

**DEVELOPMENT OF A COMBINED DILATOMETER AND MASS
SPECTROMETER SYSTEM FOR STUDYING GAS PHASE
CHEMISTRY AND KINETICS DURING SINTERING**

A Thesis

Presented to

The Faculty of the Graduate School

at the University of Missouri

In Partial Fulfillment

of the Requirements for the Degree

Master of Science

by

Matthew Schurwanz

Dr. Stephen J. Lombardo, Thesis Supervisor

December 2010

The undersigned, Appointed by the Dean of the Graduate School, have examined the thesis entitled

**KINETIC AND GAS PHASE ANALYSIS OF THE SINTERING OF
STRONTIUM TITANATE USING A COMBINED DILATOMETERY
MASS SPECTROMETERY SYSTEM**

Presented by

Matthew Schurwanz

A candidate for the degree of

Master of Science

And hereby certify that in their opinion it is worthy of acceptance.

Dr. Stephen J. Lombardo _____

Dr. Qingsong Yu _____

Dr. David Retzloff _____

Acknowledgements

First and foremost I would like to thank Dr. Stephen J. Lombardo for the limitless patience he has shown me, for accepting me as his student even though I didn't have the most impressive grades and for giving me the opportunity to finish my degree despite the long and arduous path getting to this point. I really learned a lot from you and I sincerely appreciate the ways you have "held our feet to the fire" and the general high level quality that you hold us to.

I would also like to show my appreciation to the GAANN (Graduate Assistantship in Areas of National Need) Fellowship for providing the funding for my graduate career, allowing me to expand my horizons by attending conferences and providing resources for my research that would otherwise not have been available.

I also want to thank the faculty and staff of the Chemical Engineering department. I have learned much during my years at the University of Missouri, not only about mass transfer and kinetics, but also about taking a scientific approach to the world and what it means to be an Engineer.

Finally I wish to express my appreciation to my fellow graduate students: Kai Feng and Jeong Woo Yun for developing and training me to use the combined dilatometry and mass spectrometry; Murray Moss for helping me with experiments while I was working on my thesis; Brandon Abeln and Andrew Ritts for their advice and assistance as well as Kumar Krishnamurthy, Rajiv Sachanandani, Ki Yong Lee and Jun Oh for their help and support over the years.

**DEVELOPMENT OF A COMBINED DILATOMETER AND MASS
SPECTROMETER SYSTEM FOR STUDYING GAS PHASE
CHEMISTRY AND KINETICS DURING SINTERING**

Matthew Schurwanz

Dr. Stephen J. Lombardo

Thesis Supervisor

ABSTRACT

An in-depth analysis of the components and materials comprising the combined dilatometry mass spectrometry (CDMS) apparatus is provided. This includes recent modifications, operating procedures and information on how and why major system failures have occurred. The CDMS system is then used to study the gas phase reactions that occur during the sintering of strontium titanate. Two families of peaks, mass to charge (m/z) ratios 44 and 64 being the primary peaks, are consistently observed prior to the onset of sintering. Based on isotope ratios, cracking patterns, and comparisons to the decomposition of model compounds, these gases have been identified as carbon dioxide and sulfur dioxide respectively. Quantitative analysis was performed by comparing the primary peak size from the strontium titanate sample to the decomposition of the model compounds, showing that these two gases can account for between 60 to 200% of the observed weight loss. This range is because it is unclear whether the carbon and sulfur reacted with oxygen occurring in the crystal matrix, or with trace oxygen in the atmosphere.

Su and Johnson [1] have previously proposed a method to determine the apparent activation energy of sintering, which requires no simplified models and only simple experiments. However, the equation used for this method contains an integral that can not be evaluated analytically. Here, an approximation developed by Lee and Beck [2] is modified to generate three analytic approximations for the integral. These are then compared to numeric integration to find the activation energy of sintering for simulated data. All three equations are proven to be highly accurate, two of them even more so than numeric integration when noise is present in the data. Additionally, if an equation for the mechanism is known, the equation can be substituted for the integral so that the mechanism equation can be mathematically manipulated to facilitate analysis of the assumed mechanism.

References

1. H. Su, and D. L. Johnson, Master Sintering Curve: A Practical Approach to Sintering, *J. Am. Ceram. Soc.*, **79** [12] 3211-17 (4.1996).
2. T. V. Lee, and S. R. Beck, A New Integral Approximation Formula for Kinetic Analysis of Nonisothermal TGA Data, *AIChE J.*, **30** [3] 517-519 (4.1984).

TABLE OF CONTENTS

ACKNOWLEDGEMENTS	ii
ABSTRACT	iii
LIST OF FIGURES	viii
LIST OF TABLES	xii
CHAPTERS	
1. INTRODUCTION	1
1.1 Sintering Background	2
1.2 Analysis Techniques	6
1.3 Chapter Summaries	9
1.4 References	11
2. EXPERIMENTAL AND SYSTEM DETAILS	16
2.1 Introduction	17
2.1.1 System Overview	17
2.2 System Details	18
2.2.1 Coolant Flow System	18
2.2.2 Gas Flow System	19
2.2.3 Furnace	24
2.2.4 Dilatometer	29
2.2.5 Mass Spectrometer	30
2.3 Equipment Failures	37
2.4 Procedure	38

3.	HIGH TEMPERATURE CHEMISTRY DURING THE SINTERING OF STRONTIUM TITANATE.....	41
3.1	Introduction.....	42
3.2	Experimental.....	43
3.3	Results.....	46
3.4	Discussion.....	59
3.5	Conclusion.....	61
3.6	References.....	62
4.	ANALYTIC METHODS FOR DETERMINATION OF ACTIVATION ENERGY USING THE MASTER SINTERING CURVE APPROACH.....	63
4.1	Introduction.....	64
4.2	Theory.....	65
4.2.1	Master Sintering Curve.....	65
4.2.2	Method of Lee and Beck.....	68
4.2.3	Application of the Lee and Beck Approximation to the MSC Method.....	70
4.3	Results and Discussion.....	72
4.4	Conclusions.....	86
4.5	References.....	87
5.	CONCLUSIONS & FUTURE WORK.....	88
5.1	Conclusions.....	89
5.2	Future Work.....	91

APPENDIX A: DILATOMETER SIGNAL CORRECTION ANALYSIS.....	94
A..1 Introduction.....	95
A..2 Background.....	96
A..3 Computer Analysis.....	102
A..4 Conclusion.....	107

LIST OF FIGURES

1.1	Material transport mechanisms contributing to the sintering of a consolidated mass of polycrystalline particles: (1) Surface diffusion, (2) vapor transport, (3) volume diffusion, and (4) grain boundary diffusion [1].	3
1.2	Physical states during the initial stages of sintering. (a) Starting particles, (b) rearrangement, and (c) neck formation [1].	4
1.3	Physical states during the intermediate stage of sintering: (a) Neck growth and volume shrinkage, (b) lengthening of grain boundaries, and (c) continued neck growth and grain boundary lengthening, volume shrinkage and grain growth [1].	5
1.4	Physical states during the final stage of sintering: (a) Grain growth with discontinuous pore phase, (b) grain growth with porosity reduction, and (c) grain growth with porosity elimination [1].	6
2.1	Diagram of the coolant flow system for the CDMS.	18
2.2	Diagram of the gas flow system for the CDMS.	19
2.3	Linearized diagram of path for the silica capillary.	21
2.4	Detailed image of the MS interface in the flow system including the silica capillary. Images of interior components are overlaid on top of exterior components.	21
2.5	Modifications made to the standard MCR-0057 mullite combustion tube carried by McDanel Advanced Ceramic Technologies.	23
2.6	Cross section diagram overview of furnace and components.	25
2.7	Image taken of a pressed sample loaded into the sample holder.	27

2.8	Schematic for 7.5 kVA thyristor power supply.....	29
2.9	Diagram of the primary components and layout for the mass spectrometer.....	32
2.10	Diagram of the interior workings of an oil diffusion pump.....	33
2.11	Hardware layout on the top board of the mass spectrometer.....	34
3.1	Schematic of the combined dilatometer/mass spectrometer apparatus showing the gas handling system, the furnace/dilatometer assembly, mass spectrometer, and data acquisition computers.....	44
3.2	Temperature (T), scaled shrinkage (ΔL ; total shrinkage is 17.3%), and species intensity (I) versus time for 1 g of SrTiO ₃ heated at 14°C/min in flowing helium.....	46
3.3	Temperature (T) and species intensity (I) versus time for SrTiO ₃ heated at 14°C/min in flowing helium. a) Species with m/z ratios of 12, 16, 28, 44, and 45. b) Species with m/z ratios of 16, 32, 48, and 64. c) Species with m/z ratios of possible isotopes related to the species of m/z ratios of 16, 32, 48, and 64 in panel b).....	48
3.4	Temperature (T) and species intensity (I) versus time for 0.25 g of SrSO ₄ heated at 14°C/min in flowing helium.....	54
3.5	Temperature (T) and species intensity (I) for m/z=44 versus time for samples of SrTiO ₃ , SrCO ₃ , and SrSO ₄ heated at 14°C/min in flowing helium.....	55
3.6	Temperature (T) and species intensity (I) for SrTiO ₃ in loose powder form heated at 14°C/min in flowing helium.....	57
4.1	Data simulated using second order kinetics from Equation (4.20) at three different linear heating rates with an activation energy of 450 kJ/mol.....	72

4.2	MSCs for simulations created with Equation (4.20) at A) $Q=250$ kJ/mol, B) $Q=450$ kJ/mol, and C) $Q=650$ kJ/mol. In each figure, nine curves are shown representing the three heating rates which were each analyzed with Equations (4.21), (4.22) and (4.23). The results from numeric integration and the Lee and Beck approach, Equations (4.21) and (4.23), are virtually indistinguishable from each other.	75-76
4.3	Comparison graph of temperature and density data generated for simulations ran with an activation energy of 450 kJ/mol at a linear heating rate of 14 °C/minute using Equations (4.20) and (4.24).	78
4.4	MSCs for a simulation generated using Equation (4.24), a simplified form of the Analytic Expression. For clarity, only a single MSC for each equation has been shown. Activation energies evaluated with lower limits of integration close to room temperature. A line has been added to demark a relative density of 0.6 for comparison with earlier figures.	80
4.5	Temperature/Density data for the $Q = 450$ kJ/mol simulation with +/- 2% noise added.	81
4.6	Comparison of Equation (4.23) to first and second order kinetics from Table 4.1	83
4.7	Equation (4.26), graphed with (a) 2 nd Order, and (b) 1 st Order, kinetic approximations so that the activation energy can be determined from the slope.	85
A.1	Alumina Piston Correction File, provided by Linseis software, with best-fit line and equation.	96
A.2	Two zero files at different heating rates, one using zirconia spacers and one without. Vertical lines have been added to denote the soak period for each run.	97

A.3	Three zero files run in rapid succession, each having a low temperature soak at 200 °C and a high temperature soak at 1500 °C, in helium atmosphere on November 20 th 2007 with calcia stabilized zirconia spacers.....	99
A.4	Shrinkage experienced by zero file ZrO(Ar2), which had a heating rate of 15 °C per minute, along with a 6 th order polynomial fit for each lettered section.....	100
A.5	Temperature profile, raw data and manual data correction with Equation (A.1) for strontium titanate run SrTiO12a.....	101
A.6	(a) Experimental temperature profile, Zero file, Piston Correction and the difference between temperature based analysis and manual analysis with Equation (A.1). (b) Raw Data, Manual Analysis and temperature based analysis over the time interval when disagreements arise.....	103
A.7	(a) Temperature profile, Polynomial fit of zero file and the difference between Time Based Zero File Analysis and Equation (A.1). (b) Temperature profile, Equation (A.1), Time and Temperature based analysis as well as calculations performed with the dilatometer software not using a zero file, over the soak and cooling.....	106

LIST OF TABLES

1.1	Sintering mechanisms and driving forces [Adapted from Ref. 1].	3
1.2	Three stages of sintering [1].	4
2.1	PID settings recommended by Linseis for a single thermocouple system.	27
2.2	Dilatometer settings for data acquisition.	40
2.3	Mass spectrometer settings that make up a Method.	40
2.4	Steps for dilatometer data analysis.	40
3.1	Comparison of the integrated and normalized m/z ratios evolved from strontium titanate and potassium bicarbonate, and measured, tabulated [1-2], or calculated m/z ratios corresponding to cracking patterns (CP) for carbon dioxide and its isotopes.	49
3.2	Species and natural isotopic abundances for S, Ti, O, and C [2].	51
3.3	Comparison of the integrated and normalized m/z ratios evolved from strontium titanate and calculated m/z ratios corresponding to cracking patterns (CP) for titanium monoxide and its isotopes.	52
3.4	Comparison of the integrated and normalized m/z ratios evolved from strontium titanate, strontium sulfate, and tabulated [1-2] or calculated m/z ratios corresponding to cracking patterns (CP) for sulfur dioxide and its isotopes.	53
3.5	Weight losses during heating for potassium bicarbonate, strontium carbonate, and strontium sulfate used to calibrate the MS for the strontium titanate sample. All weights normalized to 1 g of sample.	58
4.1	Kinetic mechanisms with their integrated forms.	69

4.2	Activation energies determined by the three methods for different input Q values...	76
4.3	Activation energies determined for density data simulated with $Q=450$ kJ/mol with and without 2% noise.....	81
4.4	Calculated activation energies and pre-exponential values from linear analysis of simulated data using 1 st Order and 2 nd Order kinetic approximations.....	84

CHAPTER 1

INTRODUCTION

1.1 Sintering Background

Ceramics can be broadly broken into two categories: traditional ceramics and advanced ceramics. Components from traditional ceramics are often large and include concrete, porcelain and refinery materials. Materials in this category are chosen for physical properties such as strength, hardness and high temperature stability. Advanced ceramics are often used in smaller components such as capacitors, circuit boards and other semi-conductors. Materials in this category are chosen for their electrical or optic properties, which can be fine tuned by adding small amounts of other materials, which is called doping. Due to the hardness and brittleness of most ceramics, machining can be time consuming and expensive, so a common forming method for both types is powder processing. This involves forming solid ceramic particles into the desired shape and the resulting “green body” is then heated to high temperature to create a finished body with the desired properties. This process of heating without melting to change the physical and electrical properties of a substrate is called sintering, and generally includes a significant increase in density and numerous changes in microstructure.

The four primary mechanisms for sintering are summarized in Table 1.1. Depending on the driving forces present and the material undergoing sintering, multiple mechanisms can take place. For example, the sintering of strontium titanate (SrTiO_3) occurs primarily by solid state sintering but four types of diffusive transport take place, as shown in Figure 1.1: vapor transport, surface diffusion, volume diffusion and grain boundary diffusion. Even though all four types of transport take place, only the last two cause densification by bringing particle centers closer together.

Table 1.1: Sintering mechanisms and driving forces [Adapted from Ref. 1]

Type of Sintering	Transport Mechanism	Driving Force
Vapor-phase	Evaporation/condensation	Difference in vapor pressure
Solid-state	Diffusion	Free energy or chemical potential
Liquid-state	Viscous flow, diffusion	Capillary pressure, surface tension
Reactive liquid	Viscous flow, solution precipitation	Capillary pressure, surface tension

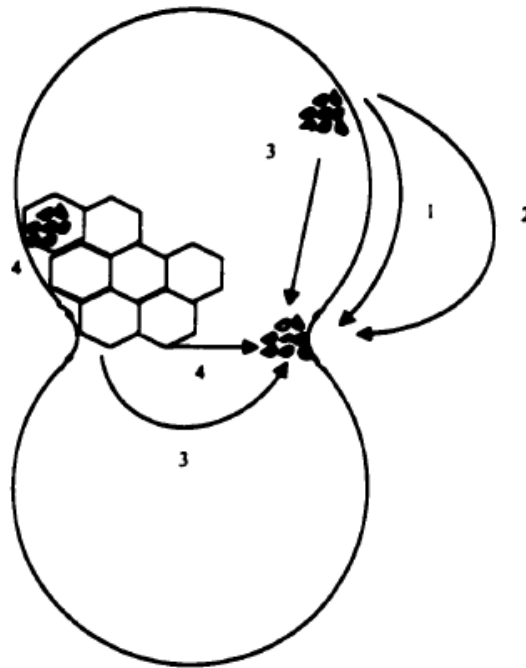


Figure 1.1: Material transport mechanisms contributing to the sintering of a consolidated mass of polycrystalline particles: (1) surface diffusion, (2) vapor transport, (3) volume diffusion, and (4) grain boundary diffusion. [1]

The three primary stages of sintering, differentiated by the primary modes of material transport and the physical changes that occur, are outlined in Table 1.2. The first stage, pictured in Figure 1.2, involves the rearrangement of particles and initial neck

growth via surface diffusion. Though surface diffusion does not cause densification, it has a relatively low activation energy, leads to the smoothing of surface roughness, and if two particles are close enough, the growth of a neck at the interface.

Table 1.2: Three stages of sintering [1].

First stage (initial)
Rearrangement
Neck formation
Second stage (intermediate)
Neck growth
Grain growth
High shrinkage
Pore phase continuous
Third stage (final)
Much grain growth
Discontinuous pore phase
Grain boundary pores eliminated

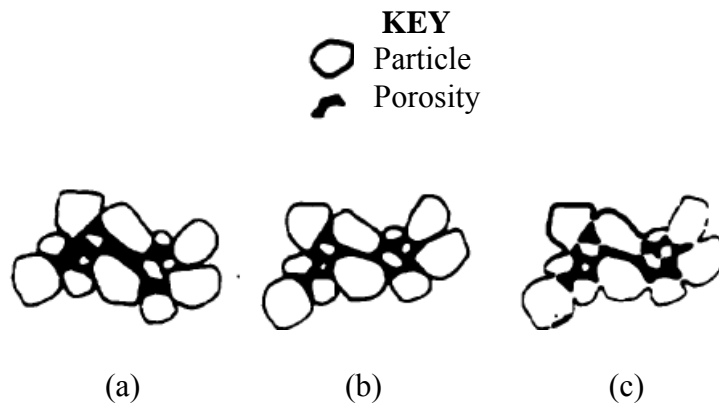


Figure 1.2: Physical states during the initial stages of sintering. (a) Starting particles, (b) rearrangement, and (c) neck formation [1].

The intermediate stage of sintering, illustrated in Figure 1.3, is the stage when the majority of shrinkage occurs and is generally dominated by grain boundary diffusion. Grain boundary diffusion is often looked at as the movement of pores from between particles to the exterior of the interface, resulting in large amounts of neck growth. This process continues until the pores become isolated.

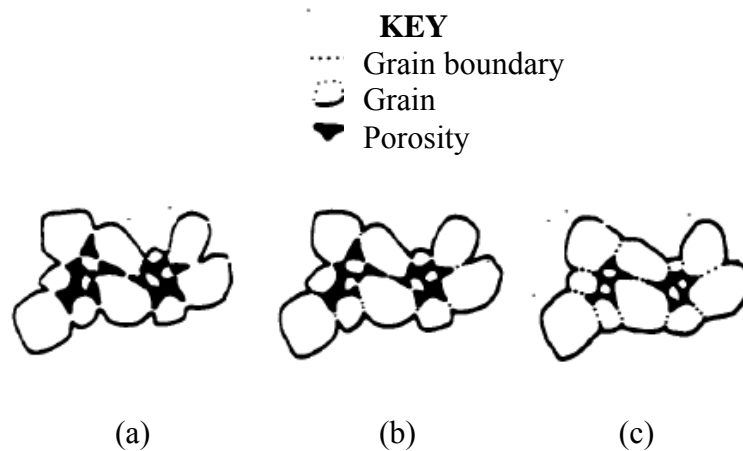


Figure 1.3: Physical states during the intermediate stage of sintering: (a) Neck growth and volume shrinkage, (b) lengthening of grain boundaries, and (c) continued neck growth and grain boundary lengthening, volume shrinkage and grain growth [1].

The final stage of sintering, illustrated in Figure 1.4, refers to any densification that occurs after the pores have become isolated, and is dominated by lattice, also called volume, diffusion. Because the pores are isolated, diffusion needs to progress by means of vacancies in the crystal lattice rather than more direct routes. At this stage, densification can be limited by the grain growth, and if sintering occurs too rapidly, pores can be completely cut off with no way of being removed.

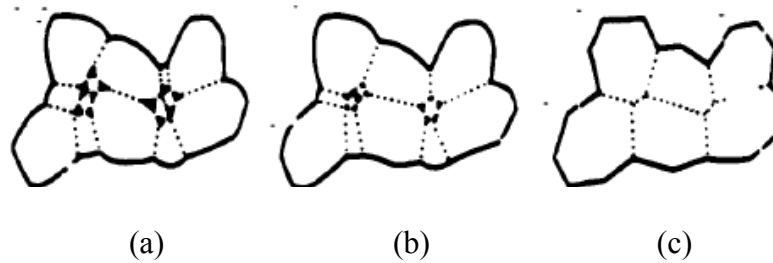


Figure 1.4: Physical states during the final stage of sintering: (a) Grain growth with discontinuous pore phase, (b) grain growth with porosity reduction, and (c) grain growth with porosity elimination [1].

1.2 Analysis Techniques

The primary method for measuring the progress of sintering is by using dilatometry to monitor the length change of the sample, which can be correlated to density changes. Because sintering is a thermally activated process, the length change, as a function of time or temperature, can be used to determine activation energy of sintering. The activation energy is the energy barrier that prevents the particles from transitioning to the lower energy sintered state, and can subsequently be used to estimate the rate of sintering for new heating cycles. However, dilatometry can not provide any information on other physical or chemical changes in the sample. Analysis of the microstructure, for example, can not be performed in situ and generally involves quenching the sample at the desired point in the sintering process, cutting, polishing and then taking pictures with a scanning electron microscope (SEM). And there is yet to be a standard method for measuring chemical processes occurring during sintering.

Over the last 40 years, a number of techniques have emerged to identify the gas-phase species that are evolved when inorganic materials are heated to high temperature;

reviews and summaries for these techniques can be found elsewhere [2-6]. In one approach, a Knudsen diffusion cell containing an inorganic material is heated, and the reaction products evolved into the gas phase are either trapped for subsequent analysis or monitored directly by a mass spectrometer. A second technique has used the flow of a carrier gas across a sample to transport the evolved species for analysis. The former type of measurement is made under conditions corresponding to chemical equilibrium, whereas the latter type may not correspond to chemical equilibrium but instead may represent non-equilibrium environments, such as may be found during sintering.

Although both of these techniques have supplied a wealth of information about reactions occurring at high temperature, less information has appeared in the literature as to possible direct relationships between reactions that occur at high temperature and the rate of sintering of ceramic green bodies. A broad question of interest is to what extent, at what concentrations, and at what temperature do evolved species inhibit or enhance sintering kinetics, influence material composition, including defect chemistry, and ultimately influence the development of microstructure. The types of reactions [5-39] which may occur at elevated temperature include the decomposition or dissociation of the inorganic material, the volatilization of sintering aids or other additives, and the removal or modification of native surface layers which may be different from the bulk. In addition to the reactions that arise from the sample itself, the furnace environment may participate in or catalyze reactions [40]; the gas phase is thus changed which may influence sintering kinetics, sample composition, and microstructural development.

Although high temperature dilatometers [27-36] and mass spectrometers [14, 16-18, 34, 35] have been used separately, these techniques have not been routinely combined to simultaneously monitor the gas phase during sintering. To highlight the potential utility of such measurements, Ness and Rafaniello [26] have examined the origin of density gradients in β -silicon carbide bodies during sintering by monitoring the evolution of CO with a gas chromatograph (GC). With this approach, they were able to correlate CO evolution with low sintered density. In another study, Carroll et al. [38] monitored CO evolution during the sintering of nanophase SiC/Si₃N₄ to show how the density of the material could be optimized. Both studies highlight the utility of using information about the gas phase to rationalize sintering behavior and ultimately microstructural development.

1.3 Chapter Summaries

This work focuses on what can be done with a combined dilatometer mass spectrometer (CDMS) system. Chapter 2 goes over the CDMS in detail, including part numbers and software settings. The layouts for the gas flow and coolant flow systems are outlined as well as recent changes to the system. Due to equipment failures, a secondary thermocouple has been installed, and the interface between the dilatometer and the mass spectrometer has been redesigned for a quicker, smoother flow path.

In chapter 3, the CDMS unit is used to examine the high temperature chemistry that occurs during the sintering of strontium titanate. In the temperature range from 450-1000°C, carbon dioxide and fragments related to its cracking are observed; these species are assigned to the decomposition of organic species and trace strontium carbonate. In the temperature range of 900-1470°C, species are identified that can be assigned to the evolution of SO₂. These species were identified by using tabulated cracking patterns and natural isotopic abundances, by obtaining cracking patterns from known gases (CO₂), and by using model compounds (KHCO₃, SrCO₃, SrSO₄) which evolve the suspected species at elevated temperature.

In chapter 4, the master sintering curve (MSC) approach by Su and Johnson [41] is approximated to yield three different analytical equations by using the method of Lee and Beck [42]. Numeric integration is used along with these equations to calculate the activation energies of data simulated at three heating rates with three different activation energies. Across all simulations studied, including those with added noise, all of the

equations prove to be very accurate in calculating input activation energies. Furthermore, one of the simplified equations matches the behavior of numeric integration very closely and could be useful for testing theoretical mechanism equations because it can be mathematically manipulated in ways that the integral can not.

Appendix A details the signal correction process performed by the dilatometer software. This process is designed to account for readings that will be picked up by the dilatometer regardless of a sample being present, such as the thermal expansion of the measuring piston. An equation that can be used to manually reproduce these corrections is tested against different modes of software analysis to determine what conditions and files are required to accurately evaluate the data.

1.4 References

1. D. W. Richerson, *Modern Ceramic Engineering*. Marcel Dekker, New York, 1992.
2. J.L. Margrave, *The Characterization of High-Temperature Vapors*. John Wiley & Sons, New York, 1967.
3. J.H. Hastie, *High Temperature Vapors: Science and Technology*. Academic Press, New York, 1975.
4. *Characterization of High Temperature Vapors and Gases, Vol. 1*, Edited by J.H. Hastie. NBS Special Publication 561, U.S. Department of Commerce, 1979.
5. G. A. Somorjai, "Studies of the Sublimation Mechanism of Solids"; in *Advances in High Temperature Chemistry, Vol. 2*, Edited by L. Eyring. Academic Press, New York, 1969.
6. W. L. Worrel, "Dissociation of Gaseous Molecules on Solids at High Temperature"; in: *Advances in High Temperature Chemistry, Vol. 4*, Edited by L. Eyring. Academic Press, New York, 1971.
7. D. A. Northrop, "Vaporization of Lead Zirconate-Lead Titanate Materials"; *J. Am. Ceram. Soc.*, **50** [9] 441-45 (1967).
8. D.A. Northrop, "Vaporization of Lead Zirconate-Lead Titanate Materials: II, Hot-Pressed Compositions at Near Theoretical Density"; *J. Am. Ceram. Soc.*, **51** [7] 357-61 (1968).
9. R.B. Atkin and R.M. Fulrath, "Point Defects and Sintering of Lead Zirconate-Titanate"; *J. Am. Ceram. Soc.*, **54** [5] 265-70 (1971).

10. R.L. Holman and R.M. Fulrath, "Intrinsic Nonstoichiometry in Single Phase $\text{Pb}(\text{Zr}_{.5}\text{Ti}_{.5})\text{O}_3$ "; *J. Am. Ceram. Soc.*, **55** [4] 192-97 (1972).
11. A.I. Kingon and J.B. Clark, "Sintering of PZT Ceramics: I, Atmosphere Control"; *J. Am. Ceram. Soc.*, **66** [4] 253-56 (1983).
12. A.I. Kingon and J.B. Clark, "Sintering of PZT Ceramics: II, Effect of PbO Content on Densification Kinetics"; *J. Am. Ceram. Soc.*, **66** [4] 256-60 (1983).
13. B.V. Hiremath, A.I. Kingon, and J.V. Biggers, "Reaction Sequence in the Formation of Lead Zirconate-Titanate Solid Solution: Role of Raw Materials"; *J. Am. Ceram. Soc.*, **66** [11] 790-93 (1983).
14. K.H. Hardtl and H. Rau, "PbO Vapor Pressure in the $\text{Pb}(\text{Ti}_{1-x}\text{Zr}_x)\text{O}_3$ System"; *Solid State Commun.*, **7** [1] 41-45 (1969).
15. N.G. Schmahl, G.K. Schwitzgebel, H. Kling and E. H. Speck, "Thermodynamic Investigations of the Solid Solution of Lead Zirconate-Titanate"; *Mater. Res. Bull.*, **14** [9] 1213-1218 (1979).
16. A. Popovic, B. Malic, and L. Bencze, "Knudsen Cell Mass Spectrometric Investigation of the $\text{PbO-ZrO}_2\text{-TiO}_2$ System"; *Rapid Commun. Mass Spectrom.*, **13** [12] 1129-37 (1999).
17. P. Rocabois, C. Chatillon, and C. Bernard, "Thermodynamics of the Si-O-N System: I, High-Temperature Study of the Vaporization Behavior of Silicon Nitride by Mass Spectrometry"; *J. Am. Ceram. Soc.*, **79** [5] 1351-60 (1996).
18. Sin-Shong Lin, "Mass Spectrometric Analysis of Vapors in Oxidation of Si_3N_4 Compacts"; *J. Am. Ceram. Soc.*, **58** [3-4] 160 (1975).

19. M. A. Mulla, V. D. Krstic, "Pressureless Sintering of β -SiC with Al_2O_3 Additions"; *J. Mater. Sci.*, **29** 934-38 (1994).
20. T. Grande, H. Sommerset E. Hagen, K. Wiik, and M. Einarsrud, "Effect of Weight Loss on Liquid-Phase-Sintered Silicon Carbide"; *J. Am. Ceram. Soc.*, **80** [4] 1047-52 (1997).
21. W. van Rijswijk, "Effect of Carbon as a Sintering Aid in Silicon Carbide"; *J. Am. Ceram. Soc.*, **73** [1] 148-49 (1990).
22. W. J. Clegg, "Role of Carbon in the Sintering of Boron-Doped Silicon Carbide"; *J. Am. Ceram. Soc.*, **83** [5] 1039-43 (2000).
23. T. Quadir and D. W. Readey, "Microstructure Development of Zinc Oxide in Hydrogen"; *J. Am. Ceram. Soc.*, **72** [2] 297-302 (1989).
24. H. Wada, Ming-Jong Wang, and Tseng-Ying Tien, "Stability of Phases in the Si-C-N-O System"; *J. Am. Ceram. Soc.*, **71** 837-40 (1998).
25. U. Neidhardt, H. Schubert, E. Bischoff, and G. Petzow, "Gas Pressure Sintering of Si_3N_4 in $\text{N}_2/\text{CO}/\text{CO}_2$ Atmosphere"; *Key Engineer. Mater.*, **89-91** 187-92 (1994).
26. E. A. Ness, and W. Rafaniello, "Origin of Density Gradients in Sintered β -Silicon Carbide Parts"; *J. Am. Ceram. Soc.*, **77** [11] 2879-84 (1994).
27. H. Lee and R.F. Speyer, "Pressureless Sintering of Boron Carbide"; *J. Amer. Ceram. Soc.*, **86** [9] 1468-73 (2003).
28. C. Boberski, H. Bestgen, and R. Hamminger, "Microstructural Development during Liquid-Phase Sintering of Si_3N_4 Ceramics"; *J. Eur. Ceram. Soc.*, **9** 95-99 (1992).

29. J. Jung, "Body-Controlled Sintering and Differential Thermal Analysis up to 2400°C"; *Keramische Zeit.*, **42** [11] 830-32 (1990).
30. O. Abe and S. Kanzaki, "High-Temperature Dilatometer for Non-Oxide Ceramics"; *J. Ceram. Soc. Japan*, **97** 187-91 (1989).
31. M. L. Mecartney, "Influence of Dissolved Si₃N₄ on the Properties of Al₂O₃-MgO-SiO₂ Glass"; *J. Mat. Sci. Lett.*, **6** [3] 370-72 (1987).
32. H-J. Kleebe, W. Braue, and W. Luxem, "Densification Studies of SRBSN with Unstabilized Zirconia by Means of Dilatometry and Electron Microscopy"; *J. Mat. Sci.*, **29** [5] 1265-75 (1994).
33. S. Siegel, M. Hermann, and G. Putzky, "Effect of Process Atmosphere on Dilatometer Controlled Sintering"; *Key Engineer. Mater.*, **89-91** 237 (1994).
34. L. Chen, W. Lengauer, P. Ettmayer, K. Dreyer, H.W. Daub, and D. Kassel, "Fundamentals of Liquid Phase Sintering for Modern Cermets and Functionally Graded Cemented Carbonitrides (FGCC)"; *Inter. J. of Refractory & Hard Metals*, **18** 307 (2000).
35. L. Chen, W. Lengauer, and K. Dreyer, "Advances in Modern Nitrogen-Containing Hardmetals and Cermets"; *Inter. J. of Refractory & Hard Metals*, **18** 153-61 (2000).
36. E.A. Oliber, E.R. Benavidez, G. Requena, J.E. Fiscina, and C.J.R. Gonzalez Oliver, "High Temperature Reactions, Densification and the Peritectic Decomposition of YBa_{2-x}Sr_xCu₃O_{7-δ} (YBSCO) Superconducting Ceramics"; *Physica C*, **384** [11] 247-257 (2003).

37. H. Ishida, Nanri, Sh. Takechi, N. Watanabe, and K. Wakamatsu, "Oxidation Behavior of Si₃N₄ at Low Oxygen Partial Pressures"; *J. Soc. Mat. Sci. Japan*, **45** 694-99 (1996).
38. D.F. Carroll, A.W. Weimer, S.D. Dunmead, G.A. Eisman, J.H. Hwang, G.A. Cochran, D.W. Susnitzky, D.R. Beaman, and C.L. Conner, "Carbothermally Prepared Nanophase SiC/Si₃N₄ Composite Powders and Densified Parts"; *AIChE J.*, **43** [11] 2624-35 (1997).
39. K. Feng and S. J. Lombardo "Kinetic Analysis from Dilatometry and Mass Spectrometry Measurements of the Decomposition and Sintering of Calcium Carbonate"; *J. of Ceram. Proc. Res.*, **3** 101-108 (2002).
40. K. Feng and S. J. Lombardo "High-Temperature Reaction Networks in Graphite Furnaces"; *J. of Mat. Sci.*, **37** 2747-53 (2002).
41. H. Su, and D. L. Johnson, Master Sintering Curve: A Practical Approach to Sintering, *J. Am. Ceram. Soc.*, **79** [12] 3211-17 (4.1996).
42. T. V. Lee, and S. R. Beck, A New Integral Approximation Formula for Kinetic Analysis of Nonisothermal TGA Data, *AIChE J.*, **30** [3] 517-519 (4.1984).

CHAPTER 2

EXPERIMENTAL AND SYSTEM DETAILS

2.1 Introduction

This chapter details the hardware for the Combined Dilatometry/Mass Spectrometry (CDMS) system which can be used to simultaneously monitor the rate of sintering and the mass to charge (m/z) ratios of species in the gas phase. Part numbers and relevant settings for the hardware and software respectively, are included, as well as details on significant equipment failures and changes to the system.

2.1.1 System Overview

The CDMS system consists of a dilatometer (Push-Rod Dilatometer, L-75/260, Linseis, Selb, Germany) and furnace (High Temperature Tube Furnace, 1640, Thermal-Technologies, Santa Rosa, CA) coupled to a mass spectrometer (MS) (Quadrupole Mass Filter Spectrometer, 5971A, Agilent Technologies, Santa Clara, CA). The general system layout, including overviews of the coolant flow system and gas flow system are shown in Figures 2.1 and 2.2 respectively. The gas flow system is comprised of two parts: the Shell Side system maintains an inert atmosphere around the graphite elements inside the furnace and in the Tube Side system, helium carrier gas flows from a high pressure cylinder, through the dilatometer and furnace, and then enters a T-junction where a small amount of gas is diverted into the MS with the remainder vented to atmosphere. Inside the furnace, the Tube Side and the Shell Side systems are separated by a mullite tube (Combustion Tube, MCR-0057--modified, McDanel Advanced Ceramic Technologies, Beaver Falls, PA). Furthermore, this ensures that out gassing from graphite components inside the furnace does not mix with the gas flow entering the MS. Gas flow into the MS is restricted by a 45 cm length of silica tubing with an ID of 100 μm .

2.2 System Details

2.2.1 Coolant Flow System

Figure 2.1 is a diagram of the two coolant flow systems for the CDMS. A chiller (Water Recirculating Cooling System, R2200V, Dynaflux, Cartersville, GA) dissipates excess heat from the system by drawing air through a block of cooling fins while circulating 12 gallons of cooling fluid. This fluid is composed of a 2:1 ratio of distilled water to antifreeze (Defense Anti-Freeze and Pump Lubricant, DF929, Dynaflux), along with 4 fl oz of pump lubricant (Lubricist, CR92B, Dynaflux). After leaving the chiller, the coolant flows through a heat transfer coil inside a constant temperature bath, which contains an internal heater (Circulator Bath, C10/B3, Haake, Paramus, NJ). The coolant then flows through the furnace housing and returns to the chiller. The constant temperature bath is present to ensure that the measuring head for the dilatometer is maintained at 30 °C and does not experience thermal expansion. The system uses 45 degree flared fittings on the shell and electrodes, 1/8th inch NPT fittings on the front and rear flanges and contains a flow sensor so that power to the heating element will be cut if coolant flow from the chiller is interrupted.

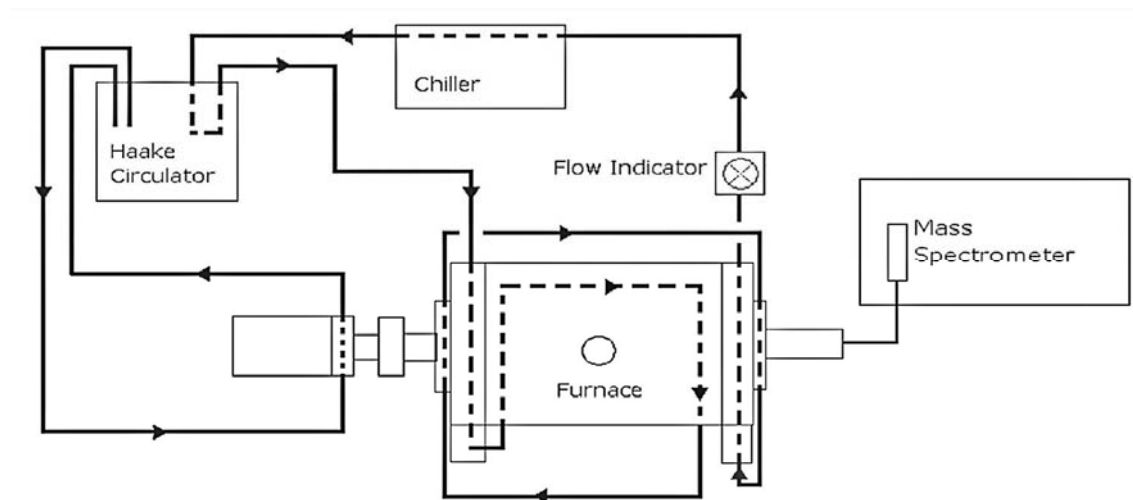


Figure 2.1: Diagram of the coolant flow system for the CDMS.

2.2.2 Gas Flow System

Figure 2.2 outlines the two independent gas flow systems in the CDMS which are separated inside the furnace by a mullite combustion tube. Both use gas stored in high pressure cylinders, have quick-fill bypasses and are connected to a vacuum pump for purging. The “shell side” system uses a continuous nitrogen purge with a flow rate between 5 and 6 liters per hour to maintain an inert atmosphere around the graphite heating element inside the furnace. The “tube side” system carries gas from the furnace, inside the mullite tube, into the MS. The tube side system has a control/mixing board which can combine gasses from up to three high pressure cylinders, though the MS is only designed for helium carrier gas. A reading of 150 on the flow meter correlates to approximately 135 mL per minute of helium.

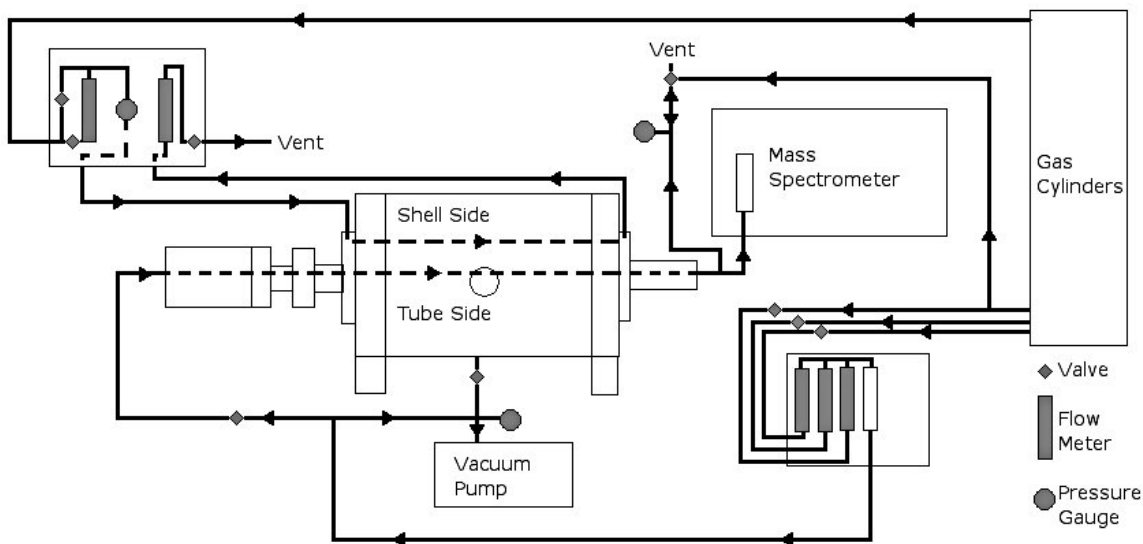


Figure 2.2: Diagram of the gas flow system for the CDMS

The tube side flow system is primarily comprised of 1/4th inch and 1/8th inch tubing connected with Swagelok (Solon, OH) fittings, while the shell side has primarily Serto (Aadorf, Switzerland) fittings. The exceptions are that on the shell side, the gas

regulator is connected to the nitrogen cylinder with a Swagelok fitting, and on the tube side, the exit from the furnace has a Serto connection. The helium gas line on the tube side also contains a desiccant tube (Drying Tube for Air and Gases, 26930, Drierite, Xenia, OH) connected in-line, near the cylinder, with barbed fittings and hose clamps.

Gas flow into the MS is restricted by a 45 cm long silica capillary with an ID of 100 μm (Fused Silica Capillary Tubing, Z-FSS-100238, Postnova Analytics, Salt Lake City, UT). Figure 2.3 shows a linearized diagram of the capillary flow path and Figure 2.4 shows a detailed image of the interface between the furnace and the MS. The capillary runs the entire length of the MS inlet heater, then through the interior of the steel tubing between the MS and the furnace and continues 11 cm into the bellows at the outlet of the furnace, including running 7 cm into the mullite tube separating the shell side from the tube side. When inserting the capillary into the mullite tube, a 5 x5 cm rolled up piece of paper can be inserted into the mullite tube and used as a funnel to ensure that the tip of the capillary does not enter the space between the mullite tube and the metal flange and become clogged. If vacuum is pulled on the shell side of the furnace while this is being done, the bellows will contract, facilitating the insertion process. The vacuum inside the MS manifold draws gas through the capillary with the remainder vented to atmosphere. The capillary is held in place by sealing the toroidal space between the silica capillary and the upstream end of a piece of 1/16th inch diameter steel tubing (HPLC Capillary Tubing, 25255, Restek Chromatography Products, Bellefonte, PA) with silicone (Ultra Blue Silicone Gasket Maker, 77B, Permatex, Hartford, CT). The silica capillary has a maximum operating temperature of 350 °C and is capable of being

inserted about 15 cm into the bellows on the furnace outlet without suffering thermal damage during a typical heating cycle.

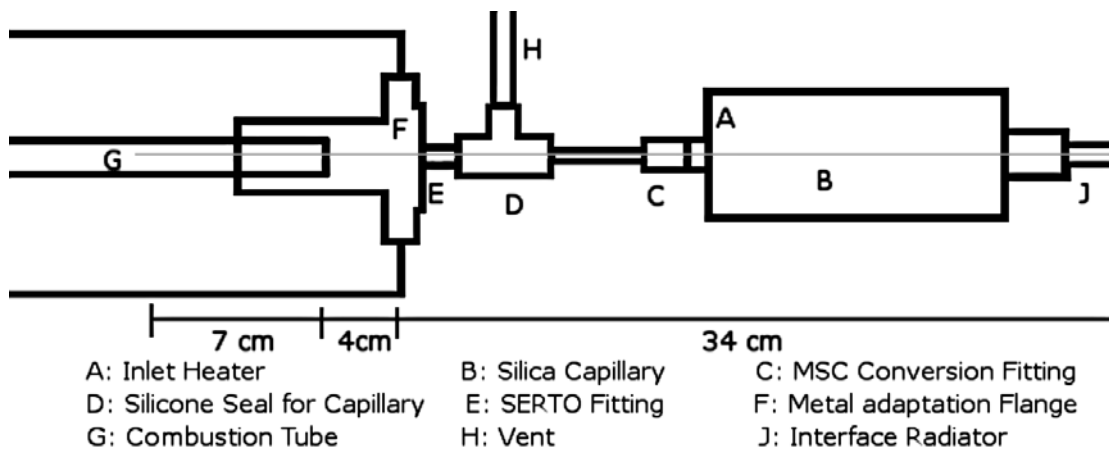


Figure 2.3: Linearized diagram of path for the silica capillary.

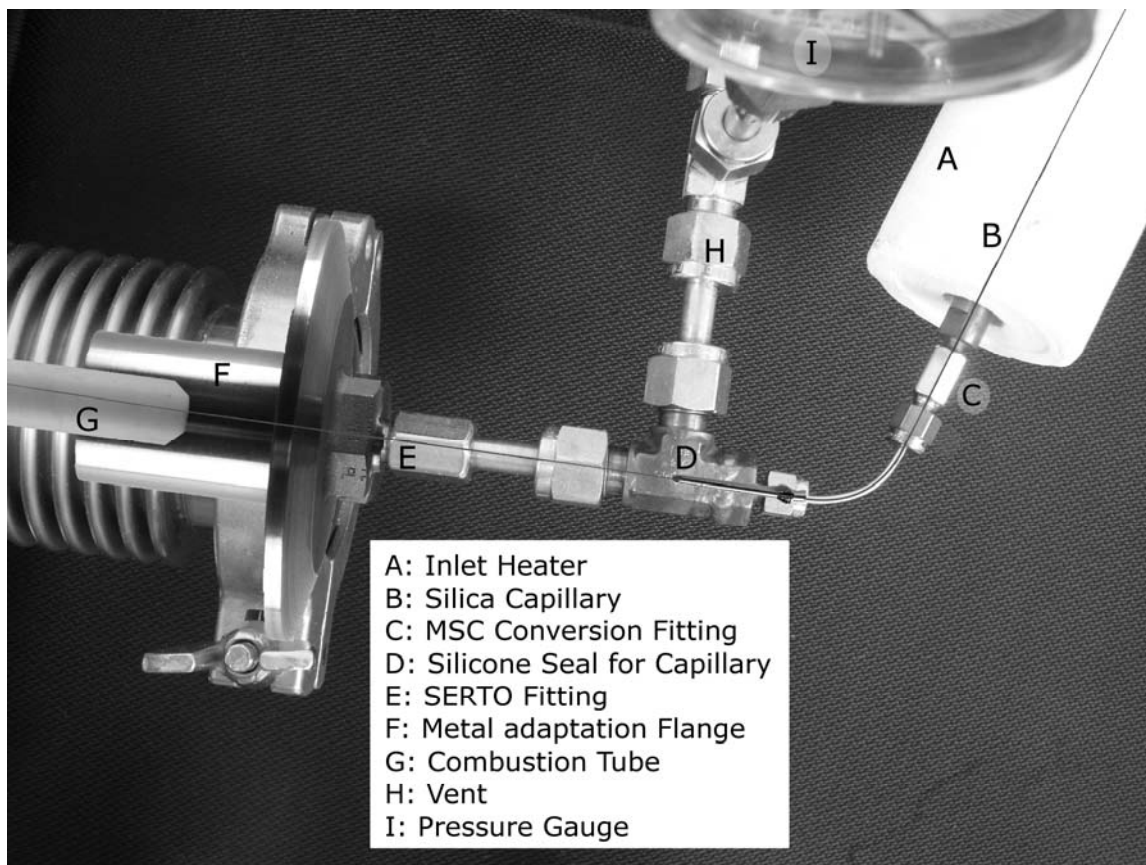


Figure 2.4: Detailed image of the MS interface in the flow system including the silica capillary. Images of interior components are overlaid on top of exterior components.

The adaptor for the inlet heater (MSD Conversion Fitting – Improved, 21314, Restek) is made of nickel-plated brass so that its teeth will mold around the inlet to help create an airtight seal. Because of this, the adaptor can be easily damaged if over-tightened and Vespel or Vespel/Graphite ferrules (Ferrules, Standard, 22210, Restek), instead of the usual stainless steel ferrules, must be used on the tubing. An aluminum sealing ring is used where the adaptor connects to the inlet heater. Both the sealing ring and ferrules are designed to be removed and replaced when the respective seals are broken.

An elevated temperature between the furnace and the MS can be maintained, by wrapping the metal tubing with heating tape (Heavy Insulated Heating Tape, STH051-020, Omega). Even though the temperature needs to be kept lower than 350 °C to avoid damaging the capillary, to prevent the heating tape from arcing to the metal surface, heavy insulated tape with a maximum operating temperature of 760 °C must be used. When this was tried, temperature was controlled with a Variac and monitored with a Type-K thermocouple inserted between the heating tape and the tubing. However, odd signals occurred in the MS data and afterwards the capillary needed to be replaced.

The mullite combustion tube is anchored to the flange at the inlet of the furnace with a silicone adhesive (Ultra Blue Silicone Gasket Maker, 77B, Permatex, Hartford, CT), which is thermally stable for intermittent exposure up to 260 °C. McDanel Ceramics modified their standard MCR-0057 for this system by reducing its length and putting a 45° bevel on the restricted end to prevent chipping during installation. The original and

modified schematics are shown in Figure 2.5. To prevent damage caused by thermal expansion, the restricted end of the combustion tube extends into a bellows at the furnace exit and is sealed with a floating o-ring.

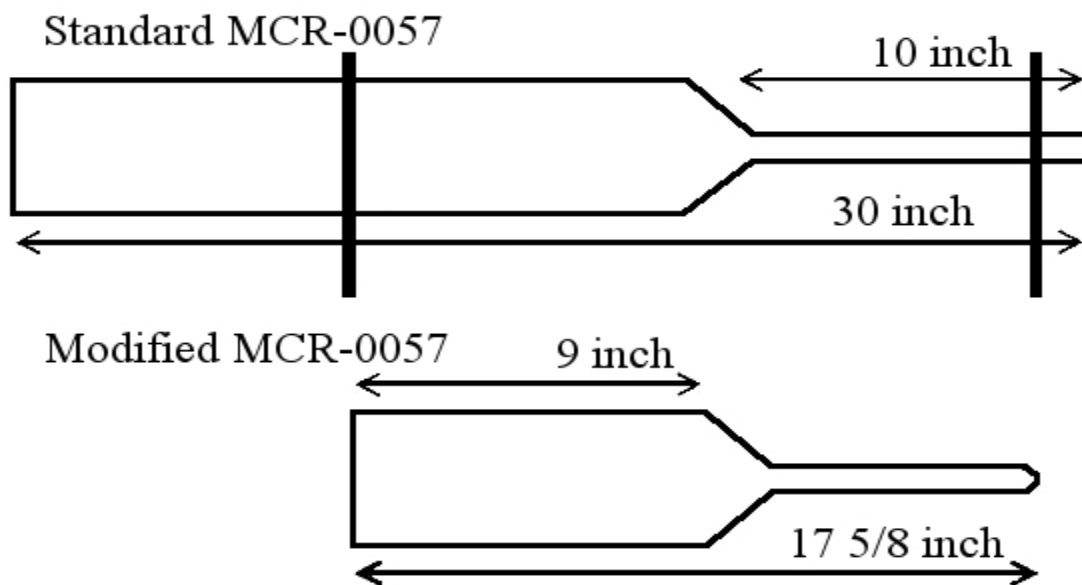
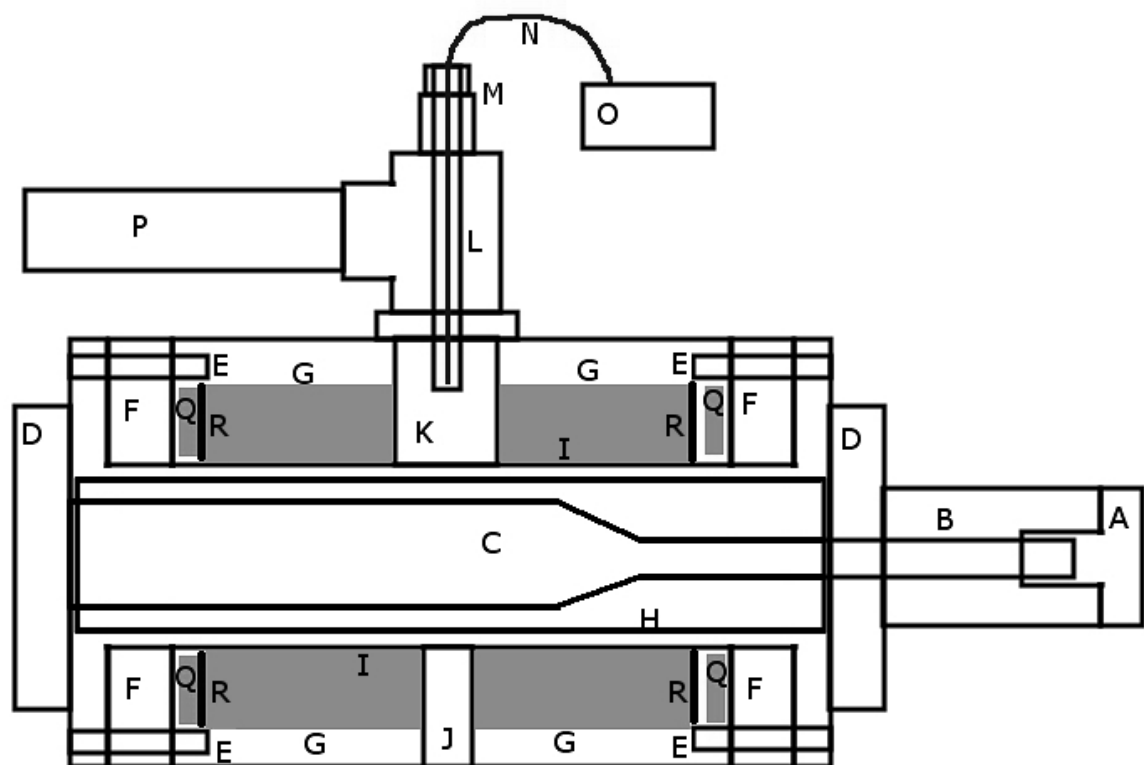


Figure 2.5: Modifications made to the standard MCR-0057 mullite combustion tube carried by McDanel Advanced Ceramic Technologies.

Originally, gas flow into the MS was controlled by a dosing valve (EV016 DOS AB, Leybold, Cologne, Germany) instead of using a silica capillary. The valve made it possible to instantly change the flow rate and to seal the MS. However, due to the weight of the dosing valve, it was clamped directly onto the MS vacuum manifold, thus leaving no space for the inlet heater to be installed. Switching to silica capillaries also made for a much smoother flow path, significantly reducing the transfer time from the furnace to the MS.

2.2.3 Furnace

Figure 2.6 is a diagram of a top-down cross section of the furnace. The sample holder for the dilatometer is inserted into the large end of the combustion tube and clamped to the flange on the entrance with a high vacuum fitting (QF, KF or NW, available at McMaster-Carr, Aurora, OH). The graphite heating element radially surrounds the combustion tube and is held in place by a copper spacer screwed into each end of the heating element. The spacers force the ends of the element outward, firmly pressing them against the electrodes. To prevent the element from rotating, a copper key is inserted into corresponding notches on the heating element and the electrodes at each end. A radial felt retainer, followed by several layers of graphite felt, surrounds the heating element. Axial felt retainers are located at each end of the graphite felt and are followed by cottony felt spacers that insulate the graphite from the electrodes. Each electrode, as well as the end caps for the shell, are held in place with 8 hex screws. Note; the end caps and electrodes are held in place by the same set of screws and are removed concurrently during disassembly.



- | | | |
|--------------------|-------------------------|------------------------|
| A: Adaptor Flange | G: Graphite Felt | M: Ultra Torr Fitting |
| B: Bellows | H: Heating Element | N: Safety Thermocouple |
| C: Combustion Tube | I: Radial Felt Retainer | O: Safety Controller |
| D: End Flanges | J: Sighting Tube | P: to Vacuum |
| E: Hex Screw Wells | K: Vacuum Port | Q: Felt Spacer |
| F: Electrodes | L: Thermocouple Tube | R: Axial Felt Retainer |

Figure 2.6: Cross section diagram overview of furnace and components.

A sighting tube runs through a hole in the graphite felt so that it is possible to monitor the temperature of the heating element during experiments with an infrared sensor. The vacuum port is located on the back of the furnace, opposite the sighting tube. A T-section has been installed at the vacuum port so that a backup type B thermocouple (17 inch bare-wire type B thermocouple, P30R-17, Omega Engineering, Stamford, CT), can be installed. The thermocouple sits in an alumina tube (Ceramic Thermocouple Protection Tube, PTR-553214-12, Omega Engineering) and is insulated with an alumina rod (Double-Bore Extruded Alumina Rods, AXD0999-13-18, McDanel

Advanced Ceramic Technologies) followed by cladding stripped from old wires. The protection tube is held in place with an ultra-torr vacuum fitting (SS-4-UT-1-4, Swagelok). Due to the low-temperature inaccuracy of type B thermocouples, the secondary thermocouple is not accurate when the furnace is below 400 °C. The relative temperature readings for the two thermocouples are also dependant on the heat transfer dynamics of the atmospheres on both the shell and tube sides. In the necessary temperature range, with nitrogen on the shell side and helium on the tube side, the readings from the secondary thermocouple can be correlated to the temperature in the main heated zone according to the following equation:

$$T_{primary}(\text{°C}) = 0.9178 * T_{backup}(\text{°C}) + 381.55(\text{°C}) \quad (2.1)$$

The secondary thermocouple is connected to a temperature/process controller (CN132, Omega Engineering) that will cut power to the heating element if it detects a temperature above 1225 °C, corresponding to 1505 °C in the heated zone. The secondary temperature sensor is important because the furnace is capable of reaching temperatures in excess of 3200 °C while the alumina sample holder has a melting point near 2700 °C and the mullite combustion tube has a maximum operating temperature of 1680 °C. One reason the cut off temperature is low is because neither thermocouple is in close proximity to the mullite tube. If accurate temperature readings of the combustion tube could be taken with an optical thermocouple, it might be possible to operate at higher temperatures. Alternately, if the mullite combustion tube was replaced with an alumina one, higher temperatures would be possible; however this would be significantly more expensive.

The temperature controller for the furnace uses another 17 inch bare-wire type B thermocouple, with similar insulation, which is located beneath the sample holder, as shown in Figure 2.7. The dilatometer software is designed to operate with dual PID control, however, this is not possible because a single thermocouple is inside the heated zone of the furnace. The signal from the primary thermocouple is split to provide both readings for the software. The manufacturer recommended PID settings for this arrangement are given in Table 2.1. Under this control scheme, the observed soak temperature is always 20-40 degrees lower than the programmed temperature at 1500 °C, though there is better agreement at lower temperatures.

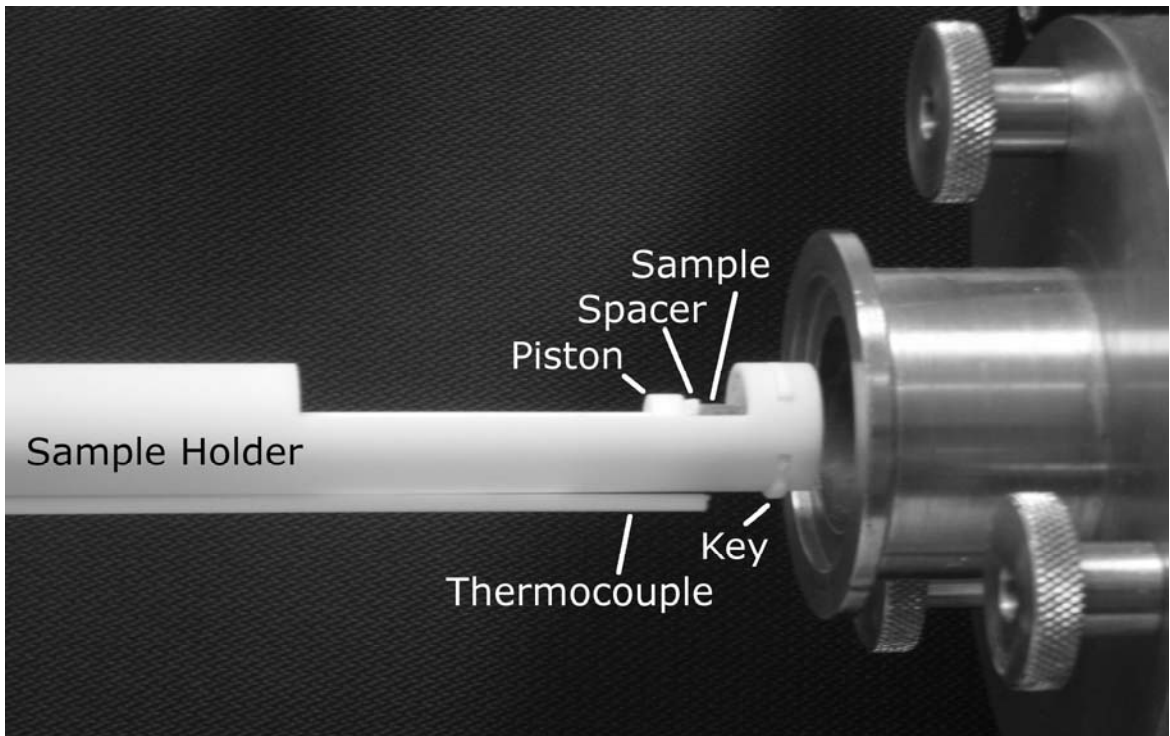


Figure 2.7: Image taken of a pressed sample loaded into the sample holder.

Table 2.1: PID settings recommended by Linseis for a single thermocouple system

		Controller 1	Controller 2
Proportional	(P)	0	200
Integral	(I)	0	1100
Derivative	(D)	0	0

Figure 2.8 shows the schematic wiring diagram for the thyristor power supply. The thyristor produces a low-voltage, high current, load across the graphite heating element and is controlled with the dilatometer software. It also supplies power to the dilatometer control board, which is used to move the piston as well as set the amount of pressure the piston applies to the sample. The thyristor has a 50 amp 125/250 volt 3-pole 3-wire plug, which provides a dual voltage so that the control board and lights can be powered on a 125 volt circuit while the heating element uses a 250 volt circuit. The aforementioned flow sensor in the coolant system, and the process controller for the secondary thermocouple, are both run in series with a normally closed relay in the thyristor so that if either sensor detects a problem, power to the heating element is cut off. A yellow LED on the front of the thyristor denotes that the relay is closed and the system is ready. The large red light on the front of the thyristor becomes lit when power is supplied to the heating element.

A low density blue build up has been found on the heating element, as well as on the outside of the mullite combustion tube, approximately 7 cm to either side of the main heated zone in the furnace. On one side, this corresponds to the reduction in diameter of the combustion tube. Although this material has not been completely identified, energy-dispersive X-ray spectroscopy (EDS) analysis showed the presence of nitrogen, potassium, sodium and carbon in addition to the silicone, aluminum and oxygen that make up mullite. Previous work showed that the graphite inside the furnace experienced off-gassing at high temperatures, and it is possible that this material comes from the heating element or graphite felt retainers.

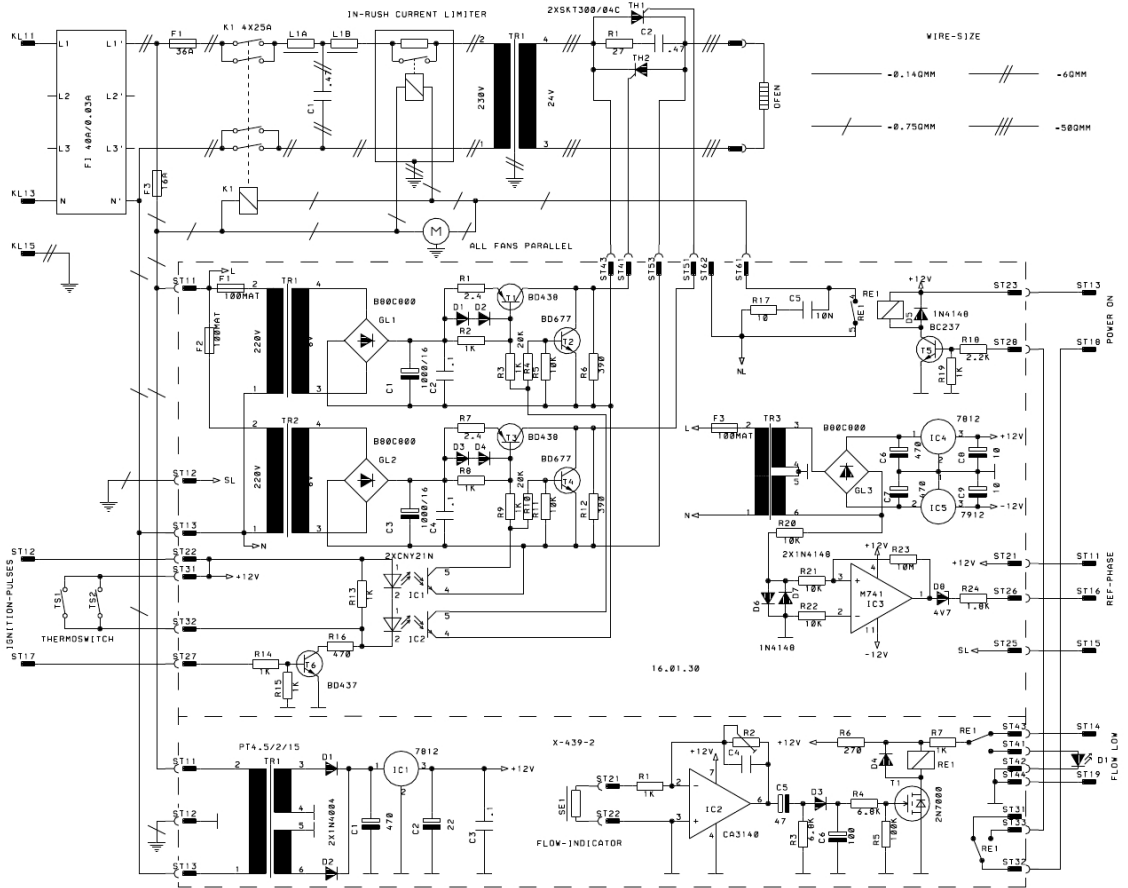


Figure 2.8: Schematic for 7.5 kVA thyristor power supply.

2.2.4 Dilatometer

The sample holder and piston for the dilatometer, shown in Figure 2.7, are composed of alumina, which during test runs in a box furnace (High Temperature Furnace, F46120CM, Barnstead Thermolyne, Dubuque, IA), reacted with strontium titanate at high temperatures. To protect the dilatometer, calcia stabilized zirconia spacers (custom made, 0.5 inch diameter, 0.03 inch thickness, Machined Ceramics Inc, Bowling Green, KY) are placed between the sample and the alumina. More common yttria stabilized zirconia spacers were also tried in the system, but at high temperatures they fused to the sample and became lightly bonded to the alumina. A layer of disposable

alumina paper (C4502, Zircar Ceramics, Florida, NY) is placed beneath the sample to prevent powder flakes from reacting with the sample holder. While in the green state, the alumina paper is a soft felt-like material that can be easily handled and manipulated. After sintering, the alumina paper can be easily removed, even if contaminated. During sintering, however, various species from the alumina paper are released into the gas phase. To prevent the signals from these species appearing as false signals in the MS data during a sample run, an oxidation run, with air flowing past the sample holder, must be performed each time the alumina paper is replaced. This will also serve to oxidize any discolorations on the sample holder that can develop over time. However, the high oxygen content in the carrier gas will damage the filaments in the MS if it is collecting data during an oxidation run. Additionally, ceramic oxides inside the furnace will absorb oxygen in defects which will be released during future runs in low-oxygen atmospheres. Therefore, oxidation runs must be followed with blank runs, in inert atmosphere, with a heating profile no shorter than the oxidation run.

2.2.5 Mass Spectrometer

Figure 2.9 shows the layout of the primary components of the mass spectrometer. The top plate holds the operative equipment for the separation and detection of ions based on their mass to charge (m/z) ratios and is held against the vacuum manifold by the pressure differential between the high vacuum area and the surrounding atmosphere. A tee-fitting on the vacuum manifold, near the gas inlet, connects to the ionization gauge tube, used for high vacuum measurements, and the calibration valve, which controls access to a vial of PFTBA (GC/MS Checkout Standard Perfluorotributylamine 1 x 0.5

MI, 5971-60571, Agilent Technologies, Santa Clara, CA), which is used for tuning the MS. The diffusion pump maintains the high vacuum necessary for MS operation and is located at the opposite end of the vacuum manifold. The diffusion pump boils oil, (Diffusion pump oil, SantoVac Ultra, 18.5ml, 6040-0809, Agilent Technologies) which is then drawn through a jet assembly and finally directed through a series of baffles changing its flow profile. Gasses are drawn from the chamber and directed through the outlet as the oil condenses and returns to the boiler; a diagram of this process is shown in Figure 2.10. The diffusion pump is incapable of discharging gasses to atmospheric pressure so a foreline pump, with an oil trap, is required at the outlet; this also serves the purpose of creating sufficient vacuum so that the diffusion pump oil does not burn upon heating.

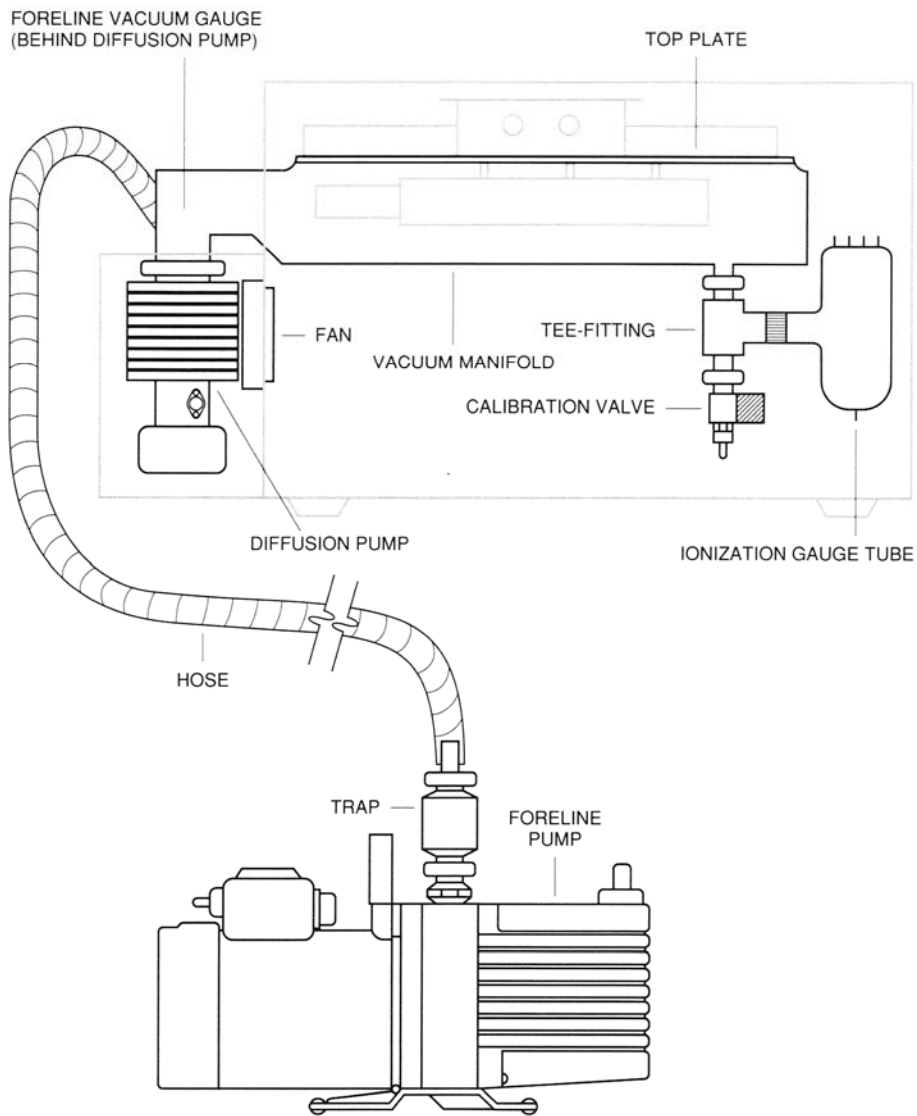


Figure 2.9: Diagram of the primary components and layout for the mass spectrometer.

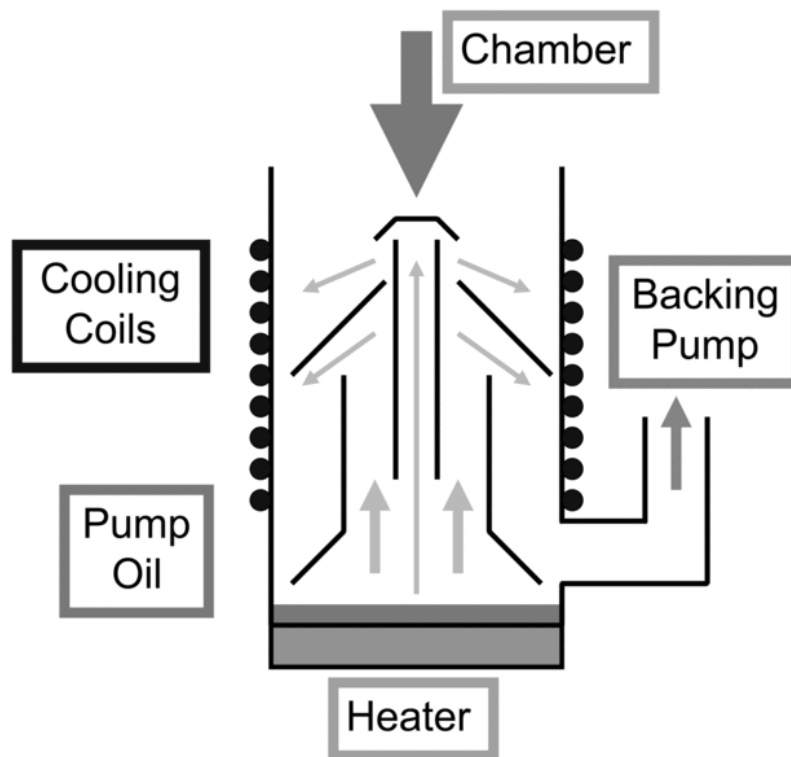


Figure 2.10: Diagram of the interior workings of an oil diffusion pump.

Figure 2.11 shows the MS top board which contains a majority of the hardware used to count and sort ions based on their m/z ratios. The interface socket is where the gas stream enters the MS and is designed to accommodate the gold plated tip on the inlet heater. This also conducts heat, aided by the gas flow, to other components of the MS. The filaments (Refurbished 5971A Filament, 05971-60140, Analytical West, Corona, CA) are located above and below the ion source and are the most frequently replaced part of the MS. Although only one filament is used at any given point in time, two are installed in case one burns out. The quadrupole mass filter is a fused silica tube with hyperbolic geometry that is used to sort ions based on their m/z ratio by applying a combined DC and RF signal to various segments of the filter. The RF coils create the RF

segment of the signal applied to the mass filter and there are two adjustment screws on the rear of the case. However, the coils only require adjustment when the top board is first installed and not during normal use. The detector, (Electron Multiplier 5971A – Old Style, 356, Manufactured by: DeTech Detector Technologies; Distributed by: Analytical West) located at the end of the mass filter, is a dynode electron multiplier which generates an electronic signal proportional to the number of ions striking it. The voltage applied to the horn of the electron multiplier is adjustable from 0 to -3000 V DC. The signal response at a given voltage degrades over time and the degradation accelerates when operating at higher voltages. The detector needs to be replaced when the signal level is low despite a maximum voltage setting.

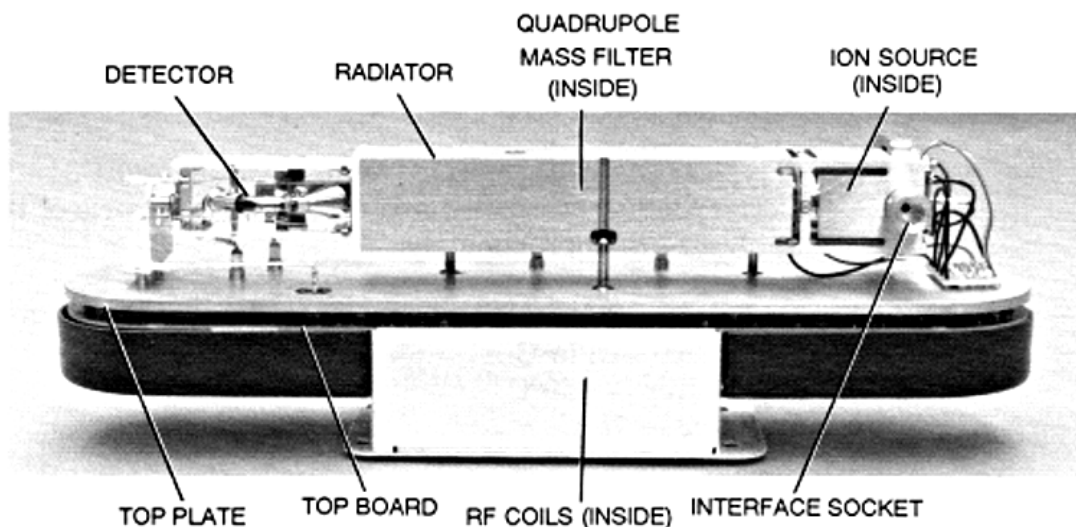


Figure 2.11: Hardware layout on the top board of the mass spectrometer.

The diffusion pump and inlet heater are the only actively heated zones of the MS. The inlet heater, shown in Figure 2.3, is necessary to heat the ion source, quadrupole mass filter, and ion detector. During MS tuning, “MS Temp” will be displayed by the

software; this value is collected at the radiator on the top board and should be between 160 and 220 °C. After the inlet heater is activated, it can take up to 4 hours for the temperature to stabilize throughout the MS and an additional 20 hours for absorbed water to be removed if the top board has been removed. The inlet heater is designed to interface with and be controlled by a gas chromatography (GC) unit, which is not present in this system. Instead, the temperature is controlled with a Variac and the 100 Ω platinum RTD in the inlet heater is read using a multimeter. The resistance of the RTD can be related to the temperature in the heater by:

$$\text{Temperature}(\text{°C}) = 2.6445 * \Omega - 265.11 \quad (2.2)$$

where Ω is the resistance of the RTD in ohms. The temperature of the inlet heater should be maintained between 250 and 320 °C, which corresponds to a setting of 90 volts on the Variac; though the temperature can sometimes vary up to 30 °C during the course of a heating cycle. In the absence of gas flow, the temperature experienced by the capillary in the center of the inlet heater is approximately 20-30 °C lower than the heater temperature indicated by the RTD reading.

MS performance is influenced by the atmosphere inside the MS vacuum manifold as well as the temperature. For example, gasses containing large amounts of oxygen and sulfur can damage the filaments over time. Once carrier gas flow has been established, it can take up to 2 hours for the MS signals to stabilize. The MS signal levels can be verified in the Manual Tune window of the MS software. According to the manufacturer, there will always be a small amount of air and water leaking into the system, and as long as the primary m/z ratios corresponding to nitrogen, 28, and water, 18, are below 10% of

the 69 peak in PFTBA, the system is adequately sealed. The diffusion pump is rated to maintain pressure while removing up to 1 mL per minute of helium, though other gasses may have different removal rates. If the inlet flow rate is faster than the pumping rate, the background signal levels, or baselines, will gradually increase over time. Furthermore helium cylinders below 500 psi have noticeably decreased purity.

There are two pressure gauges for the MS, one is located near the foreline vacuum pump, shown in Figure 2.9, and is read by the MS software during tuning, pump down and venting, while the other is the ionization gauge which has a separate controller. This gauge functions by ionizing gas molecules to establish a pressure-dependant current flow and will only operate at pressures below 10^{-3} Torr. The ionization gauge also has a degas function which passes a large current through a coiled wire inside the ionization tube in order to desorb any neutral molecules that may build up during use. The signal response for the ionization gauge is dependant on the ionization potential of the gas and is tuned for air. Helium, for example, causes a pressure reading approximately 6 times lower than the actual pressure. During operations with helium carrier gas, the ionization gauge should read 4×10^{-5} Torr or lower, which corresponds to a true pressure of 2.4×10^{-4} Torr.

2.3 Equipment Failures

Before the secondary thermocouple was installed at the vacuum port, there were two catastrophic system failures where the temperature inside the heated zone of the furnace exceeded the melting point of the mullite combustion tube, which then dripped onto the heating element and fused to the radial felt retainer. Two failure mechanisms were identified, the first being inadequate insulation on the primary thermocouple where it passes into the metal head on the dilatometer, and the second being a breakdown in the cooling system. The breakdown occurred because the fan which draws air through the cooling fins in the chiller became loose and pulled itself off the dowel so that heat was no longer being removed from the system. However, this had no impact on the pump and coolant was still flowing, thus the flow dependant shut off sensor was not tripped. Although the dowel on the chiller was retooled and the fan was reattached, the fan should be inspected each year for signs of wear. Each instance of fan failure was preceded by a squeaking sound from the chiller.

Thermal Technologies recommends that the O-rings, graphite felt and sighting and vacuum tubes be replaced whenever the furnace is disassembled. Because the furnace is not being used near its maximum temperature, this was deemed unnecessary. Thermal Technologies has stated that all of the graphite components of the furnace are constructed from IGM50 or 780GL purified graphite. Thus, if an appropriate supplier can be located, the felt retainer and possibly the heating element may be produced in house.

2.4 Procedure

One gram strontium titanate samples were uniaxially dry pressed, without binder or other organic additives, in a 1/4th inch stainless steel die. For activation energy analysis using the Master Sintering Curve (MSC) approach, a consistent green density is very important. To achieve this, the amount of powder as well as the magnitude and duration of pressure must be kept consistent. During pressing, the load was increased to an internal pressure of 600 psi and then held constant for 45 seconds. Samples had an average green length of 10.82 mm. The pressure used while pressing must be sufficient to promote green body cohesion, but if it is too high, the pressure differential when removing the sample will result in end capping, fracturing the end of the sample. An approximate pressure can be found by slowly increasing the pressure until there is a marked change in the resistance in the handle for the press. This should be near the optimum pressure for a given powder and die.

In the past, a silicone based lubricant (Dow Corning 7 Release Compound, Dow Corning, Midland, MI) was used to ensure that the plungers did not become lodged in the die during pressing. However, various m/z peaks during sintering were traced back to the lubricant rather than to the ceramic. Because of these signals, the lubricant was replaced with poly(ethylene glycol) (average $M_n \sim 200$, Sigma-Aldrich, St. Louis, MO) which is commonly used in industry. However runs performed with this lubricant experienced complications requiring the replacement of the silica capillary between the furnace and the MS. Further runs were conducted using isopropyl alcohol (IPA) as a lubricant, with the hopes that the lubricant would fully evaporate at low temperature. However, the MS

was sensitive enough to detect the trace amounts of IPA that bonded to the surface of the sample and did not evaporate. Finally, it was determined that lubricants were no longer necessary when the die and contact surfaces of the press were retooled.

The final steps before starting an experiment are to load the sample, establish gas and coolant flow and prepare the software on the MS and dilatometer computers. The sample should be loaded so that it is centered on the dilatometer plunger as shown in Figure 2.7. The atmospheres on both the shell side and tube side should be evacuated to below 0.8 mbar and back filled three times. Then gas flow rates should be set at 5 liters of nitrogen per hour on the shell side, and 135 milliliters of helium per minute, corresponding to a reading of 150 on the flow meter, on the tube side. After purging, gas must flow for one to two hours before signal levels inside the MS will reach steady state. The software settings for the dilatometer should be set as shown in table 2.2 and the method for the MS should be loaded. The MS software methods are suites of settings for data acquisition that generally remain constant across experiments and are outlined in table 2.3. Finally, the Haake constant temperature bath should be switched on to maintain the temperature of the measuring head, and the chiller will need to be activated before power can be applied to the heating element. Table 2.4 shows the various steps involved in dilatometer data analysis.

Table 2.2: Dilatometer settings for data acquisition

Setting	Value (units)	Comments
Range	2500 μm	Must match analog numbers on control board
Zero Point	85%	Allows for thermal expansion and full shrinkage
Power Output	55%	Allows for ramp rate up to 21 $^{\circ}\text{C}/\text{min}$ to 1500 $^{\circ}\text{C}$
Ramp Rate	Linear	Power output should be <40% below 1000 $^{\circ}\text{C}$
Soak	≤ 1500 $^{\circ}\text{C}$	Between sintering and melting points of material
Cooling	Same as Ramp	-- -- --
Length	~ 10 mm	Used for Piston Correction during analysis
Duration	Variable	Auto shut-off for furnace control
Max Temperature	1505 $^{\circ}\text{C}$	Auto shut-off for furnace control
Sampling Interval	20 seconds	-- -- --
Pressure Control	300 mN	Set on the control board above the thyristor

Table 2.3: Mass spectrometer settings that make up a Method

Setting	Value (units)	Comments
Mode (1)	Scan	Allows quick data collection over a range of masses
Range	3-150	M/z ratios scanned during run
N value	0-7	Data for each m/z will be collected 2^N times
Mode (2)	SIM	Selected Ion Monitoring, higher precision than Scan
Group	Up to 50	Group of masses that will be monitored for a set time
Start Time	Minutes	When collection for a group begins; 1 group at a time
Masses	Up to 30	Specific masses that will be monitored for this group
Dwell	200 ms	How long data will be collected for a given m/z
Tune File	AT12-09.U	Suite of settings for mass filter and ion collector

Table 2.4: Steps for dilatometer data analysis

Step	Setting	Comments
Signal Correction	Zero File	Time based, specified while preparing run
Signal Correction	Piston Correction	Whole trace, Alumina
Y-Smoothing	Default	-- -- --
Export	ANSI Format	Creates a file that can be opened in Excel

CHAPTER 3:

**HIGH TEMPERATURE CHEMISTRY DURING THE SINTERING
OF STRONTIUM TITANATE**

3.1 Introduction

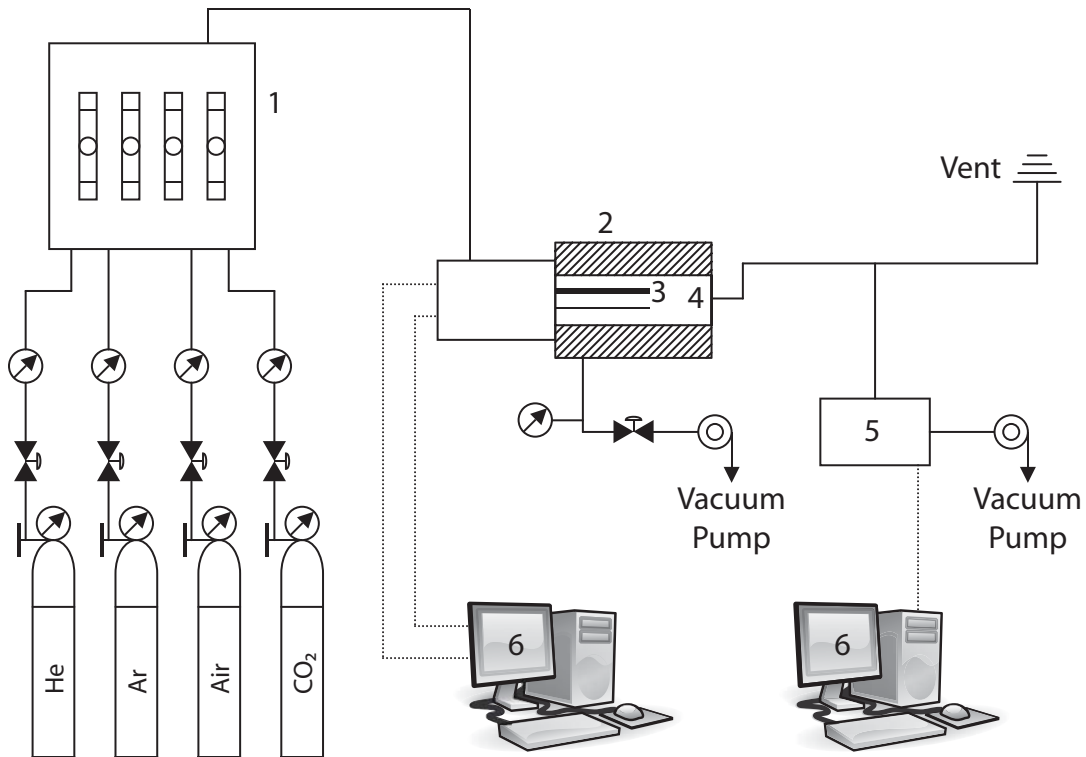
In this work, we examine the high temperature gas phase chemistry occurring during the sintering of strontium titanate using a combined dilatometer mass spectrometer (CDMS) apparatus which allows for the simultaneous measurement of the progress of sintering and species in the gas phase. The high temperature chemistry primarily occurs over two temperature regions in the mid-temperature range near the onset of sintering. Along with the evolution of carbon dioxide, two other compounds are suspected as the source of the signals. To clarify the origin of these species, we use mass spectrometer cracking patterns, natural isotopic abundances, and the decomposition behavior of model inorganic compounds.

In order to perform preliminary quantitative analysis, the primary signal response for m/z 44 and 64 are compared to signal responses from the decomposition of known amounts of carbon dioxide and sulfur dioxide, respectively. Depending on whether the source of oxygen is from the solid crystal matrix or from trace amounts of oxygen found in the gas phase, between 60% and 200% of the observed weight loss experienced by the strontium titanate sample can be attributed to these two compounds.

3.2 Experimental

The experimental apparatus consists of three sections (see Figure 3.1): the gas handling system, the furnace/dilatometer assembly, and gas analysis by mass spectrometry (MS). The gas supply section consists of cylinders and a mixing station for preparing the desired gas-phase composition. The furnace/dilatometer (L75/2000, Linseis, Germany) can be heated to 1500°C with temperature measurement by a type B thermocouple placed directly below the sample holder. The sample holder and push rod are made from alumina and the surrounding muffle tube is mullite. A slip stream from the furnace effluent is introduced via a fused silica transfer capillary (Post Nova Analytics, Salt Lake City, UT) of 0.1 mm interior diameter and 450 mm length into a quadrupole mass spectrometer (Hewlett Packard 5971A, Agilent, Santa Clara CA). The silica capillary runs through a heated interface held at approximately 320°C.

High purity helium (99.9995%) is used as the carrier gas in each experiment. Prior to the start of each experiment, the muffle tube is evacuated twice to 0.6 mbar and backfilled with helium. The gas flow rate is then set at 135 ml/min at nominally 1 atm total pressure. This flow rate is maintained for 60-180 minutes to completely purge the system and to establish flat baseline signals in the MS. Specified mass to charge, m/z , ratios and sample length change were monitored as a function of time and temperature at a constant heating rate of 14°C/min to 1500°C followed by a 20 min hold. For the carrier gas flow rate used, the transfer time from the sample location in the furnace to the MS detector is less than 10 seconds.



Legend:
 1: Flowmeters 2: Furnace 3: Sample holder 4: Thermocouple 5: Mass spectrometer 6: Computers

Figure 3.1: Schematic of the combined dilatometer/mass spectrometer apparatus showing the gas handling system, the furnace/dilatometer assembly, mass spectrometer, and data acquisition computers.

Samples were prepared from strontium titanate powder (Sigma Aldrich, Milwaukee, WI) with a nominal particle size of $<5 \mu\text{m}$ and 99% purity. Samples were fabricated by dry pressing 1.00 g of powder to a relative green density of 0.55, which is based on a theoretical density of 5.1 g/cm^3 . Calcia stabilized zirconia spacers (Machined Ceramics Inc, Bowling Green, KY) were used to prevent reaction between the strontium titanate samples and the alumina sample holder.

To identify the species evolved into the gas phase and subsequently entering the MS, three approaches were used. When an easily available compound such as carbon dioxide was suspected, the gas was introduced into the MS and the cracking pattern (CP) was determined by integrating and then normalizing intensities to the most dominant signal. For less commonly available substances or for substances that could not be easily evolved into the gas phase, either a NIST database [1] of cracking patterns or the naturally occurring isotope abundances [2] were used to aid in species identification. In other instances, the CPs were determined for the decomposition behavior of model compounds such as strontium carbonate (Sigma Aldrich), potassium bicarbonate (Sigma Aldrich), and strontium sulfate (Sigma Aldrich).

3.3 Results

Figure 3.2 shows the heating profile, the length change of the SrTiO₃ sample, and the four highest intensity signals ($m/z=28, 44, 48,$ and 64) recorded by the mass spectrometer versus time for a heating rate of $14^{\circ}\text{C}/\text{min}$ in helium gas. For times of about 0-70 min (corresponding to temperatures from $200\text{-}1100^{\circ}\text{C}$), the SrTiO₃ sample expands with a CTE value of $11.2 \times 10^{-6}/^{\circ}\text{C}$, which is consistent with literature values [3]. At approximately 70 min (1100°C), the sample begins to sinter, and ultimately experiences $\sim 17.3\%$ linear shrinkage, which corresponds to a change in fractional density from 0.55 to 0.97.

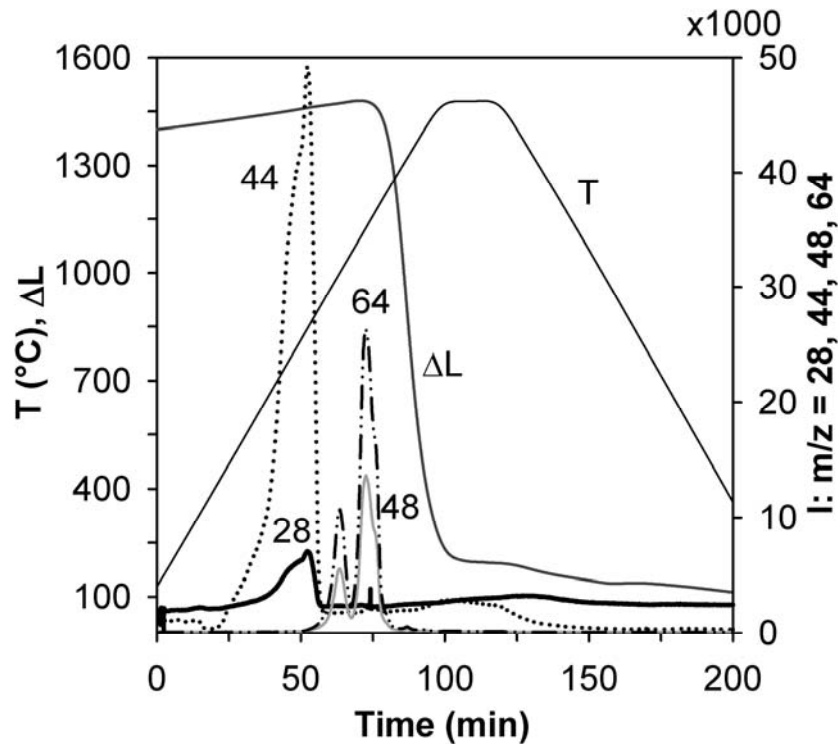


Figure 3.2: Temperature (T), scaled shrinkage (ΔL ; total shrinkage is 17.3%), and species intensity (I) versus time for 1 g of SrTiO₃ heated at $14^{\circ}\text{C}/\text{min}$ in flowing helium.

Figure 3.2 also shows that the evolution of species in the gas phase can be divided into two primary periods. The first occurs from 20-60 min (400-1000°C) where $m/z=28$ and 44 are observed with a peak temperature of 800°C at 50 min preceded by a broad low temperature shoulder, which may consist of one or more additional overlapping features. The second region of gas evolution occurs from 55-90 min (900-1400°C), where two peaks each of $m/z=48$ and 64 are observed at 1015°C and 1140°C.

To aid in the identification of the species evolved into the gas phase in the different temperature regions, the intensities of additional signals are shown in Figure 3.3. For the time period of 20-60 min (400-1000°C), Figure 3.3 (a) shows that species of $m/z=12$, 16, 28, 44, and 45 are evolved with the aforementioned single peak and low temperature shoulder, all with the same general shape. The dominant intensity at $m/z=44$ is suggestive of CO_2 evolution. To verify this assignment to CO_2 , Table 3.1 compares the normalized ratios of the measured ion intensities arising from the SrTiO_3 sample as compared to measured and tabulated CPs and to isotopes of CO_2 gas ($m/z=44$ ($^{12}\text{C}^{16}\text{O}_2$) and $m/z=45$ ($^{13}\text{C}^{16}\text{O}_2$)). In general, the measured ratios at $m/z=12$, 16, 28 and 45 arising from the sample are in good agreement as compared to the CP data for CO_2 measured with the mass spectrometer with pure CO_2 added to the carrier gas. In contrast, poorer agreement is obtained to the tabulated cracking pattern; this underscores the well-known best mode of MS analysis whereby cracking patterns should be obtained with same equipment under similar conditions, when possible.

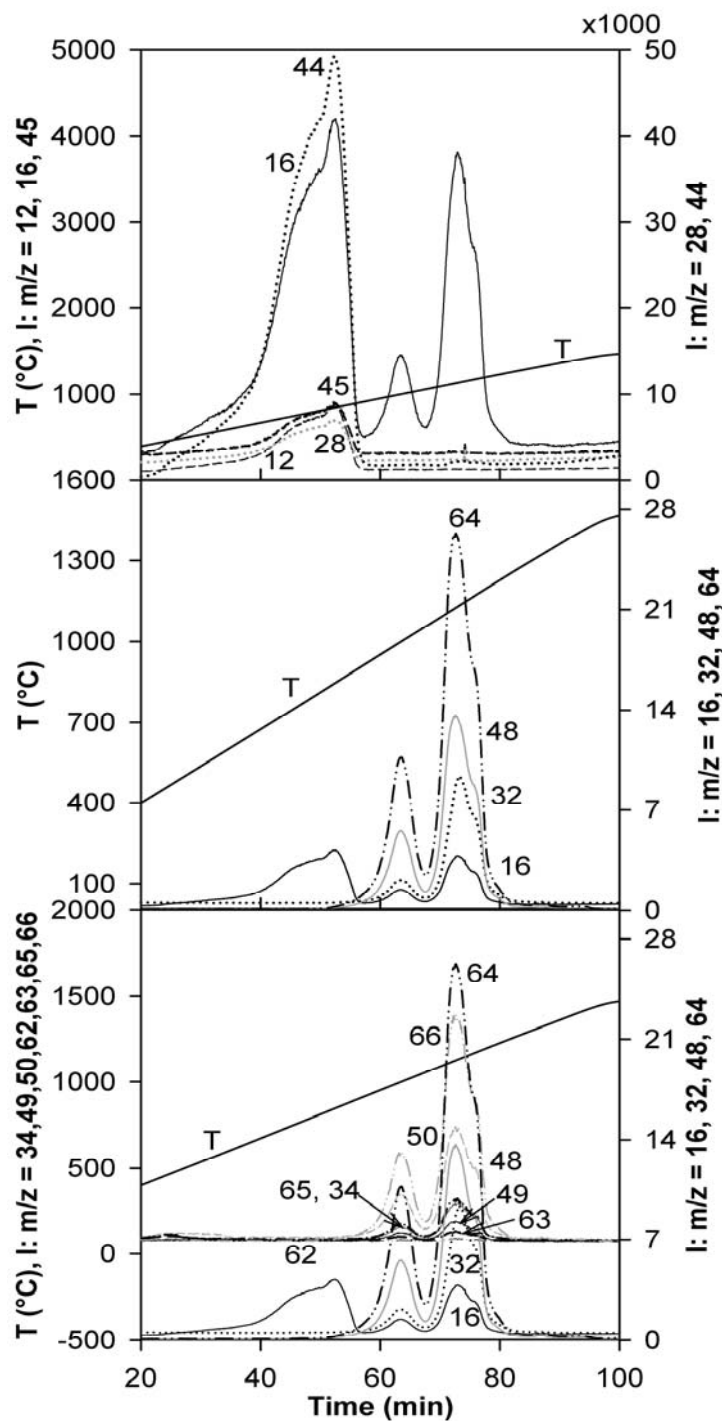


Figure 3.3: Temperature (T) and species intensity (I) versus time for SrTiO₃ heated at 14°C/min in flowing helium. a) Species with m/z ratios of 12, 16, 28, 44, and 45. b) Species with m/z ratios of 16, 32, 48, and 64. c) Species with m/z ratios of possible isotopes related to the species of m/z ratios of 16, 32, 48, and 64 in panel b).

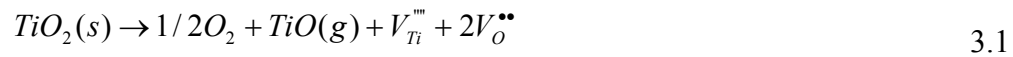
Table 3.1: Comparison of the integrated and normalized m/z ratios evolved from strontium titanate and potassium bicarbonate, and measured, tabulated [1-2], or calculated m/z ratios corresponding to cracking patterns (CP) for carbon dioxide and its isotopes.

Source	Temp (°C)	Intensity at m/z ratios normalized to m/z=44				
		12	16	28	44	45
SrTiO ₃ sample Peak 1	850	1.4	6.4	7.7	100	0.9
Measured CP for CO ₂	25	1.0	5.2	7.6	100	1.2
NIST CP for CO ₂	-	9.7	9.6	9.9	100	1.2
CO ₂ Isotopes	-				100	1.7
KHCO ₃ Peak 1	190	1.3	6.5	8.3	100	1.3
KHCO ₃ Peak 2	1050	1.1	5.4	7.1	100	1.2
Possible Compounds	-	¹² C	¹⁶ O	¹² C ¹⁶ O	¹² C ¹⁶ O ₂	¹³ C ¹⁶ O ₂

As an alternative method to verify the assignment to CO₂, a sample of KHCO₃ was decomposed at the same heating rate in helium, and for this sample two peaks were observed at 190 and 1050°C. Table 3.1 shows that the observed ratios of normalized ion intensities from both peaks during KHCO₃ decomposition agree with the measured CP for CO₂. Taken together, the results in Table 3.1 indicate that the m/z intensities seen from 400-1000°C arise from CO₂. The CO₂ at low temperature may have as its source trace organic impurities arising from processing and exposure to the ambient environment. At higher temperature, the source of CO₂ may be from residual unreacted SrCO₃, which is a common precursor used to synthesize SrTiO₃ [4]. When a sample of pure SrCO₃ was decomposed at the same heating rate, a strong family of signals at m/z=12, 16, 28, 44, and 45 were observed over the temperature range of 750-1470°C with a smaller peak between 400 and 650°C; this low temperature range overlaps the first region in Figure 3.3a. The CP of the signals from SrCO₃, however, exhibited some

discrepancies at the lower m/z ratios, which could correspond to an unknown amount of CO evolution. In addition, other (unidentified) compounds were also detected.

For the second period of gas evolution, from 55-90 min (900-1400°C), Figure 3.3 (b) shows that a family of similarly shaped peaks for m/z=64, 48, 32, and 16 are observed, whose appearance coincides with the onset of sintering. Based on these four m/z ratios, one possible source is TiO with peaks assigned as $^{48}\text{Ti}^{16}\text{O}$ (m/z=64), ^{48}Ti (m/z=48), $^{16}\text{O}_2$ (m/z=32), and ^{16}O (m/z=16). The underlying defect chemistry reaction corresponding to these species in the gas phase is thus:



where the signals at m/z=48 (Ti) and 16 (O) then presumably arise due to the cracking of TiO during ionization in the mass spectrometer. The source for such a reaction could be trace unreacted TiO₂ in the powder arising from the synthesis scheme for SrTiO₃. Alternatively, the vaporization of TiO is also a possible source, although less likely as presumably the powder was synthesized in an oxygen rich atmosphere. We note, though, that in any case it would be surprising for TiO to be detected given its low vapor pressure and the fact that the capillary between the dilatometer and mass spectrometer is at 320°C.

A second plausible reaction is the evolution of SO₂, and fragments thereof as $^{32}\text{S}^{16}\text{O}_2$ (m/z=64), $^{32}\text{S}^{16}\text{O}$ (m/z=48), ^{32}S (m/z=32), and ^{16}O (m/z=16) according to either the oxidation of trace S or S-containing species or from the decomposition of a sulfate as, respectively,





The signals at $m/z=48$ ($^{32}\text{S}^{16}\text{O}$), 32 (^{32}S) and 16 (^{16}O) would then arise as fragments of SO_2 during ionization in the MS. The presence of sulfur in the sample may not be surprising, as a standard synthesis route to SrTiO_3 is from SrCO_3 , which is derived from mined celestite (SrSO_4) [4].

To differentiate between TiO and SO_2 evolution, the fact that S, Ti, and O have different natural isotopic abundances, as given in Table 3.2, may be of use. Figure 3.3 (c) illustrates the m/z signals corresponding to a number of the isotope combinations of the species appearing in Table 3.2. Most of these signals in Figure 3.3 (c) closely mirror the trends seen for the $m/z=64$, 48, 32, and 16 signals in Figure 3.3 (b) for the time period of 55-90 min. Thus, the presence, absence, and amount of signal can next be used to distinguish between TiO and SO_2 .

Table 3.2 Species and natural isotopic abundances for S, Ti, O, and C [2]

S	Abundance	Ti	Abundance	O	Abundance	C	Abundance
32	0.9493	46	0.0825	16	0.9976	12	0.9893
33	0.0076	47	0.0744	17	0.0004	13	0.0107
34	0.0429	48	0.7372	18	0.0021		
36	0.0002	49	0.0541				
		50	0.0518				

Table 3.3 shows the integrated and normalized ratios (to the parent compounds) at $m/z=48$ and 64 for the case where TiO is suspected to be evolved from the SrTiO_3 sample. With the exception of the signals at $m/z=50$ and 66, very little agreement is seen between the observed intensity ratios and the expected ratios based on the isotopic

abundances. In addition, no signals are observed at $m/z=46$, 47, and 62, and these signals should be seen based on the expected isotopic abundances relative to the parent compounds.

Table 3.3: Comparison of the integrated and normalized m/z ratios evolved from strontium titanate and calculated m/z ratios corresponding to cracking patterns (CP) for titanium monoxide and its isotopes.

Source	Intensity at m/z ratios normalized to $m/z=48$					Intensity at m/z ratios normalized to $m/z=64$				
	46	47	48	49	50	62	63	64	65	66
SrTiO ₃ sample	0.0	0.0	100	0.9	4.8	0.0	0.2	100	1.0	4.9
TiO Isotopes	11.2	10.1	100	7.3	7.5	11.2	10.1	100	7.4	7.2
Possible Elements	⁴⁶ Ti	⁴⁷ Ti	⁴⁸ Ti ³² S ¹⁶ O	⁴⁹ Ti ³³ S ¹⁶ O	⁵⁰ Ti ³⁴ S ¹⁶ O	⁴⁶ Ti ¹⁶ O	⁴⁷ Ti ¹⁶ O	⁴⁸ Ti ¹⁶ O ³² S ¹⁶ O ₂	⁴⁹ Ti ¹⁶ O ³³ S ¹⁶ O ₂	⁵⁰ Ti ¹⁶ O ³⁴ S ¹⁶ O ₂

Table 3.4 shows the observed intensity ratios, normalized to $m/z=64$, for the case where SO₂ is suspected to be evolved. Based on the expected isotopes for sulfur, the signals at $m/z=65$ and 66 are present in approximately the correct amounts. In addition, the level of the agreement between the measured cracking pattern and a tabulated pattern [1] for SO₂ is quite good, with exception of the signal at $m/z=32$, which can be accounted for by the release of oxygen gas as shown in Equation (3.2b).

To provide further insight into the identity of the compound, a sample of SrSO₄ was heated at 14°C/min in helium. As seen in Figure 3.4, SrSO₄ decomposes between 75-140 min (from 1200°C and through the soak period at 1470°C), which is at a higher temperature than was observed for the corresponding m/z signals in Figures 3.3 (b) and

3.3 (c). Table 3.4 compares the integrated normalized signals observed at nine m/z values for the SrTiO₃ and SrSO₄ samples; the level of agreement at all intensities is quite high and decomposition of the SrSO₄ sample also shows the elevated intensity at m/z=32, again in accord with Equation (3.2b). In summary, the agreement between the intensities arising from the SrTiO₃ and SrSO₄ samples is quite high, which suggests that the evolution of sulfur dioxide underlies the family of peaks seen in Figure 3.3. This reaction presumably arises from residual trace celestite used in the synthesis scheme to produce SrTiO₃.

Table 3.4: Comparison of the integrated and normalized m/z ratios evolved from strontium titanate, strontium sulfate, and tabulated [1-2] or calculated m/z ratios corresponding to cracking patterns (CP) for sulfur dioxide and its isotopes.

Source	Temp (°C)	Intensity at m/z ratios normalized to m/z=64								
		16	32	34	48	49	50	64	65	66
SrTiO ₃ sample	1000	11.4	28.1	0.8	51.4	0.4	2.5	100	1.0	4.9
NIST SO ₂ CP	-	5.9	10.4	0.4	49.2	0.4	2.2	100	0.9	4.9
SO ₂ Isotopes	-							100	0.9	4.9
SrSO ₄ sample	1500	8.7	32.0	0.6	45.8	0.4	2.2	100	0.9	5.0
Possible Compounds	-	¹⁶ O	¹⁶ O ₂ ³² S	³⁴ S	⁴⁸ Ti ³² S ¹⁶ O	⁴⁹ Ti ³³ S ¹⁶ O	⁵⁰ Ti ³⁴ S ¹⁶ O	⁴⁸ Ti ¹⁶ O ³² S ¹⁶ O ₂	⁴⁹ Ti ¹⁶ O ³³ S ¹⁶ O ₂	⁵⁰ Ti ¹⁶ O ³⁴ S ¹⁶ O ₂

In the assignment of species to SO₂ evolution, however, a discrepancy exists in that the family of signals arising from SrSO₄ decomposition in Figure 3.4 appears at higher temperature as compared to Figure 3.3. This suggests that the evolution of trace SO₂ from the SrTiO₃ sample is more facile than for the pure SrSO₄; this may arise

because the SO_2 from the SrTiO_3 sample is not present as bulk crystalline SrSO_4 . Alternatively, the more facile evolution of SO_2 may be related to the diffusion and surface area changes that occur during the sintering process, which is just initiating at 70 min (1100°C).

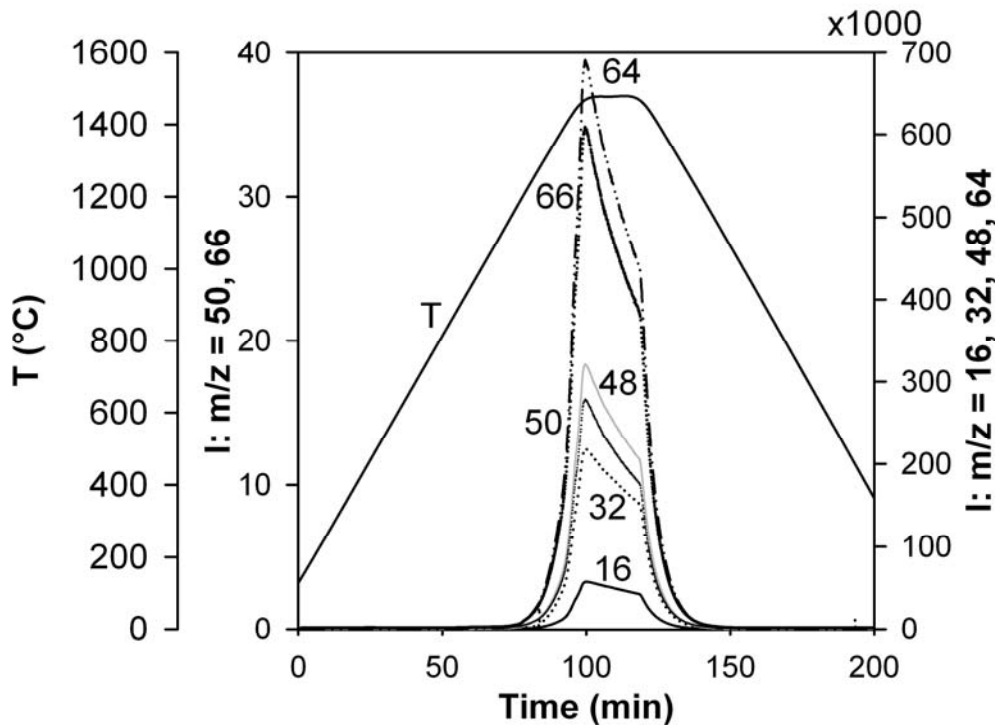


Figure 3.4: Temperature (T) and species intensity (I) versus time for 0.25 g of SrSO_4 heated at $14^\circ\text{C}/\text{min}$ in flowing helium.

The CDMS apparatus can also be used to examine other aspects of the synthesis scheme, the powder purity, and sintering. As mentioned earlier, a common route to SrTiO_3 is from conversion of SrSO_4 to SrCO_3 and then subsequent reaction with TiO_2 . Figure 3.5 compares the CO_2 signals arising from SrTiO_3 , SrCO_3 , and SrSO_4 , and a number of features common to two or more of the compounds are evident. Both SrTiO_3

and SrSO_4 evolve CO_2 between 40-55 min (720-930°C), and both have a small peak at ~60-62 min (~950°C), which may have a common source from trace carbonate present in both. At ~80 min (1200°C), however, a peak is common to both SrCO_3 , and SrSO_4 but not to SrTiO_3 . Above 85 min (1300°C), SrCO_3 has two sharp high temperature peaks whereas SrSO_4 has one; these may or may not be related. In summary, the appearance of CO_2 with peaks of the same shape and at the same temperature from different compounds suggests that the kinetics are the same, which in turn then implies that the structural environment from which the CO_2 emanates may be similar as well. The traces in Figure 3.5 may thus be used to track both the purity and possibly the environment of carbonate species.

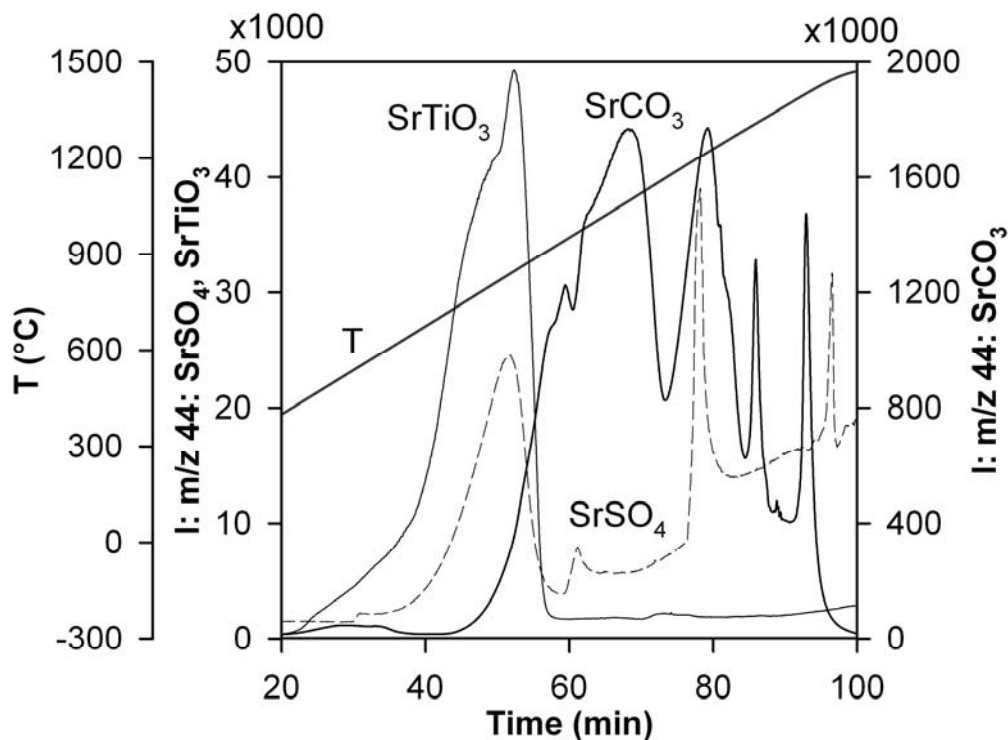


Figure 3.5: Temperature (T) and species intensity (I) for $m/z=44$ versus time for samples of SrTiO_3 , SrCO_3 , and SrSO_4 heated at $14^\circ\text{C}/\text{min}$ in flowing helium.

The CDMS apparatus can also be used to assess some aspects of the role of powder compaction in the dry pressing operation. Figure 3.6 shows the MS signals for $m/z=16, 32, 44, 48$ and 64 for SrTiO_3 present as a loose powder. As compared to Figures 3.2 and 3.3, the signal corresponding to CO_2 ($m/z=44$) is similar, regardless of whether the sample is pressed or not. In contrast, the relative peak heights for the family of curves for $m/z=16, 32, 48,$ and 64 , which correspond to SO_2 evolution, are different in that for the loose powder, the low temperature peaks are sharply attenuated as compared to the curves for the pressed sample in Figures 3.2 and 3.3. This may arise because the SO_2 evolves from different environments such as from the near surface region of particles and from deeper within primary particles. Dry pressing of the powder may lead to fragmentation of the some primary particles which leads to the more facile evolution of SO_2 at low temperature. For the loose powder, however, SO_2 appears in abundance at higher temperature, which coincides with the diffusional processes and surface area changes occurring at the onset of sintering.

Finally, in addition to providing cracking patterns, the decomposition of the model compounds $\text{KHCO}_3, \text{SrCO}_3,$ and SrSO_4 can be used to help quantify the weight loss corresponding to the different regions of gas evolution in the SrTiO_3 sample. To accomplish this, integration of the area under the curve of a dominant signal (e.g., $m/z=64$ in Figure 3.4 for SO_2) and the stoichiometric weight loss from the reaction $\text{SrSO}_4 \rightarrow \text{SrO} + \text{SO}_2 + 1/2 \text{O}_2$ can be used to relate signal intensity to moles of SO_2 . A similar procedure can be used for the decomposition behavior of KHCO_3 and SrCO_3 to relate intensity to the moles of CO_2 . Table 3.5 shows that with this procedure, the estimated

weight loss from SrTiO₃ due to CO₂ and SO₂ evolution ranges from 60-200% of the observed weight loss. This range arises partially because of the uncertainty in the source of the oxygen for the evolution of CO₂ and SO₂ (see Equation 3.2), *i.e.*, does the oxygen arise from traces in the gas phase or from the sample itself. In addition, some of the weight loss arises from adsorbed water, which occurs below 500°C. Based on the analysis in Table 3.5, the conservative sensitivity of the apparatus, for a 1 g sample, is approximately 100 ppm by weight or 1 μmole.

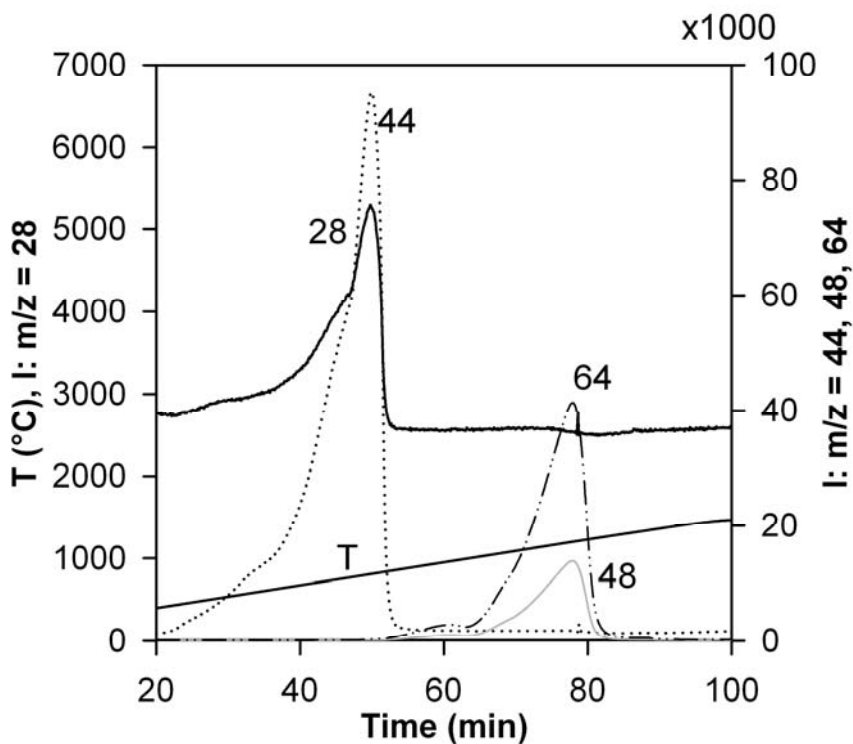


Figure 3.6: Temperature (T) and species intensity (I) for SrTiO₃ in loose powder form heated at 14°C/min in flowing helium.

Table 3.5: Weight losses during heating for potassium bicarbonate, strontium carbonate, and strontium sulfate used to calibrate the MS for the strontium titanate sample. All weights normalized to 1 g of sample.

	KHCO₃	SrCO₃	SrSO₄	SrTiO₃
Observed Weight Loss (g)	1.00	0.309	0.419	0.0069
Calculated CO ₂ Evolved (mol)	9.99×10^{-3}	7.03×10^{-3}		2.54×10^{-4} #
Calculated SO ₂ Evolved (mol)			5.24×10^{-3}	3.65×10^{-5}
Calc. Min. CO ₂ and/or SO ₂ Weight Loss (g)*	0.120	0.084	0.168	0.0042
Calc. Max. CO ₂ and/or SO ₂ Weight Loss (g)*	0.440	0.309	0.336	0.0135

*Minimum (maximum) weight loss corresponds to oxygen arising from the gas phase (from the solid).

#Calculated from strontium carbonate.

3.4 Discussion

In this work, it was desired to examine the high temperature chemistry that occurs during a sintering cycle by combining a dilatometer with a characterization technique for qualitatively and quantitatively analyzing species in the gas phase. The decision to use mass spectrometry over gas chromatography was based on the following considerations. Gas chromatography is useful for identifying different species because when a mixture is present, the GC column effects a separation so that individual species elute separately into the detector. By using known calibration compounds and amounts, quantitative analysis of unknowns can be performed. A limitation of GC is that because of possibly lengthy separation times, the analysis can only be performed at selected, discrete times and not on a continuous basis in real time.

Mass spectrometry, on the other hand, allows for essentially continuous real-time analysis. A limitation of MS, however, is that because gas phase species are not separated before entering the quadrupole filter, multiple compounds of a given mass-to-charge ratio are indistinguishable. In addition, fragmentation during ionization in the MS leads to additional signals. To overcome these limitations, a number of options are available for species identification. Measured cracking patterns, reference cracking patterns, isotopic abundances, and model compounds have all been used in this work to aid in the identification of gas-phase species, and the use of multiple methods increases the certainty of the species assignment. In addition, the use of model compounds can be used to semi-quantitatively calibrate the instrument, and in the future the accuracy of the CDMS apparatus may be improved.

For the SrTiO₃ material examined in this work, high temperature reactions are seen to occur in the early part of the sintering cycle. At lower temperatures, carbon dioxide is observed, the source of which may be trace organic contamination and trace strontium carbonate. It is further expected that when binders are present in a sample, the kinetics of their decomposition can be observed as well, and this information can presumably be used to develop heating cycles for binder removal. At higher temperature, a family of signals was evident, which was ultimately assigned to the evolution of SO₂. This species may arise from residual celestite used to synthesize SrTiO₃. The sensitivity of the apparatus, together with the capability to monitor signals continuously in real time, suggests that the CDMS can be used as a quality control tool for simultaneously assessing powder chemistry and sintering behavior.

Finally, the appearance of species in the gas phase at the onset of sintering raises a number of interesting questions, and in future work we will determine if the high temperature chemistry accelerates, inhibits, or is independent of the sintering process. In addition, we will attempt to quantify in what manner the gas phase chemistry affects the defect chemistry, defect equilibria, and the resulting electrical properties of SrTiO₃. Such information can then be used to compare to other strontium titanate powders, derived for example from other synthesis routes such as sol-gel, hydrothermal, or from nanosized powders. Ultimately, the results of *in-situ* gas phase chemistry and sintering studies can be tied to microstructure and properties determined *ex-situ* to help complete the structure-processing-property paradigm.

3.5 Conclusions

The high temperature chemistry accompanying the sintering of strontium titanate has been examined using a combined dilatometer/mass spectrometer system. At both low and intermediate temperature, the dominant species observed was carbon dioxide. In addition, high temperature chemistry was also observed which occurred at the onset of sintering; the observed species were ultimately related to the evolution of sulfur dioxide from the strontium titanate sample. The identification of species in the gas phase was accomplished by using measured and tabulated cracking patterns and cracking patterns calculated from known isotopic abundances. Model compounds were also used to aid in distinguishing between possible compounds. The CDMS unit was also demonstrated to have high sensitivity, on the order of 100's of ppm by weight (1 μ mole), and high m/z resolution, in that isotope species differing by 1 atomic mass unit were easily distinguished.

3.6 References

1. <http://webbook.nist.gov/chemistry/>; NIST Chemistry WebBook, NIST Standard Reference Database Number 69, June 2005 Release (accessed on Oct. 26, 2007).
2. IUPAC Commission on Atomic Weights and Isotopic Abundances, *Pure Appl. Chem.* **70**, 217-235 (1998).
3. D. Ligny and P. Richet, "High-Temperature Heat Capacity and Thermal Expansion of SrTiO₃ and SrZrO₃ Perovskites," *Phys. Rev. B*, **53** [6] 3013-22 (1996).
4. "Strontium and Strontium Compounds"; *Kirk-Othmer Encyclopedia of Chemical Technology*, 27 Volume Set, 5th Edition. Wiley Knowledge for Generations, New Jersey, 2004.

CHAPTER 4

ANALYTIC METHODS FOR DETERMINATION OF ACTIVATION ENERGY USING THE MASTER SINTERING CURVE APPROACH

4.1 Introduction

The changes that take place during sintering can be seen as a thermally activated kinetic process similar to many others. One of the fundamental aspects of each kinetic process is the activation energy, which is the size of the energy barrier preventing the “reactants,” in this case the ceramic green body, from converting to the “products,” meaning the dense sintered body. In thermally activated processes, the activation energy is the energetic barrier preventing the reaction from moving forward and is generally higher than the energy of either the products or the reactants. There are many techniques available to calculate activation energies from experimental data, though most require detailed knowledge, or assumptions, about the kinetic mechanism behind the reaction. However, the master sintering curve (MSC) approach for sintering [1] can be used as a “model free” technique in that the activation energy of a process can be calculated with very little knowledge of the mechanism.

Unfortunately, the MSC involves an integral that can not be evaluated analytically. In this paper, we use the method of the Lee and Beck [2] to effectively approximate the value of the integral and create an analytical approximation of the MSC. This expression can not only be used to find the activation energy, but can be substituted back into a mechanistic equation and mathematically manipulated to calculate unknown variables. Moreover, these equations and the methodology of the MSC can theoretically be applied to other thermally activated processes which can be a useful tool to compare the evolution of gas phase species scene in the previous chapter with the process of sintering.

4.2 Theory

4.2.1 Master Sintering Curve Method

The master sintering curve is an integral method of kinetic analysis for calculating the activation energy of sintering. The method is “mechanism free” in that the activation energy is obtained without assuming an underlying mechanistic process such as first-order kinetics, second order kinetics, etc. It was originally developed by Su and Johnson [1] and is based on the combined stage sintering model of Hansen *et al.*[3] The latter model treats the shrinkage which occurs during sintering as arising from mass transfer due to two diffusion processes, namely grain boundary diffusion and volume diffusion. The length change, L , that occurs during sintering is given as a linearly additive sum of these two diffusion processes as:

$$-\frac{dL}{Ldt} = \frac{\gamma \Omega}{k_b T} \left(\frac{\Gamma_v D_v}{G^3} + \frac{\Gamma_b \delta D_b}{G^4} \right) \quad (4.1)$$

where t is the time, γ is the surface energy, Ω is the atomic volume, k_b is the Boltzmann constant, T is the absolute temperature, and G is the mean grain diameter. The coefficients for volume (subscript v) and grain-boundary diffusion (subscript b) are, respectively, D_v and D_b , and δ is the average width of a grain boundary. The Γ quantities are lumped scaling functions which relate driving forces, mean diffusion distances, and other geometric features of the microstructure that influence the sintering rate in terms of the mean grain diameter; these quantities are more thoroughly explained in Hansen *et al.*[3] From the results of experiments, the Γ functions depend on density but are independent of the heating schedule. Although the values for all of the variables in the combined stage sintering model can be obtained in principle either from

experiment or from theory with simplified models, the calculated and experimental values are usually significantly different. Furthermore, experimental determination is a time-consuming process and impractical on an industrial scale.

Because the quantities Γ and G are functions of density (or microstructure) alone, Equation (4.1) can be rearranged so that the left-hand side (lhs) contains all the properties dependant on the microstructure and the right-hand side (rhs) is dependant only on the heating schedule and activation energy. Provided sintering is dominated by a single mechanism, either volume or grain boundary diffusion, the factoring of Equation (4.1) into a lhs and rhs leads to:

$$lhs = \Phi(\rho) \equiv \frac{k_b}{\gamma \Omega D_0} \int_{\rho_0}^{\rho} \frac{(G(\rho))^n}{3\rho\Gamma(\rho)} d\rho \quad (4.2)$$

$$rhs = \Theta(T(t)) \equiv \int_0^t \frac{1}{T} \exp\left(-\frac{Q}{RT}\right) dt \quad (4.3)$$

$$\Phi(\rho) = \Theta(T(t)) \quad (4.4)$$

where D_0 is the pre-exponential factor for D_v or δD_b , depending on which is the dominant diffusion mechanism, Q is the activation energy of diffusion, R is the universal gas constant, and ρ is the fractional density of the sample relative to the maximum theoretical density. The exponent n is 3 or 4 for volume grain boundary diffusion, respectively. Due to the underlying assumptions, Equations (4.2) and (4.3) are only valid when the microstructural evolution is dependent on density alone, which is most true for relative densities in the range of 0.6 to 0.9 during sintering. The relationship between ρ and $\Phi(\rho)$ defines the MSC, and is unique for each powder and green body forming

method, including a fixed green density. Since Equation (4.3) depends on time and temperature, both of which are simple to monitor in an experiment, $\Theta(T(t))$ is known if Q is known or can be approximated. The equality in Equation (4.4) can then be used to obtain the value of $\Phi(\rho)$ without determining the individual factors comprising Equation (4.2) or making any further assumptions. Because Equation (4.3) is dependant on time and heating rate, and Equation (4.2) is not, when $\ln(\Theta(T(t)))$ is plotted versus ρ for data collected at different heating rates, the separate curves will collapse to a single curve only if the true activation energy has been established. For a linear heating rate, β , the temperature evolves as $T=T_o+\beta t$ where T_o is the initial temperature, and thus

$$\beta = \frac{dT}{dt} \quad (4.5)$$

which can then be used to eliminate time from Equation (4.3).

The “model- or mechanism-free” basis of the MSC can be applied to a wide range of thermally activated processes and requires no knowledge of the underlying mechanism other than the thermally activated process has a single activation energy and is independent of the heating profile. This can be represented by replacing $\Phi(\rho)$ with the generic $F(\rho)$ in Equation (4.3), which when combined with Equation (4.5) yields:

$$F(\rho) = \int_{T_o}^T \frac{1}{\beta T} \exp\left(-\frac{Q}{RT}\right) dT \quad (4.6)$$

We note that in the original MSC method, the activation energy in Equation (4.3) or (4.6) is obtained numerically.

4.2.2 Method of Lee and Beck

Prior to the development of the MSC methodology for determining the activation energy of sintering, Lee and Beck [2] had analyzed the kinetics of coal decomposition obtained using thermogravimetric analysis (TGA). They represented the kinetics of decomposition for a solid with a thermally activated (Arrhenius-type) expression as:

$$\frac{d\rho}{dt} = A \exp\left(\frac{-Q}{RT}\right) f(\rho) \quad (4.7)$$

where A is the pre-exponential factor, ρ is the decomposed fraction of solid (the conversion), and $f(\rho)$ is a function which depends on the reaction mechanism. Combining Equations (4.5) and (4.7) and then integrating between the initial and final temperatures and conversions yields:

$$\frac{\beta}{A} \int_{\omega_0}^{\omega} \frac{d\rho}{f(\rho)} = \int_{T_0}^T \exp\left(-\frac{Q}{RT}\right) dT = \frac{RT^2}{Q} \exp\left(-\frac{Q}{RT}\right) \Big|_{T_0}^T - \int_{T_0}^T \frac{2RT}{Q} \exp\left(-\frac{Q}{RT}\right) dT \quad (4.8)$$

The right-hand side of Equation (4.8) is the result of integration by parts and leads to the same integral of the exponential function in Q , which cannot be obtained analytically. By rearranging the terms containing Q in Equation (4.8) and grouping the integrals together, it can be shown that:

$$\int_{T_0}^T \exp\left(-\frac{Q}{RT}\right) dT + \int_{T_0}^T \frac{2RT}{Q} \exp\left(-\frac{Q}{RT}\right) dT = \int_{T_0}^T \left(1 + \frac{2RT}{Q}\right) \exp\left(-\frac{Q}{RT}\right) dT = \frac{RT^2}{Q} \exp\left(-\frac{Q}{RT}\right) \Big|_{T_0}^T \quad (4.9)$$

For moderate temperatures and large activation energies, $2RT/Q$ is far less than unity, thus making $(1+2RT/Q)$ approximately equal to one and therefore approximately constant. When $(1+2RT/Q)$ is thus factored from the integral, Equation (4.9) can be rearranged to:

$$\int_{T_0}^T \exp\left(-\frac{Q}{RT}\right) dT = \left[\frac{\frac{RT^2}{Q} \exp\left(-\frac{Q}{RT}\right)}{1 + \frac{2RT}{Q}} \right]_{T_0}^T \quad (4.10)$$

which can then be substituted into Equation (4.8) to yield:

$$\int_{\rho_0}^{\rho} \frac{d\rho}{f(\rho)} = \frac{A}{\beta} \left[\frac{\left(\frac{RT^2}{Q}\right) \exp\left(-\frac{Q}{RT}\right)}{\left(1 + \frac{2RT}{Q}\right)} - \frac{\left(\frac{RT_0^2}{Q}\right) \exp\left(-\frac{Q}{RT_0}\right)}{\left(1 + \frac{2RT_0}{Q}\right)} \right] \equiv \frac{A}{\beta} (\lambda_T - \lambda_{T_0}) \quad (4.11)$$

where λ_T and λ_{T_0} denote the two terms in square brackets. When relative density is substituted for conversion, Equation (4.11) can be used with a kinetic mechanism or model to directly find the activation energy of sintering:

$$F(\rho) \equiv \int_{\rho_0}^{\rho} \frac{d\rho}{f(\rho)} = \frac{A}{\beta} \int_{T_0}^T \exp\left(-\frac{Q}{RT}\right) dT = \frac{A}{\beta} (\lambda_T - \lambda_{T_0}) \quad (4.12)$$

Some common kinetic models and their integrated forms are shown in Table 4.1.

Table 4.1. Kinetic mechanisms with their integrated forms.

Kinetic Model	$f(\rho)$	$F(\rho)$
Zero order	$(1 - \rho)^0$	$\rho - \rho_0$
First order	$(1 - \rho)^1$	$\ln(1 - \rho_0) - \ln(1 - \rho)$
Second order	$(1 - \rho)^2$	$1/(1 - \rho) - 1/(1 - \rho_0)$

Equation (4.12) can be further simplified if, when compared to λ_T , the value of λ_{T_0} is assumed to be small (which is often the case for T_0 moderately removed from T and for large activation energies). This approximation leads to

$$F(\rho) = \frac{A}{\beta} \lambda_T = \frac{A \left(\frac{RT^2}{Q} \right) \exp\left(-\frac{Q}{RT}\right)}{\left(1 + \frac{2RT}{Q}\right)} \quad (4.13)$$

which can be rearranged to

$$\ln\left[\frac{F(\rho)}{T^2}\right] = \ln\left[\frac{AR}{\beta(Q+2RT)}\right] - \frac{Q}{RT} \quad (4.14)$$

When $\ln[F(\rho)/T^2]$ is plotted versus $1/T$, linear behavior results, and the slope is proportional to $-Q/R$; this Q value can then be used with Equation (4.14) and the known mechanism to obtain the value of the pre-exponential factor.

4.2.3 Application of the Lee and Beck Approximation to the MSC Method

The contribution of this paper is to use the approximation developed by Lee and Beck [2] to obtain the activation energy of the kinetic of sintering analytically, instead of numerically as is typically done. We note, however, that Equation (4.3) has a $1/T$ term not present in Equation (4.6) and thus the method of Lee and Beck [2] must be modified slightly. First, the definition of a linear heating rate from Equation (4.5) is substituted into Equation (4.3) and integration by parts then yields:

$$\Theta(T(t)) = \frac{1}{\beta} \int_{T_0}^T \frac{1}{T} \exp\left(-\frac{Q}{RT}\right) dT = \frac{1}{\beta} \left(\frac{1}{T} \int_{T_0}^T \exp\left(-\frac{Q}{RT}\right) dT - \int_{T_0}^T \int_{T_0}^T \exp\left(-\frac{Q}{RT}\right) dT \right) \left(-\frac{1}{T^2}\right) dT \quad (4.15)$$

where the integral from the Lee and Beck expression now appears twice. Combining Equation (4.15) with the term defined in Equation (4.11) yields:

$$\Theta(T(t)) = \frac{1}{\beta} \left(\frac{\lambda_T}{T} + \frac{R}{(Q+2RT)} \int_{T_0}^T \exp\left(-\frac{Q}{RT}\right) dT \right) \quad (4.16)$$

which once again contains the integral from the Lee and Beck expression. Combining Equation (4.16) with Equation (4.11) yields the final analytic MSC expression:

$$\Theta(T(t)) = \frac{1}{\beta} \left(\frac{\lambda_T}{T} + (\lambda_T - \lambda_{T_0}) \frac{R}{Q} \frac{1}{(1 + 2RT/Q)} \right) \quad (4.17)$$

or in expanded form:

$$\Theta(T(t)) = \frac{1}{\beta} \left(\frac{\left(\frac{RT}{Q} \right) \exp\left(-\frac{Q}{RT}\right)}{\left(1 + \frac{2RT}{Q}\right)} + \left[\frac{\left(\frac{RT^2}{Q} \right) \exp\left(-\frac{Q}{RT}\right)}{\left(1 + \frac{2RT}{Q}\right)} - \frac{\left(\frac{RT_0^2}{Q} \right) \exp\left(-\frac{Q}{RT_0}\right)}{\left(1 + \frac{2RT_0}{Q}\right)} \right] \frac{R}{(Q + 2RT)} \right) \quad (4.18)$$

All the equations for the master sintering curve can now be summarized as:

$$\begin{aligned} \frac{k_b}{\gamma \Omega D_0} \int_{\rho_0}^{\rho} \frac{(G(\rho))^n}{3\rho\Gamma(\rho)} d\rho &\equiv \Phi(\rho) = \Theta(T(t)) \\ &\equiv \int_0^t \frac{1}{T} \exp\left(-\frac{Q}{RT}\right) dt \approx \frac{1}{\beta} \left(\frac{\lambda_T}{T} + (\lambda_T - \lambda_{T_0}) \frac{R}{Q} \frac{1}{(1 + 2RT/Q)} \right) \end{aligned} \quad (4.19)$$

We next illustrate how the approximation on the right hand side of Equation (4.19) allows for use of analytical expressions to obtain Q instead of numerical integration of the exponential function.

4.3 Results and Discussion

To demonstrate how Equation (4.19) can be used, density versus temperature data were simulated with second order kinetics (see Table 4.1) at three linear heating rates of 21, 14, and 7 °C/min, at each of three activation energies, namely, 250, 450, and 650 kJ/mol, by numerically integrating the MSC expression:

$$\frac{1}{1-\rho} - \frac{1}{1-\rho_0} = \int_{T_0}^T \frac{A}{\beta T} \exp\left(-\frac{Q}{RT}\right) dT \quad (4.20)$$

In each simulation, A was equal to 10^{19} /min. Figure 4.1 shows the three curves generated for $Q = 450$ kJ/mol; the shape of these curves is qualitatively similar to the density profiles obtained in sintering experiments.

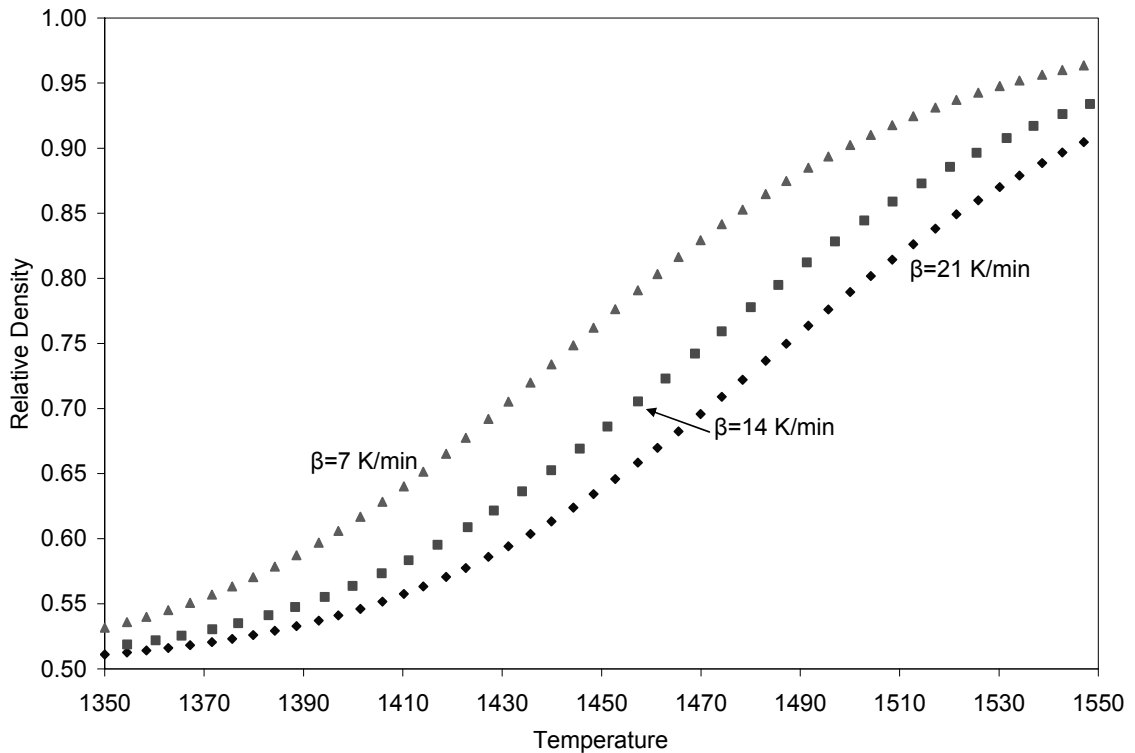


Figure 4.1: Data simulated using second order kinetics from Equation (4.20) at three different linear heating rates with an activation energy of 450 kJ/mol.

Activation energies for each data set were then calculated using the MSC method with three different equations used to represent $\Theta(T(t))$. First, Equation (4.3) was integrated numerically using the trapezoidal rule with step sizes of 0.01, 0.001 and 0.0001 relative density. For the simulations generated with an activation energy of 450 kJ/mol, disagreement in calculated activation energies between the three step sizes was less than 0.0003 kJ/mol. For ease of calculation, a step size of 0.01 relative density was chosen for the remaining simulations and techniques. In the second approach, the analytic expression in Equation (4.17) was used. The third equation was obtained by replacing the $1/T$ quantity in Equation (4.3) with a logarithmic mean value that could then be removed from the integral, thereby allowing for direct use of the Lee and Beck expression. For ease of comparison, these three equations are repeated here as:

$$\ln[\Theta(T(t))] = \ln \left[\int_{T_0}^T \frac{1}{\beta T} \exp\left(-\frac{Q}{RT}\right) dT \right] \quad (4.21)$$

$$\ln[\Theta(T(t))] = \ln \left[\frac{1}{\beta} \left(\frac{\lambda_T}{T} + (\lambda_T - \lambda_{T_0}) \frac{R}{Q} \frac{1}{(1 + 2RT/Q)} \right) \right] \quad (4.22)$$

$$\ln[\Theta(T(t))] = \ln \left[\frac{\ln \frac{T}{T_0}}{\beta(T - T_0)} (\lambda_T - \lambda_{T_0}) \right] \quad (4.23)$$

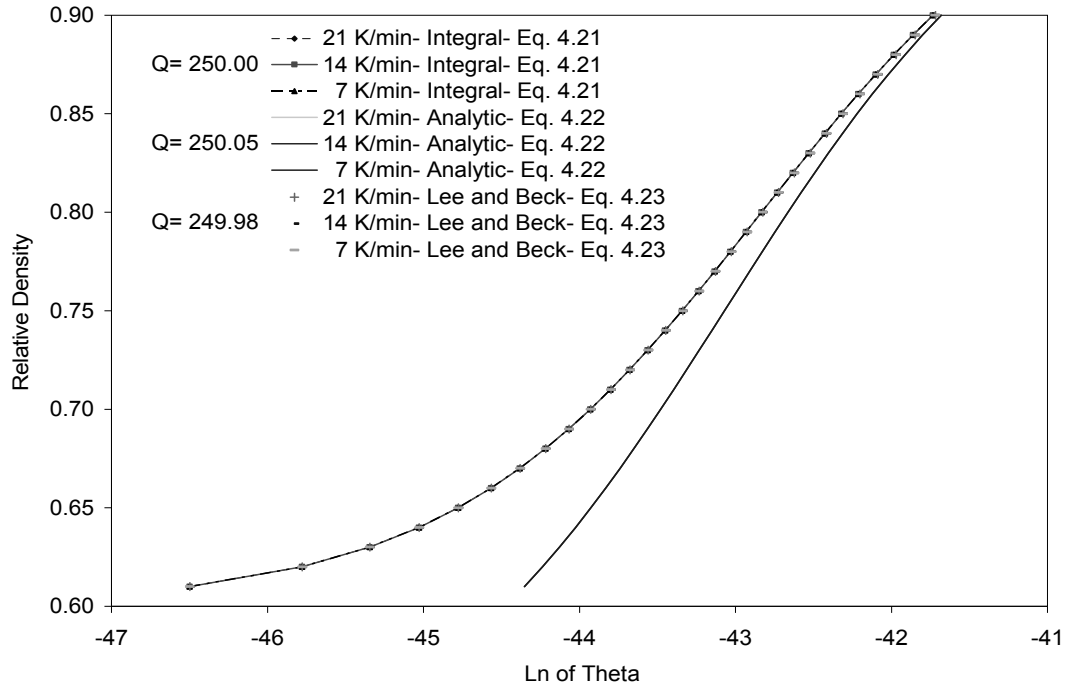
For each of the three equations used to represent $\Theta(T(t))$, the same procedure for determining the activation energy was followed. First, the simulated data were graphed with temperature as a function of relative density and a fifth order polynomial fit was constructed over the range of $\rho = 0.6$ to $\rho = 0.9$. This was done so that temperature and $\Theta(T(t))$ values could be calculated at discrete values of ρ for direct comparison at the

different heating rates. The absolute values of the differences in $\Theta(T(t))$ at the different heating rates were summed and then the Q values for each equation were varied using a generalized reduced gradient (GRG) nonlinear optimization code until the sum reached a minimum.

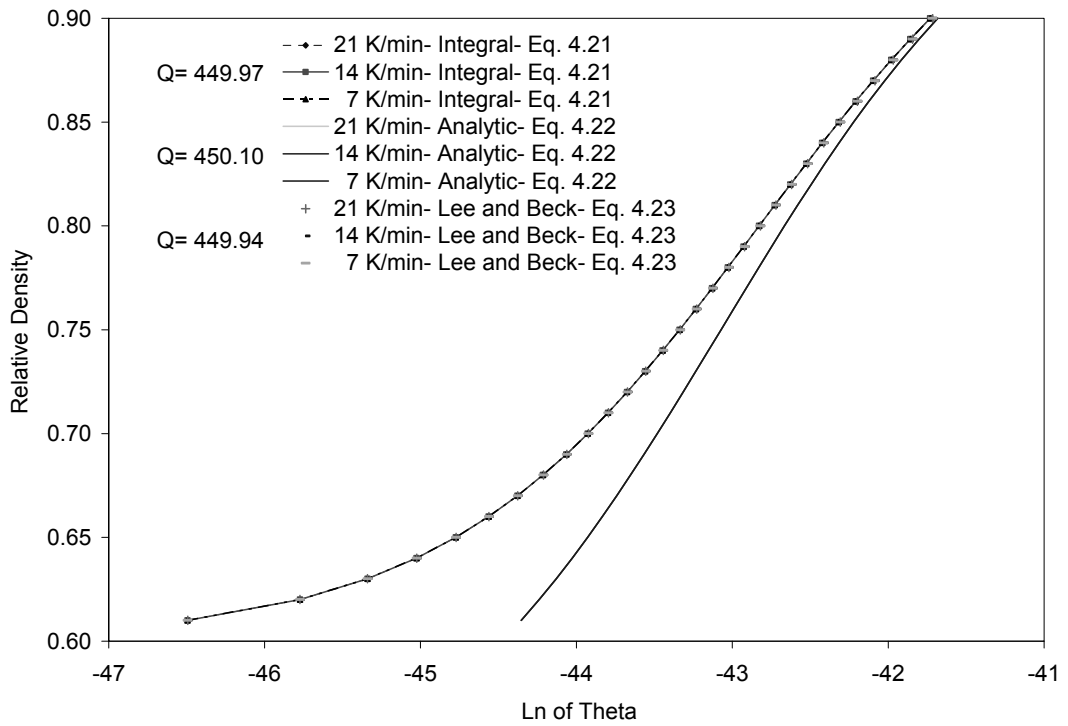
Figure 4.2 shows the MSCs calculated by the three methods at three heating rates for each activation energy, *e.g.*, there are nine curves in each panel. For each method, namely Equations (4.21)-(4.23), the data for the three heating rates collapse to a single curve. In addition, the curves obtained from Equations (4.21) and (4.23) are virtually indistinguishable whereas the curves obtained from Equation (4.22) are offset relative to the other two at each relative density. Additionally, the $\Theta(T(t))$ values are the same regardless of activation energy because all the simulations were generated with the same kinetic model and A value, which means that Q/T , at a given relative density, were consistent down to the 7th decimal point, for each heating rate; this equality of $\Theta(T(t))$ values can most readily be seen from Equation (4.20).

Table 4.2 compares the original Q values used to simulate the data with the calculated Q values determined from Equations (4.21)-(4.23). Not surprisingly, numeric integration (Equation (4.21)) produced the most accurate results, in part because the equation involves no approximations and thus the degree of accuracy depends only on the step size used. However, both approximate analytic equations were able to produce activation energies within 0.08% of the input value for all simulations. In addition, even

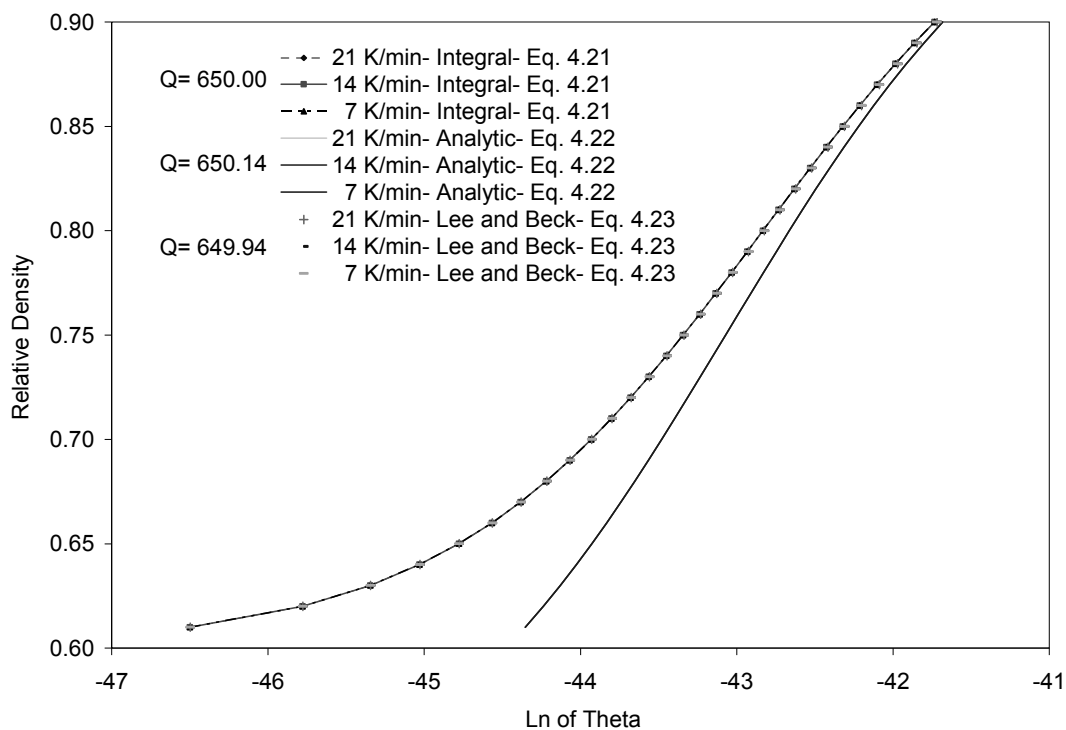
though the curves in Figure 4.2 from Equation (4.22) are different from the curves from the other two methods, the activation energies are nearly the same in all instances.



A)



B)



C)

Figure 4.2: MSCs for simulations created with Equation (4.20) at A) $Q=250$ kJ/mol, B) $Q=450$ kJ/mol, and C) $Q=650$ kJ/mol. In each figure, nine curves are shown representing the three heating rates which were each analyzed with Equations (4.21), (4.22) and (4.23). The results from numeric integration and the Lee and Beck approach, Equations (4.21) and (4.23), are virtually indistinguishable from each other.

Table 4.2: Activation energies determined by the three methods for different input Q values.

Input Q value (kJ/mol)	Numeric Integral Equation 4.21 (kJ/mol)	Analytic MSC Equation 4.22 (kJ/mol)	Lee and Beck Equation 4.23 (kJ/mol)
250	250.00	250.05	249.98
450	449.97	450.10	449.94
650	650.00	650.14	649.94

Upon further analysis of the results obtained from Equation (4.22), it became apparent that the equation was dominated by the λ_T / T term. Because of this, T_0 , and therefore the lower limit of integration, has very little impact on the calculated $\Theta(T(t))$ value. To compare the functionality of Equation (4.22) to the other methods, the entire range of sintering, starting in the green state, should be analyzed. Unfortunately, the polynomial fit required to set temperature as a function of relative density can not accurately recreate the behavior of the simulated data outside of the $0.6 \leq \rho \leq 0.9$ range, and without temperature and $\Theta(T(t))$ values for a consistent set of density values, this method of calculating the MSC cannot be performed. However, this limitation can be avoided if the equation used to generate the simulated data can be rearranged so that ρ is the independent variable. Unfortunately, this can not be done with either Equation (4.20) or a similar second order equation based on Equation (4.22). Therefore, simplifying Equation (4.22) to the dominating term with second order kinetics yields:

$$\frac{1}{1-\rho} - \frac{1}{1-\rho_0} = \frac{A\lambda_T}{\beta T} \quad (4.24)$$

which can then be solved for temperature as a function of density thereby allowing for calculation of the activation energy without the need for a polynomial fit. Figure 4.3 shows a comparison of data generated with Equation (4.20) and Equation (4.24) for an activation energy of 450 kJ/mol and a heating rate of 14 °C/minute. The overlap of the data sets suggests that Equation (4.24) is an accurate approximation of Equation (4.20).

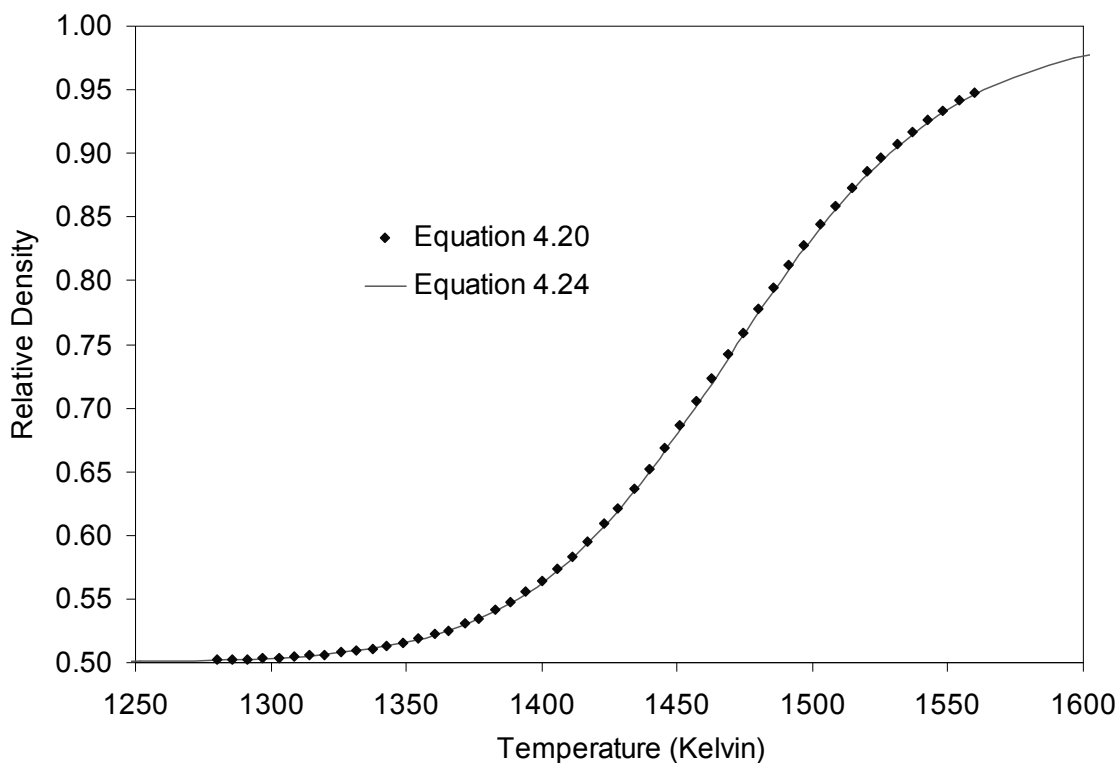


Figure 4.3: Comparison graph of temperature and density data generated for simulations ran with an activation energy of 450 kJ/mol at a linear heating rate of 14 °C/minute using Equations (4.20) and (4.24).

Density data generated with Equation (4.24) were next analyzed with Equations (4.21), (4.22), and (4.23) as well as the simplified form of Equation (4.22) shown here:

$$\ln[\Phi(\rho)] = \ln\left(\frac{\lambda_T}{\beta T}\right) \quad (4.25)$$

Data was generated for 50 relative densities over the $0.5 \leq \rho \leq 0.99$ range. Values for $\Theta(T(t))$ were next calculated with each of the four equations, and activation energies were found using the technique outlined earlier. Figure 4.4 shows one MSC curve generated with each equation for an activation energy of 450 kJ/mol. Additionally, a line

demarking $\rho = 0.6$ was added to illustrate that the $\Theta(T(t))$ values obtained from Equation (4.22) were consistent with the values from Figure 4.2 above that value. With this simulation, instead of the T_0 values corresponding to a relative density of 0.6, T_0 corresponded to a relative density of 0.5006. This change leads to a difference of approximately 170 °C in T_0 values, and despite this small difference, all four MSC equations now overlap over the entire range. Although all equations for $\Theta(T(t))$ produced very accurate Q values, Equation (4.25) produced the value closest to the original input value, likely because it is based on to the equation used to generate the data. Thus, the discrepancy in Figure 4.2 between the curves given by Equations (4.21) and (4.23) versus Equation (4.22) can be attributed to the insensitivity of Equation (4.22) to the value of T_0 used. When T_0 is sufficiently low, as was done in the analysis leading to Figure 4.4, then this discrepancy in the curves no longer exists.

In addition to the results for the simulations described above, density versus temperature data were also generated with $\pm 2\%$ random noise added to the density values, and these data are shown in Figure 4.5. These curves were then analyzed using Equations (4.21)-(4.23) and (4.25), and the results for Q with and without noise are summarized in Table 4.3. In all instances, the activation energy determined was within $\sim 2\%$ of the value of $Q=450$ kJ/mol used to generate the data. The most accurate values of the activation energy were obtained by Equations (4.23) and (4.25), where the latter is an approximation to the former. Once again, the MSC curves (not shown here) generated by Equations (4.21) and (4.23) agreed well with each other, although they do not return as accurately the values used to simulate the data. Equations (4.22) and (4.25), however, did

yield the most accurate values of Q , and this may arise because these two equations do not have a strong influence from T_0 meaning $\Theta(T(t))$ for each data point is calculated independently from all other data points.. The data in Table 4.3 thus indicate that the analytical expressions derived in this work are robust enough to use on real data which has noise.

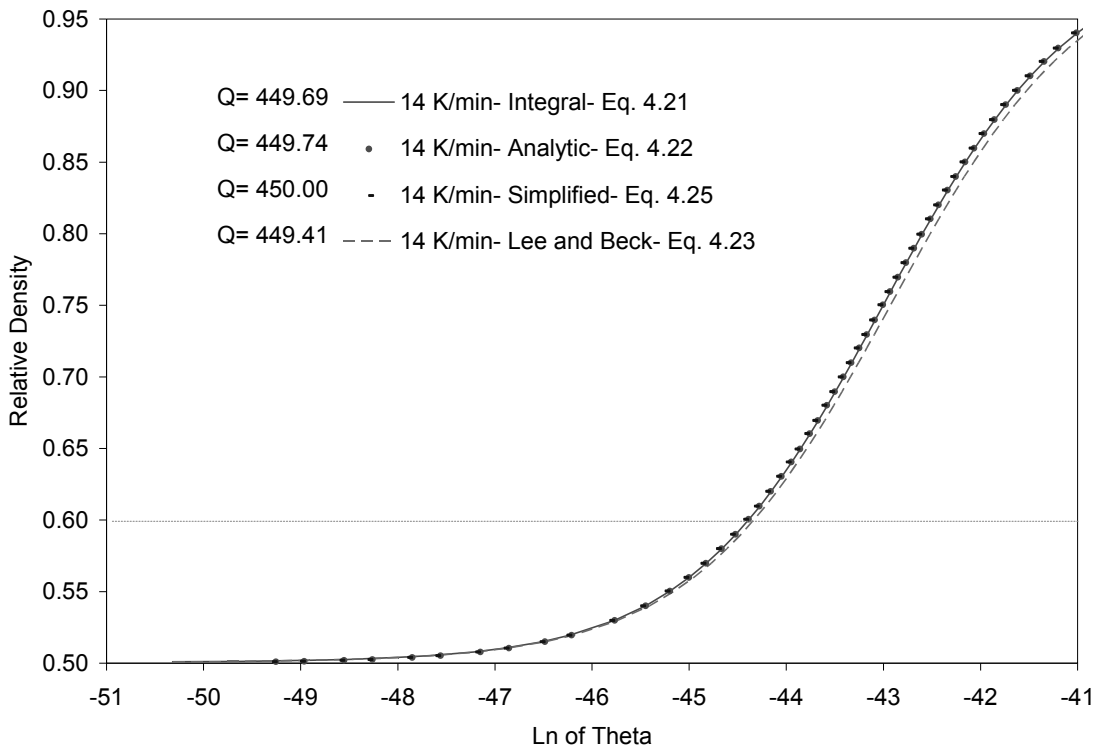


Figure 4.4: MSCs for a simulation generated using Equation (4.24), a simplified form of the Analytic Expression. For clarity, only a single MSC for each equation has been shown. Activation energies evaluated with lower limits of integration close to room temperature. A line has been added to demark a relative density of 0.6 for comparison with earlier figures.

Table 4.3: Activation energies determined for density data simulated with $Q=450$ kJ/mol with and without 2% noise.

Data	Equation 4.21	Equation 4.22	Equation 4.23	Equation 4.25
Without Noise	449.97	450.10	449.94	450.31
With 2% Noise	440.78	448.42	440.50	448.42

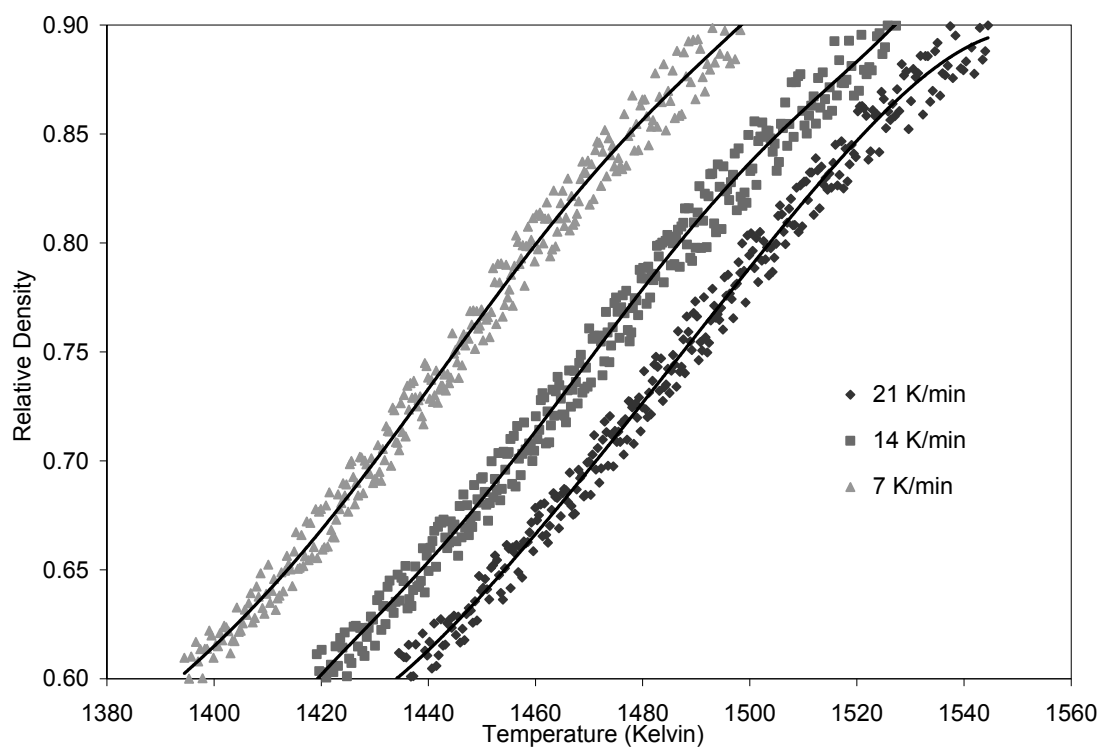


Figure 4.5: Temperature/Density data for the $Q = 450$ kJ/mol simulation with $\pm 2\%$ noise added.

Finally, we note that in general, the MSC method is a useful integral method of kinetic analysis because no knowledge of the underlying kinetic mechanism or model is required. All of the analytical equations presented herein reproduce the activation

energies to a high degree of accuracy; Equation (4.23) is especially beneficial in that it also quite accurately reproduces the MSC profile with density obtained by numerical integration, *e.g.*, Equation (4.21). In principle then, the analytical equations reproduce not only the expression for $\Theta(T(t))$, namely the value of the integral to determine the activation energy, but also the expression for $\Phi(\rho)$, namely the value of the integral of the underlying kinetic mechanism. Thus, as kinetic models or mechanisms become available for describing the kinetics of sintering via the evolution of density, such models can be tested for accuracy via the analytical equations presented here.

As an example of this idea, density versus temperature data were simulated for a given activation energy with a second order mechanism, and then these data were analyzed using Equation (4.23), which makes no assumptions about the underlying kinetic mechanism. If it is then assumed that the underlying kinetics are either first order or second order, and the pre-exponential factor is known, then plots of $\ln(\Phi(\rho))$ versus temperature can be prepared. As seen in Figure 4.6, the dependence of $\ln(\Phi(\rho))$ on temperature is well described for the second order case but not for the first order case. Thus, the analytical expressions developed in this work can be used to help discriminate between competing mechanisms, as is often done in kinetic analysis.

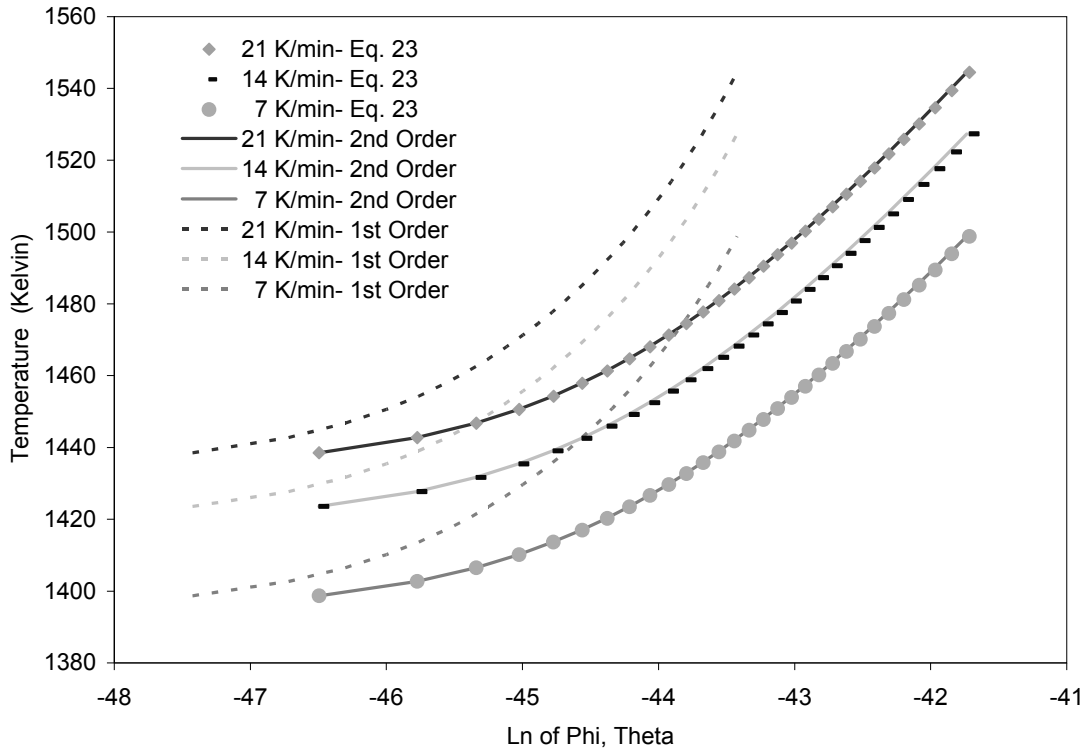


Figure 4.6: Comparison of Equation (4.23) to first and second order kinetics from Table 4.1.

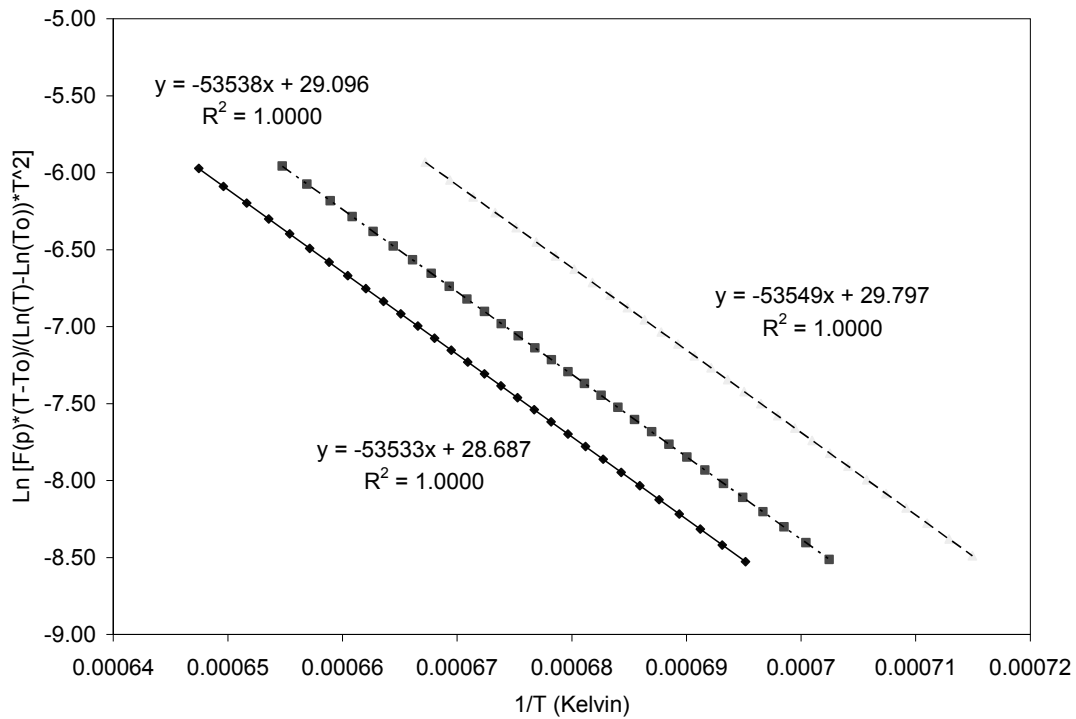
For the analysis conducted above, it was necessary to have available the value of the pre-exponential factor, which is related to the grouping of constant values in Equation (4.2). The analytical equations given above, however, also afford a method to obtain the pre-exponential factor when the mechanism is known. To perform this analysis, we follow the procedure outlined by Equations (4.13) and (4.14), where we use Equation (4.23) without the λ_0 term to describe $F(\rho)$. The equation, after algebraic rearrangement, becomes:

$$\ln \left[\frac{F(\rho)(T - T_o)}{(\ln T - \ln T_o) T^2} \right] = \ln \left[\frac{AR}{\beta(Q + 2RT)} \right] - \frac{Q}{RT} \quad (4.26)$$

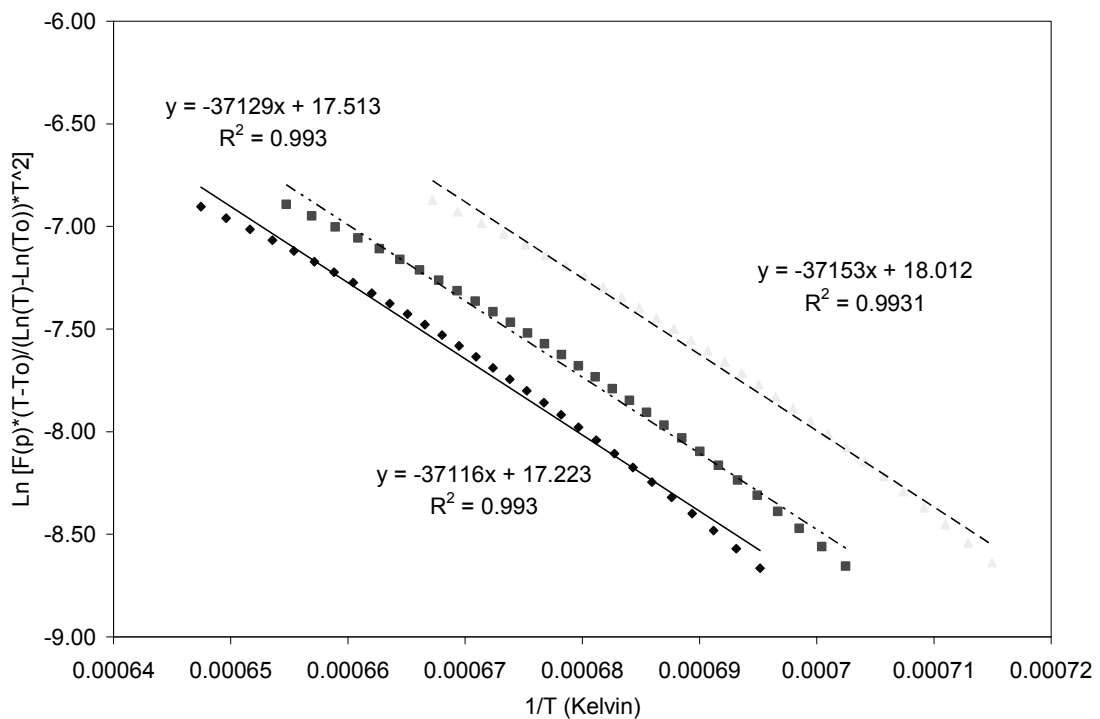
When the left-hand side is graphed versus $1/T$, the slope of the equation is given by $-Q/R$. Figure 4.7 (a) demonstrates this linear behavior for density data simulated for second order kinetics with $Q=450$ kJ/mol and $A=10^{19}$ min⁻¹ and then analyzed with $F(\rho)$ given by second order kinetics. This graphical method of analysis leads to a value of Q within approximately 1% of the value used to simulate the data, as shown in Table 4.4. The resulting pre-exponential is of the correct order of magnitude and is within 30% of the input value. If the incorrect mechanism for $F(\rho)$ is assumed, however, non-linear behavior results (See Figure 4.7 (b)) and both the activation energy and the pre-exponential factor are very inaccurate.

Table 4.4: Calculated activation energies and pre-exponential values from linear analysis of simulated data using 1st Order and 2nd Order kinetic approximations.

	Q	A ($\beta = 7$ K/min)	A ($\beta = 14$ K/min)	A ($\beta = 21$ K/min)
2 nd Order	445.16	3.45×10^{18}	3.42×10^{18}	3.41×10^{18}
1 st Order	308.74	1.86×10^{13}	2.26×10^{13}	2.54×10^{13}



A)



B)

Figure 4.7: Equation (4.26), graphed with (a) 2nd Order, and (b) 1st Order, kinetic approximations so that the activation energy can be determined from the slope.

4.4 Conclusions

Several analytic expressions have been developed to replace numerical integration of the integral occurring in the Master Sintering Curve approach. All of the expressions lead to accurate values of the activation energy within 1.5%. When noise is present in the data, the calculated activation energies were less accurate, though still quite good, and two approximations produced closer values than numeric integration. Equation (4.25) is a very simple mathematical expression that can be used to calculate activation energies of thermally activated systems using the model-free method of the MSC approach. It will also produce a consistent MSC curve, similar to that produced by numeric integration starting at a density close to the green density of a sample, regardless of what data points are used. Equation (4.23) is only slightly more complex and is capable of reproducing the results of numeric integration over any given range while maintaining the influences of the lower limit of integration. Because this is a simple expression, which can be analytically manipulated in ways that the original integral expression, Equation (4.3), cannot be, Equation (4.23) has the potential to be a useful tool for discriminating between kinetic mechanisms or for determining kinetic mechanisms when the other is known.

4.5 References

1. H. Su, and D. L. Johnson, Master Sintering Curve: A Practical Approach to Sintering, *J. Am. Ceram. Soc.*, **79** [12] 3211-17 (4.1996).
2. T. V. Lee, and S. R. Beck, A New Integral Approximation Formula for Kinetic Analysis of Nonisothermal TGA Data, *AIChE J.*, **30** [3] 517-519 (4.1984).
3. J. D. Hansen, R. P. Rusin, M. Teng, and D. L. Johnson, Combined-Stage Sintering Model, *J. Am. Ceram. Soc.*, **75** [5] 1129-35 (4.1992).
4. K. G. Ewsuk, and D. T. Ellerby, Analysis of Nanocrystalline and Microcrystalline ZnO Sintering Using Master Sintering Curves, *J. Am. Ceram. Soc.*, **89** [6] 2003-09 (4.2006).
5. S. Kiani, J. Pan, and J. A. Yeomans, A New Scheme of Finding the Master Sintering Curve, *J. Am. Ceram. Soc.*, **89** [11] 3393-3396 (4.2006).
6. Y. Kinemuchi, and K. Watari, Dilatometer Analysis of Sintering Behavior of Nano-CeO₂ Particles, *J. Eur. Ceram. Soc.*, **28** 2019-2024 (4.2008).
7. M. H. Teng, Y. C. Lai, and Y. T. Chen, A Computer Program of Master Sintering Curve Model to Accurately Predict Sintering Results, *West. Pac. Earth Sci.*, **2** [2] 171-180 (4.2002).
8. A. Mohanram, G. L. Messing, and D. J. Green, Densification and Sintering Viscosity of Low-Temperature Co-Fired Ceramics, *J. Am. Ceram. Soc.*, **88** [10] 2681-89 (4.2005).

CHAPTER 5

CONCLUSIONS AND FUTURE WORK

5.1 Conclusions

The Combined Dilatometry/Mass Spectrometry (CDMS) system is an effective tool to measure the rate of sintering while simultaneously providing information on the evolution of species in the gas phase. For optimal performance of the mass spectrometer (MS), the atmospheric composition must be precisely controlled and the pressure must be kept below 2.4×10^{-4} Torr. The installation of the mullite combustion tube insulates the furnace components from oxidizing atmospheres around the sample holder, but increases the risk of meltdown and appears to participate in side reactions on the side exposed to the graphite components of the furnace. The change from a leak valve to a silica transfer capillary has greatly reduced the transfer time from the furnace to the MS by providing a less complex flow path; however we have lost the ability to quickly change the flow rate or seal the vacuum manifold.

The CDMS was used to examine the sintering behavior of strontium titanate, and two bands of high temperature chemistry have been observed in the mid temperature range just before the onset of sintering. Based on comparisons of cracking patterns, ion abundances and the products of decomposition of model compounds, the two species observed were identified as being carbon dioxide and sulfur dioxide. Furthermore, quantitative analysis of the MS signal levels reveal that between 60% and 200% of the observed weight loss experienced by the strontium titanate sample can be attributed to these two compounds.

The method of Lee and Beck was applied to the integral appearing the master sintering curve (MSC) approach to generate 3 analytic approximations of the equation. These three equations, along with numeric integration, were used to back out the activation energies of simulated sintering data. In addition to being used to calculate the apparent activation energy of sintering, these equations can be applied to other thermally activated processes with mechanisms that are independent of heating schedule; for example, to calculate the activation energy of combustion for the impurities found the strontium titanate samples. Finally, these equations can be substituted for the integral in mechanistic equations and then mathematically manipulated to help determine the value of various unknowns.

5.2 Future Work

There are aspects of the CDMS process that could benefit from further refining. For example, it would also be beneficial to replace the mullite combustion tube with one made out of alumina. While these are available through Linseis, this has yet to be done due to pricing concerns. This change would not only increase the maximum operating temperature of the equipment, but might also eliminate the blue buildup seen around the combustion tube and on the heating element. Linear and axial shrinkage of the samples has been shown to not be equal. This occurs regularly with some powders and pressing techniques, but might also be influenced by the pressure exerted by the piston, and this phenomena could warrant further study. Quantitative analysis could be improved by more precise weight readings; ideally taken in-situ through thermo-gravimetric analysis. This could be done in successive runs of similar samples if a more uniform and consistent forming method for the green body was used. This could be coupled with runs performed in either oxidizing or reducing atmospheres which has been shown to not only affect gas phase chemistry but also the mechanics of sintering.

However, this would necessitate other changes as our MS is not designed to operate with other carrier gasses, and oxidizing atmospheres also degrade the filaments, but provided that the pressure and signal levels are below certain values, data collection is still possible. Due to the flow characteristics of different carrier gasses, both through the silica capillary and their removal by the diffusion pump, different capillaries would be required for each gas in order to avoid exceeding 2.4×10^{-4} Torr in the vacuum manifold. This could be remedied by reinstalling the dosing valve. If the valve could be externally

supported, then the inlet heater would not need to be removed and the system might retain some of the increased precision that was seen after installing the capillaries. Another possible change for the furnace/MS interface would be to replace the silica capillary with a gas chromatography (GC) column. While this would complicate real time analysis and vastly increase the transfer time from the furnace to the MS, it could be highly useful for data analysis by separating different species in the gas phase before they enter the MS. Though it will not be as clean gas injection, the input method generally used for GC/MS experiments, transfer times can be approximated by comparing when the signal appears with the current capillary and when it appears after flowing through the GC column. The effectiveness of this technique is currently unclear as most GC units use an oven to vary the temperature during separation experiments and this may not be possible when examining the effluent from the furnace.

There are also a large number of different materials and processing techniques that can be studied with the CDMS. Experiments are already being performed with barium titanate, which still shows peaks for carbon dioxide and sulfur dioxide as well as unknown signals at m/z 78. Additionally, as the sulfur dioxide evolution has been found to be influenced by whether the powder has been pressed or not, would there be differences between powders of the same material but with different particle sizes? However, the most interesting variation could be to study the effects from doping the powder before sintering. For example, the strength and oxidation resistance of ZrB_2 can be significantly improved through doping with SiC, and the sintering mechanics of the system can be improved through the addition of B_4C . The gas phase chemistry of these individual

powders can be studied, and compared to the activity that occurs when they are combined. This knowledge could potentially help to refine the formulation process or provide further understanding as to why these physical differences occur.

Finally, the thermal kinetics of sintering and the evolution of species in the gas phase can be studied to look for possible interaction between the phenomena. For example, will greater amounts of sulfur impurities increase, decrease or have no effect on the apparent activation energy of sintering? The impurities could also be removed by long soaks at moderate temperatures to see if the activation energy is affected.

APPENDIX A

DILATOMETER SIGNAL CORRECTION ANALYSIS

A.1 Introduction

During the analysis of each experiment, the dilatometer software performs a number of signal corrections to account for the apparent length change that occurs during a heating cycle, regardless of whether or not a sample is present. These corrections are primarily performed using the data from a zero file run, a run with no sample in the dilatometer, which is specific to each machine, and to the ambient conditions of the lab. The zero file must also be corrected for the length of the sample, because the presence of the sample means that less of the piston is inside the heated zone of the furnace.

This appendix details the signal correction calculations carried out by the dilatometer software and introduces an equation that can be used to manually reproduce the corrections. There are also examples of the data files used to perform the corrections as well as comparisons of the results from different application techniques, and explanations as to when each technique should be used. For example, to perform temperature based zero file analysis, the zero file must be symmetric for both heating and cooling; and even a small difference in pre-run temperature can cause signal artifacts when using time based zero file analysis.

A.2 Background

Two data files are used by the dilatometry software during signal correction: the zero file, which is a record of the length change of the equipment without a sample; and the piston correction, which corrects the zero file for the length of the sample and less of the piston being within the heated zone of the furnace. The piston correction file is a function of the coefficient of thermal expansion (CTE) of the piston material, in our case, alumina, and is shown in Figure A.1. The units are in percent change per unit length of the sample; for example, at 1200 °C the value in the piston correction file is 1.0 %. So for a 10 mm sample, 0.01 is multiplied by the length of the sample, resulting in a 100 micron correction.

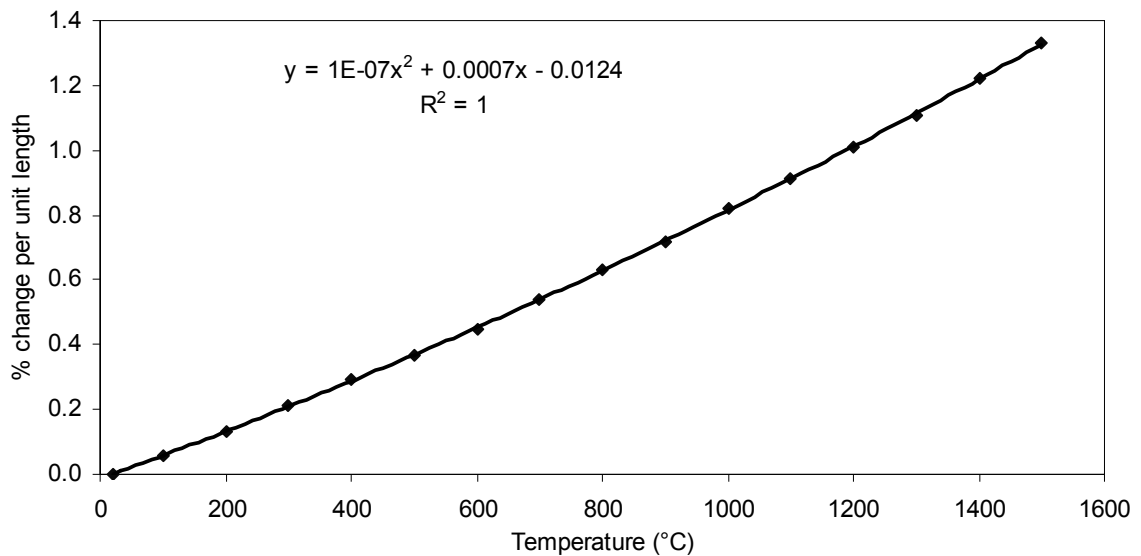


Figure A.1: Alumina Piston Correction File, provided by Linseis software, with best-fit line and equation.

To prevent samples from reacting with the alumina sample holder and piston, calcia stabilized zirconia spacers are placed on either side of the sample. At the time of

these studies, the spacers were produced in-house by cutting down parts of broken zirconia trays, which resulted in irregularities in the spacers' shape. Figure A.2 shows the length change and temperature profiles for a zero file run without spacers and one with spacers. The soak periods are marked on both zero files for reference.

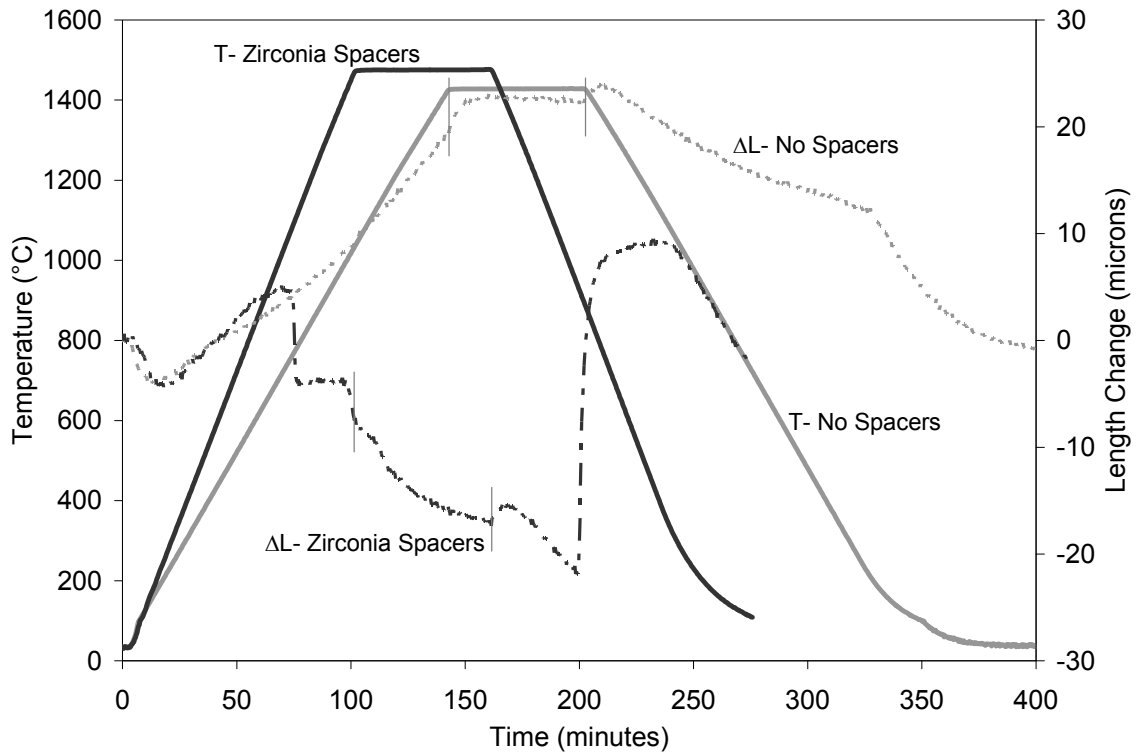


Figure A.2: Two zero files at different heating rates, one using zirconia spacers and one without. Vertical lines have been added to denote the soak period for each run.

In the zero file run with spacers, there are two sections of rapid length change, the first just after 70 minutes and the second after 200 minutes. These events are caused by the phase transition from monoclinic crystal structure to tetragonal during heating and back upon cooling. In undoped zirconia, this transition occurs at 1140 °C and causes a volume increase of about 6%, and the rapid shrinkage that takes place during the

transition back to the monoclinic structure during cooling causes significant cracking. Refractory zirconia, such as the spacers, is doped to prevent damage, though the phase transition still occurs. Both zero files also show a permanent deflection during the run, however this should not be an issue as long as the deflection is consistent across experiments.

Figure A.3 shows data from three zero files that were performed in rapid succession without opening the furnace chamber. Zero files 1 and 2 had a heating rate of 14 °C per minute while the third had a heating rate of 21 °C per minute. In each run, initial shrinkage occurred at 1075 °C and expansion during cooling occurred at 930 °C. A different amount of permanent shrinkage was observed during the high temperature portion of each run. There was a very large amount during the initial run and progressively reduced amounts in subsequent runs. Though when compared to earlier trials, which randomly show between 2 and 27 microns of permanent shrinkage, there is no consistent trend. The large amounts of shrinkage observed in the first run could be caused by the spacers moving against each other because the faces of the spacers are not parallel. This has since been remedied by purchasing commercially machined spacers. Current zero files continue to show permanent shrinkage occurring, though it is now a consistent amount. Two possible reasons for the remaining permanent shrinkage are: the spacers could be undergoing further sintering or it could be due to readjustment of microstructure related to the crystal phase change and the pressure applied by the piston. Either phenomenon could also be a contributing factor to the degradation of the spacers over time.

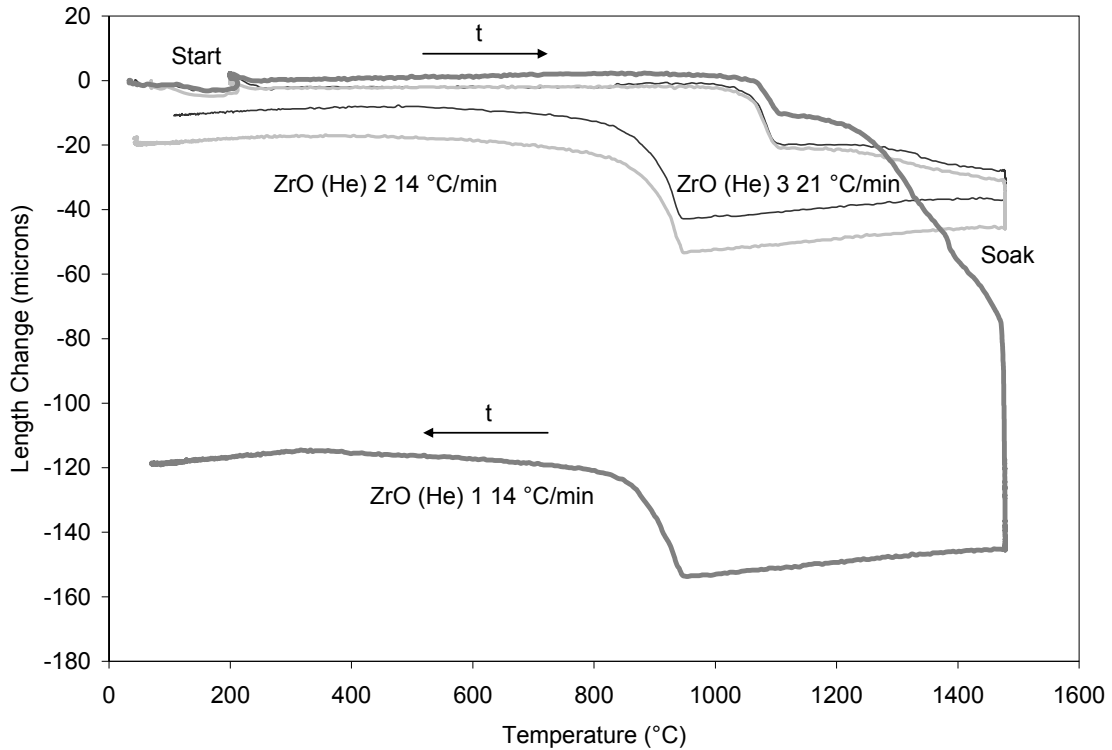


Figure A.3: Three zero files run in rapid succession, each having a low temperature soak at 200 °C and a high temperature soak at 1500 °C, in helium atmosphere on November 20th 2007 with calcia stabilized zirconia spacers.

To manually apply the zero file to experimental data, a 6th order polynomial fit of the length change as a function of temperature was generated for the zero file ZrO(Ar2). Due to the complexity of the zero file, it first needed to be broken into 6 sections and a separate approximation was generated for each section. The original zero file, the polynomial fits and the sections the file was broken into are shown in Figure A.4. For section D, the constant temperature soak, a temperature based polynomial fit could not be calculated, so observed shrinkage was assumed to be linear. The previously mentioned

changes in crystal structure of the spacers occur in section B during heating and in the beginning of section F during cooling.

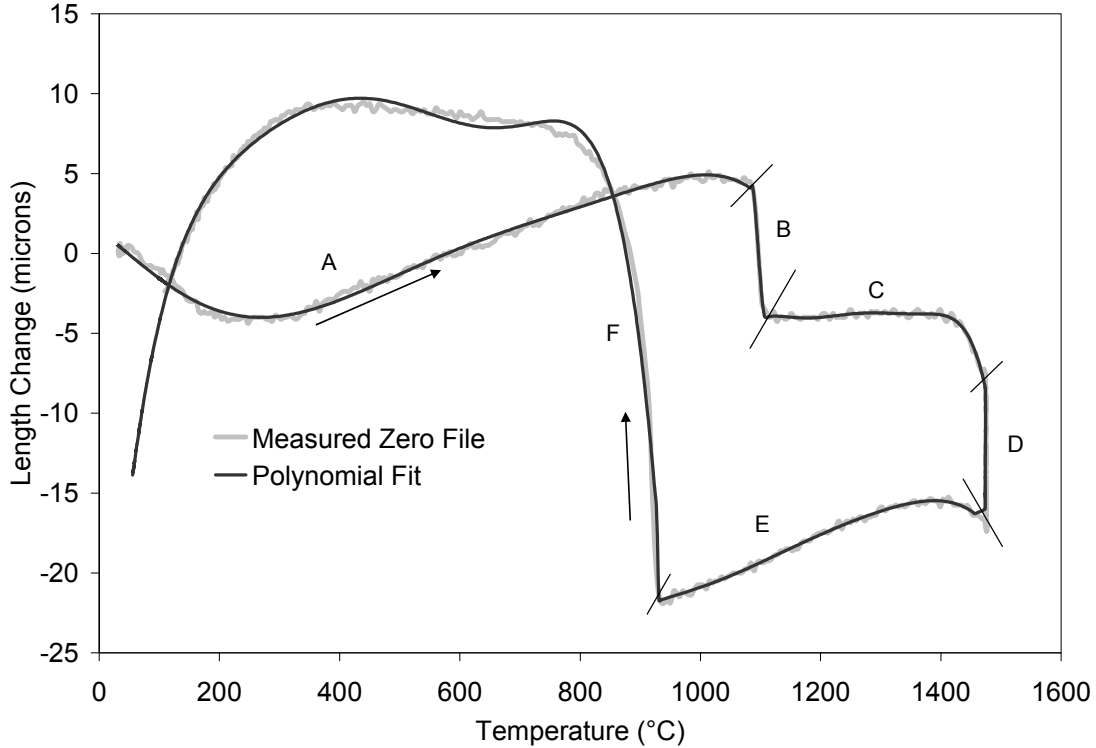


Figure A.4: Shrinkage experienced by zero file ZrO(Ar2), which had a heating rate of 15 °C per minute, along with a 6th order polynomial fit for each lettered section.

The zero file and piston corrections carried out by the dilatometer software can be manually reproduced with the following equation:

$$L = L_0 + \left(\Delta L_{Sample} - \Delta L_{Zero} + \frac{(L_0)L(T)_{Piston}}{10} \right) 1000 \quad (\text{A.1})$$

where L is the corrected length of the sample in mm; L_0 is the original sample length in mm; ΔL_{Sample} is the length change from the experiment in microns; ΔL_{Zero} is the length change in the zero file and $L(T)_{Piston}$ is the value of the piston correction for a given

temperature. Because the values in the piston correction file are in % and the sample length is in mm, a unit correction factor of 10 yields a result in microns. Figure A.5 shows the temperature profile, raw data, and manually corrected data from experiment SrTiO12a, run on March 3rd 2007, with a heating rate of 12 °C per minute. This will be used as a reference for properly corrected data for the evaluation of the software techniques. An interesting detail between the comparison of the raw data to the corrected data, is that the raw data shows nearly no signs of thermal expansion before or after sintering.

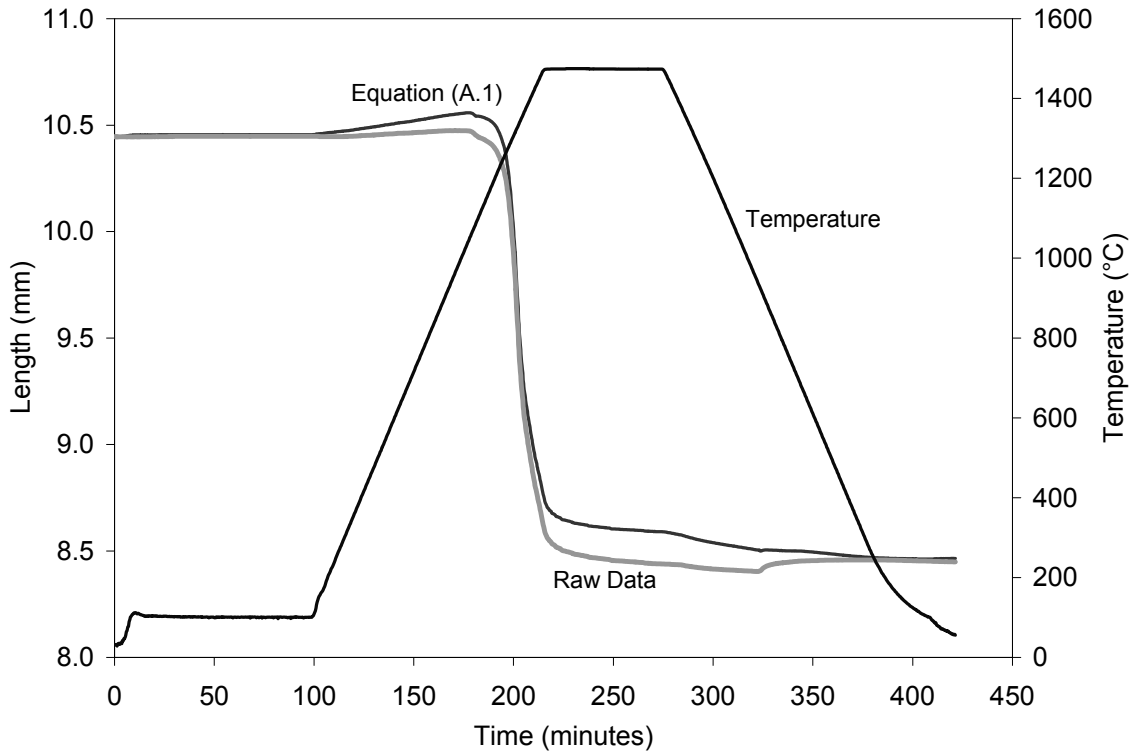
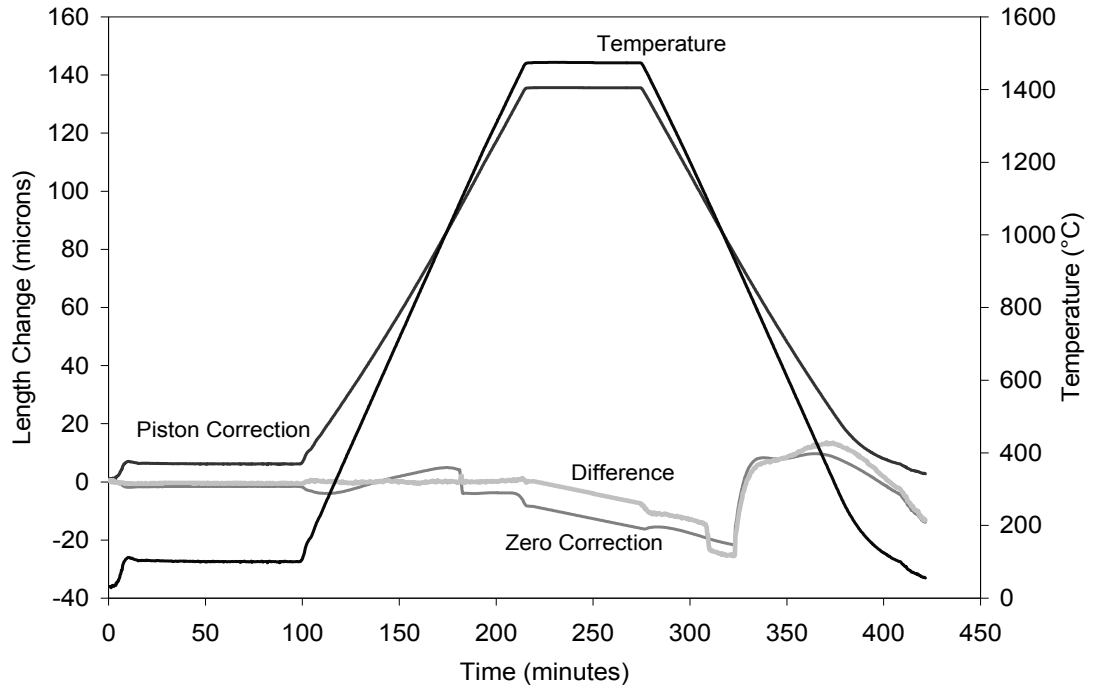


Figure A.5: Temperature profile, raw data and manual data correction with Equation (A.1) for strontium titanate run SrTiO12a.

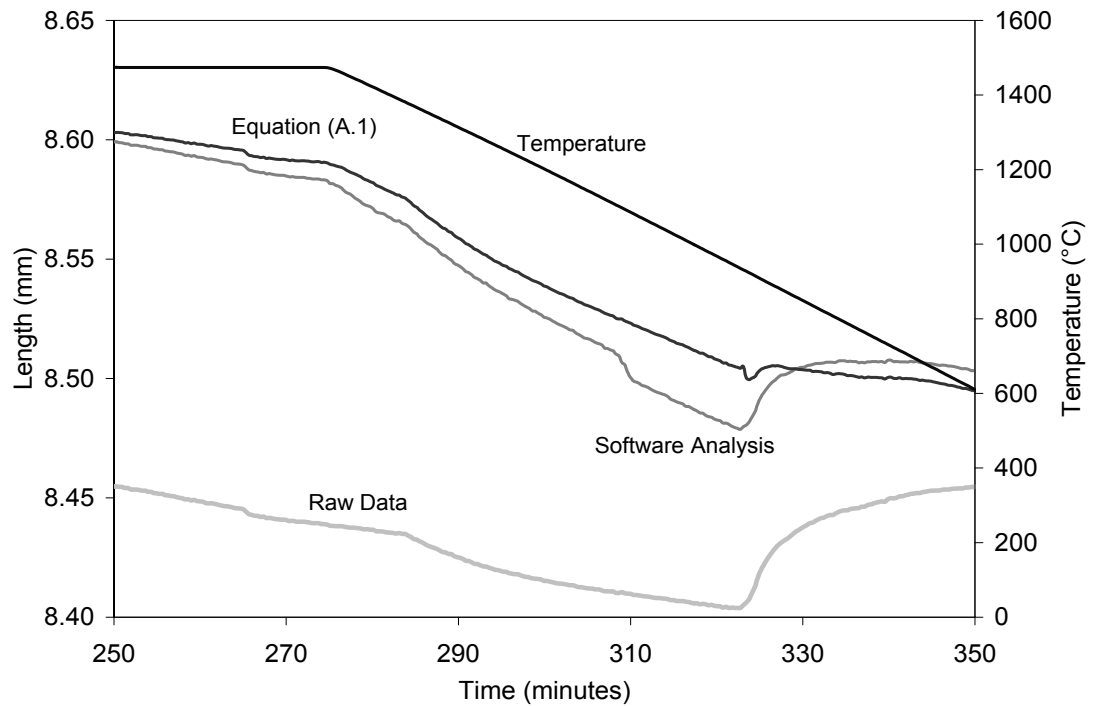
A.3 Computer Analysis

Linseis recommends that the zero file be performed directly before each experiment to minimize the effects of uncontrolled ambient conditions on CTE measurements. However, the length change of sintering is many orders of magnitude larger than what would be seen in a CTE study, so a single zero file can be used for multiple experiments. A zero file can be applied to data based on either temperature or time. Because the changes that occur in the furnace are most closely related to temperature, time dependant analysis requires heating profiles to match precisely. This process is complicated by the low temperature inaccuracy of Type B thermocouples, which could result in non-uniform heating rates at the beginning of experiments. Because temperature based analysis is not influenced by timing, there are no limitations on the heating rate of the zero file.

Figure A.6 shows a comparison between temperature based analysis performed by the software and the results from Equation (A.1). Figure A.6 (a) shows the experimental temperature profile, the polynomial fit of the zero file, the piston correction and the absolute difference between temperature based analysis and Equation (A.1). Ideally, the results from the computer analysis should be identical to the results from the application of Equation (A.1), meaning the difference function would remain zero during the entire cycle. However this only occurs for approximately the first 220 minutes; past that point, differences emerge. To explore why these differences occur, Figure A.6 (b) shows the results from Equation (A.1), temperature based analysis and the raw data over the time interval of 250 to 350 minutes.



(a)



(b)

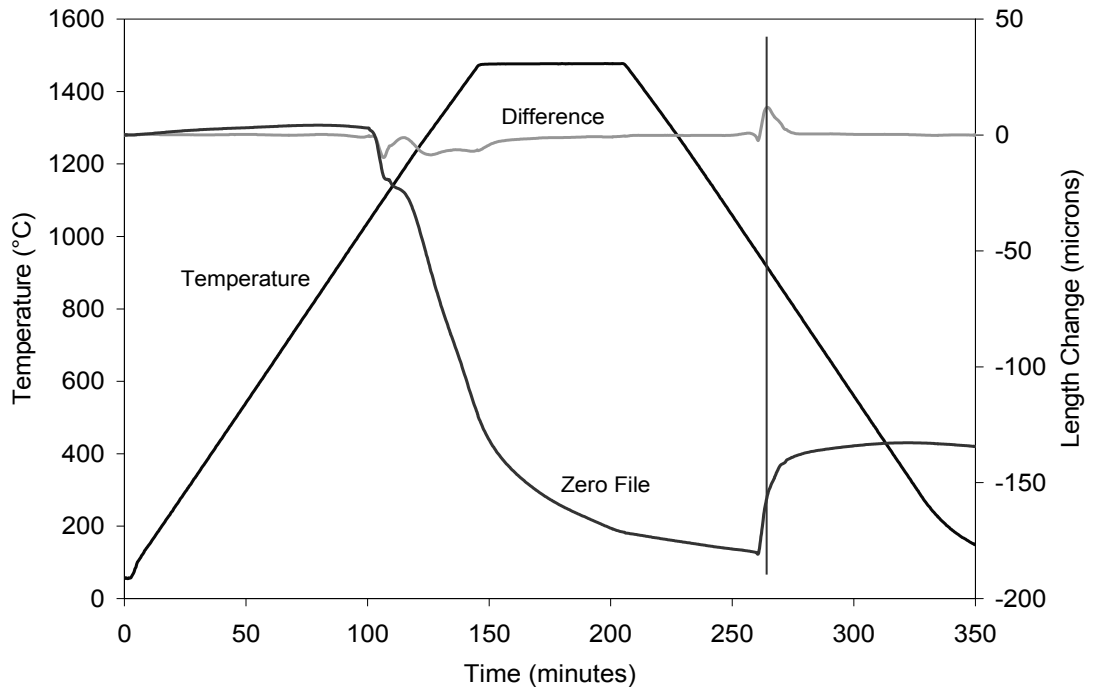
Figure A.6: (a) Experimental temperature profile, Zero file, Piston Correction and the difference between temperature based analysis and manual analysis with Equation (A.1).

(b) Raw Data, Manual Analysis and temperature based analysis over the time interval when disagreements arise.

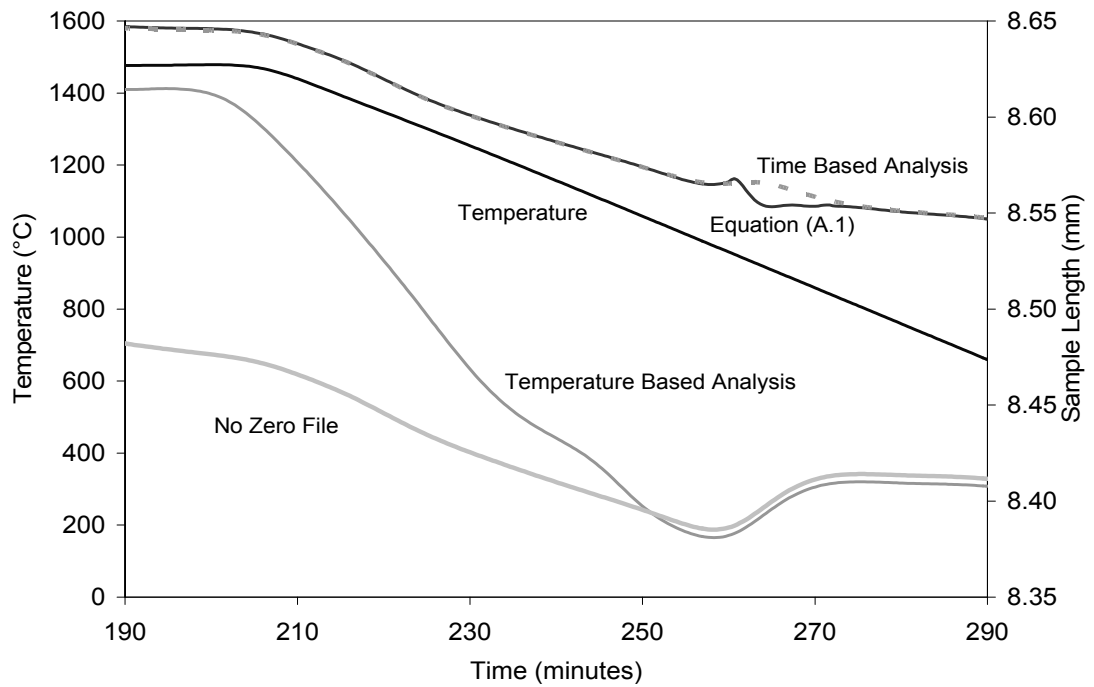
At approximately 325 minutes, there is a sharp increase in length in the raw data, matching the change in crystal structure of the spacers from the zero file shown in Figure A.6 (a). This is slightly reduced in the software analysis and is only small disturbance in the data calculated with Equation (A.1). In fact, nearly all the differences between software analysis and Equation (A.1) after the start of the soak follow the behavior of the zero file. Based on this, it appears that the software searches the zero file for the first occurrence of a given temperature and uses this value, which means that only data collected during heating is referenced. This would not be a problem with symmetric zero files, but results in the appearance of erroneous activity which arises from the zirconia spacers, and as such should not be used with the current system.

To test time-based analysis, another strontium titanate run was performed with a zero file run directly before the experiment. Both had a heating rate of 10 °C/minute up to 1500 °C and 1 hour soak. The furnace was allowed to cool for a few hours in between runs to reduce the difference in starting temperature while hopefully maintaining the effects of uncontrolled ambient conditions. The initial temperature was at 41 °C for the zero file and 58 °C for the experimental run. This small difference in starting temperature resulted in a 2 minute translation between the two temperature profiles. The polynomial fit used to approximate the zero file for use with Equation (A.1) was generated slightly differently for this experiment; during the soak, a time based approximation was used while the equations were temperature based for the other sections.

Figure A.7 shows a comparison between Equation (A.1) and time based analysis. Figure A.7 (a) shows the temperature profile, zero file and the difference between the two techniques and Figure A.7 (b) shows the results from Equation (A.1), time based analysis, temperature based analysis and software analysis performed with no zero file, over the soak and cooling. Time based analysis agrees with Equation (A.1) over the entire experiment, except for a 12 micron difference corresponding to the change in the crystal structure of the spacers. This difference can be attributed to the 2 minute translation in the temperature profile of the zero file and the experimental run. Additionally, the software analysis has much smoother and more gradual behavior even over this time period where the temperature differences between the zero file and the experiment become apparent. This is because the software uses a form of signal averaging to smooth out the line in both the X and Y direction, and this change is not reproduced by Equation (A.1). Similar to how temperature based analysis shown in Figure A.6 (b) had behavior matching that of the raw data after the soak, temperature based analysis after the soak shown in Figure A.7 (b) very closely follows the data that was analyzed without a zero file. There is also a clear change in slope before and after the change in the spacer's microstructure for all methods of analysis. Interestingly, this change in slope is even visible in the zero file run without spacers shown in Figure A.2, and it is unclear what is the cause of this activity.



(a)



(b)

Figure A.7: (a) Temperature profile, Polynomial fit of zero file and the difference between Time Based Zero File Analysis and Equation (A.1). (b) Temperature profile, Equation (A.1), Time and Temperature based analysis as well as calculations performed with the dilatometer software not using a zero file, over the soak and cooling.

A.4 Conclusion

Throughout this study, a number of details about the methodology of the dilatometer software have become apparent. Equation (A.1) has been proven to accurately reproduce the signal corrections performed by the dilatometer software. For consistency between zero files, it is important that the faces of the spacers be parallel, as non uniform spacers can shift during the expansion and contraction of a heating cycle. Regardless, there is still a small amount of permanent shrinkage observed during every run, possibly caused by small changes in microstructure or by continued sintering activity. Because temperature based analysis only uses data collected during heating, it can cause false signals during cooling if the zero file is asymmetric. Time based analysis alleviates this issue and is the best mode of analysis. However, the temperature profiles for the zero file and experiment must match exactly, which can be achieved by starting the temperature controller early, and waiting for a specific temperature to start data acquisition.